Study of Current Sharing, Magnetization, and AC Loss in REBCO Coated Conductors

Dissertation

Presented in Partial Fulfillment for the Requirements for the Degree Doctor of Philosophy

in the Graduate School of The Ohio State University

By

Shengchen Xue

Graduate Program in Materials Science and Engineering

The Ohio State University

2023

Dissertation Committee:

Prof. Michael Sumption, Advisor

Prof. Sheikh Akbar

Prof. Jinwoo Hwang

Abstract

Rare-earth barium copper oxide (REBCO) coated conductors (CCs) are of interest for fabricating high-performance cables and magnets for high-field applications (B > 22.5 T). However, the applications of REBCO CCs are facing some critical challenges, such as quench detection and protection, high magnetization loss and magnetization creep, and flux jumping due to thermal instability.

Because it is inevitable to introduce defects in REBCO CCs during the processes of manufacturing, cabling, and winding, it is important to control the current sharing between conductor tapes to enable the self-protection mechanism to take place when a localized disturbance (hot spot) appears in the cable or magnet coil. The current sharing between conductor tapes can be modified by changing inter-tape surface contact. Our study found that inter-strand contact resistance (ICR) and inter-strand thermal resistance (ITR) are determinant factors for current sharing. We modified the inter-strand contact surface properties by applying different techniques. By applying pressure, cold pressing and hot pressing, the inter-strand electrical contact efficiency, η (η = ICR $*$ contact area) can be reduced to as low as 10 μΩ*cm^2, at which value effective current sharing between REBCO CC tapes can be achieved. However, applying compression is only feasible for tape stack structure where tapes directly lay above one another without any twist pitch. For cables, such as Roebel cable, CORC cable, and STAR cable, the compression limits are much lower than that of the tape stack. Applying pressure can easily damage the tapes in the cables, leading to reduction of I_c. Therefore, performing Ni-plating and PANI coating are more suitable options. The inter-strand electrical contact efficiency, η, achieved

by Ni-plate technique is 2.7 μΩ*cm^2. PANI-coating offers a wide range of η-values needed for different requirements of various applications.

We applied experimentally achieved inter-strand contact properties to FEM analyses by using ComsolMultiphysics and assumed liquid helium (4.2 K) cooling condition. In the most ideal case, metallic inter-strand contact, a three-layer tape stack with a defective central tape could carry 3.05 critical current density (J_c) by sharing more than 0.4 J_c from the central defective tape to the two adjacent tapes, and the central defective tape showed a peak temperature of 4.37 K. In the real case scenario, if we set the inter-strand electrical contact efficiency, η, and the inter-strand thermal insulance, ω (ω = ITR*contact area), to be 5400 μΩ*cm^2 and 5.54 K*m^2/W to mimic the case of a bad inter-strand contact, the maximum current ampacity of the central defective tape reduced to 0.7 J_c with a peak temperature of 5.17 K. In the case of good inter-strand contact, given η and ω as 10 μΩ*cm^2 and 0.01 K*m^2/W, the peak temperature at the defect decreased to 5 K at 0.7 J_c applied current, and current sharing to the adjacent tapes showed significant increment. However, if the inter-strand contact was thermally insulating, thermal runaway occurred regardless of ICR, and the self-protecting mechanism through current sharing could not take place. In addition, we considered current sharing in two different states, equilibrium state and transient state. In the case of equilibrium state, the defect is pre-existing, and the current sharing takes place along the entire length of the muti-strand conductors or coils. In the case of transit state, the defect is just-created, so current sharing mostly takes near the defect. Simulation results of these two states shows that given specific inter-strand contact properties, the transient state has a lower current sharing limit. We believe that this lower limit should be carefully considered during cable and magnet designs.

Studies of magnetization and flux creep were conducted on a segment of STAR cable that is a compact design of symmetric tape round REBCO cable and promising candidate for magnet fabrication. Measurement results show the maximum magnetization normalized based on cable volume and tape volume are 1140 kA/m and 2233 kA/m. Flux creep behavior of this cable was measured by holding the cable at 1 T for 30 min and monitoring the change in magnetization over time. When the cable is fully flux penetrated, flux creep was 66 kA/m over 30 min. By applying field cycle of 0→4 T→0.8 T→1 T, flux creep reduced to 5.8 kA/m.

The AC loses of a single Ni-replacement REBCO CC tape and a loosely packed Ni-plated Roebel cables were measured. Results showed that the AC losses in the two samples consisted of mainly hysteretic loss and eddy current losses. At low field frequency (50 Hz to 150 Hz), AC loss was dominated by hysteretic loss. However, as the AC field frequency increased, eddy current loss became increasingly significant. In addition, 2-D simulation of Roebel cable was created and the simulation result was within 20% of error to the direct measurement, which is in an acceptable range.

Dedicated to my family and friends,

for their love, unwavering support

and encouragement

Acknowledgments

I would like to give my sincere and foremost gratitude to my adviser Prof. Michael D. Sumption for the continuous support and guidance he has given me through the completion of my Ph.D. study. I would like to thank the members of my dissertation committee, Prof. Sheikh Akbar and Prof. Jinwoo Hwang for their valuable advice and constructive criticism for my research and thesis.

In addition, many thanks to Prof. Edward Collings and Dr. Milan Majoros for their mentoring and enlightenment to my work. I would like to show my gratitude to my lab mates and colleagues who are Dr. Chris Kovacs, Dr. Xiaolei Guo, Dr. Fang Wan, Dr. Xiong Li, Dr. Kun Dong, Dr. Danlu Zhang, Dr. Jacob Rochester, Dr. Cory Myers, Yang Guo, Tushar Garg, Jin Kwon, Xianhao Zhang, and Minzheng Jiang. I also want to thank my collaborators at Hyper-Tech Research, Inc., including Dr. Xuan Peng, Dr. CJ Thong, Matt Rindfleisch, Dean Panik, and Michael Tomsic.

Last, but not the least, I would like to thank my beloved family for their endless and unconditional support. None of my work can be accomplished without their support.

Vita

1993……..Born in Shentou, Shanxi, China

2016……..B.S. Materials Science and Engineering,
The Ohio State University

2016 – Aug., 2023……..Graduate Research Associate,
Materials Science and Engineering,
The Ohio State University

Oct., 2023 – Present……Materials Scientist
AMPeers LLC

Publications

- **S. Xue**, M. Majoros, M. D. Sumption, T. Gard, and E. W. Collings, "FEM analysis of current sharing in REBCO coated conductor cables for particle accelerator applications," *IEEE Trans. Appl. Spercond.*, vol.33, no. 5, 2023.
- **S. Xue**, J. Kwon, Y. Guo, T. Garg, M. D. Sumption, and E. W. Collings, "Compressive Stress-Strain behavior of REBCO coated conductors and cables," *IEEE Trans. Appl. Spercond.*, vol. 33, no. 5, 2023.
- **S. Xue**, M. D. Sumption, D. Panik, C. J. Thong, X. Guo, M. Majoros, and E. W. Collings, "Electrical Contact Resistance in REBCO Stacks and Cables with Modified Surfaces," *IEEE Trans. Appl. Spercond.*, vol. 32, no. 6, 2022.
- **S. Xue**, M. D. Sumption, E. W. Collings, "YBCO Coated Conductor Interlayer Electrical Contact Resistance Measured from 77 K to 4 K Under Applied Pressure up to 9.4 MPa," *IEEE Trans. Appl. Spercond.*, vol. 31, no. 5, 2021.
- **S. Xue**, C. Kovacs, M. D. Sumption, E. W. Collings, C. J. Tong *et al.,* "Electrical and mechanical properties of high electrical conductive CNT/Cc-yarns with Br doping and Cu encapsulation," *Nano select,* vol. 3, no. 1, Jan. 2022.
- G. Tushar, J. Rochester, M. Milan, C. Kovacs, X. Peng, Matt, **S. Xue** *et al*., "Development and testing of a three-period, subsize 2G AIMI MgB2 planar undulator," *Supercond. Sci. Technol.*, vol.37, no. 1. 2024.
- M. Majoros, M. D. Sumption, **S. Xue**, E. W. Collings, "Stability and current Sharing in YBCO Cables-Impact of Broken Elements-FEM Modelling," *IEEE Trans. Appl. Spercond.*, vol. 32, no. 6, 2022.
- X. Li, E. W. Colling, F. Wan, M. D. Sumption, **S. Xue**, D. Zhang *et al.,* "Effect of biaxial cold pressure densification (BCPD) on $Ba_{0.6}K_{0.4}Fe_2As_2$ round wire using optimized precursor." *Ceram. Int.*, vol. 44, no. 4, 2018.

Fields of study

Major Field: Materials Science and Engineering

Table of Contents

List of Tables

List of Figures

List of Symbols

E_{par}: energy of particle

B: Magnetic field strength

R: Radius

P_{fusion}: power density of fusion reactor

T_c: Critical temperature

H_c: Thermodynamic critical field

$f_n(T)$: Gibbs free energy for the normal state

$f_S(T)$: Gibbs free energy for the superconducting state

$\psi(r)$: Effective wave function of the superconducting electrons at point r

m: Effective mass of charge carrier

e: Charge of an electron

α: Phenomenological parameter of Ginzburg-Landau

β: Phenomenological parameter of Ginzburg-Landau

A: Magnetic vector potential

J_s: Critical current density of supercurrent from Ginzburg-Landau theory

$\xi(T)$: Coherence length

$\lambda(T)$: Penetration depth

κ: Ginzburg-Landau parameter

ħ: Reduced Planck's constant

μ_0: Permeability of free space

B: Magnetic flux density

Λ: London parameter

n_s: Density of charge carrier

M: Magnetization in a superconductor

H_a: Externally applied field

Φ_0: Quantized fluxon

a_0: Distance between fluxons

F_p: Total pinning force

f_p: Pinning force of individual pinning center

V_c: Volume where collective pinning exists

t: Flux creep hopping time

t_0: Hopping attempt time

U_{eff}: Effective pinning energy

k_B: Boltzmann constant

U_0: Pinning energy without current

J: Current density in a superconductor

J_{c0}: Critical current density required to tilt the energy barrier for flux creep

P_h: Hysteresis loss

P_{coul}: Coupling current loss

P_{eddy}: Eddy current loss

B_0: Amplitude of applied AC field

f: Frequency of applied AC field

λ: Filling factor of superconductor

d_f: Diameter of superconductor filament

L_p: Twist pitch of a cable

$\rho_{m,\,eff}$: Effective resistivity of the matrix material in a multifilament superconductor cable

w: Width of a conductor

ρ_n: Resistivity of stabilizer

η: Inter-strand electrical contact efficiency

τ: Torque

c: Coefficient of friction

D: Major diameter of a bolt

F: Uniaxial force resulted from an applied torque

ω: Inter-strand thermal insulance

$P_{AC(hys+eddy)}$: AC loss of hysteresis component plus eddy current component

I_c: Critical current of a superconductor

C_{eddy}: Eddy current loss constant

$\rho_{300\ k}$: Resistivity of a material at 300 K

ρ_{77k}; Resistivity of a material at 77 K

$u_{r,with\ sc}$: Relative permeability with superconductor

$u_{r,no\ sc}$: Relative permeability without superconductor

f_1: Critical frequency for a superconductor cable to recouple

List of abbreviations and chemical formulas

REBCO: Rare-earth Barium Copper Oxide

Bi-2223/Bi-2212: Bismuth Strontium Calcium Copper Oxide

Bi: Bismuth

NI: No-Insulation

CC: Coated conductor

SST: Shanghai Superconducting Technology

NMR: Nuclear magnetic resonance spectrometry

HTS: High temperature superconductor

LTS: Low temperature superconductor

YBCO: Yttrium (one of the rare-earth elements) barium copper oxide

$BaCuO_3$: Barium copper oxide

$YCuO_3$: Yttrium copper oxide

IBAD: Ion beam assisted deposition

MgO: Magnesium oxide

$LaMnO_3$: Lanthanum manganese oxide

CORC: Conductor on round core

STAR: Symmetric tape round REBCO cable

TSTC: Twisted stacked tape cable

Nb_3Sn: Niobium tin

CSM: Current sharing metric

ICR: Inter-strand electrical contact resistance

ITR: Inter-strand thermal resistance

Ni: Nickel

Ag: Silver

SCE: Saturated calomel electrode

PANI: Polyaniline

H_2SO_4: Sulfuric acid

$CuSO_4 \cdot 5H_2O$: Copper sulfate pentahydrate

CNT: Carbon nanotube

FEM: Finite element method

MOCVD: Metal organic chemical vapor deposition

He: Helium

SMC: Spinning magnet calorimeter

AFRL: Air force research laboratory

LBNL: Lawrence Berkeley National Laboratory

List of equations

Chapter 1- Introduction

1.1 Motivation and Background

High-field magnets are of interest for applications in particle accelerators and fusion devices. For a particle accelerator, the maximum energy the particle can achieve in an orbit is determined by two basic parameters, the radius of the orbit and the magnetic field strength of the controlling magnets ($E_{par} \propto B \times R$). Therefore, to update the current existing particle accelerator for higher energy research without changing the infrastructure, increasing the magnetic field that controls the particles becomes the only option. In fusion technology, the power density of a fusion reactor, the volumetric fusion rate, is also determined by the strength of the magnetic field, $P_{fusion} \propto B^4$.

Superconducting materials are preferred for the winding of high field magnets. NbTi, a low-temperature superconducting alloy, has been widely used to wind magnets up to 10 T for magnetic resonance imaging and high energy physics applications. Nb_3Sn, a low temperature superconducting intermetallic compound, can be used to wind magnets up to 20 T. However, to wind magnets that can generate fields higher than 22.5 T, only the high temperature superconductors, Rare-earth Barium Copper Oxide (REBCO) and Bismuth Strontium Calcium Copper Oxide (Bi-2223 and Bi-2212), are available (Fig. 1) [1, 2, 3, 4, 5, 6].

The design of a high field magnet needs to take the mechanical properties of the materials into consideration. For a 32 T No-Insulation (NI) REBCO insert magnet, the hoop stress limits of the design are 400 MPa for the inner coil and 440 MPa for the outer coil [7]. Simulation results of the same coil show that the maximum local hoop stress within the coil can even reach 766 MPa [8]. Therefore, Bi-2212 which has a low hoop stress limit around 250 MPa is less favorable for

high field magnet construction [1] [9]. Bi-2223, in comparison with REBCO coated conductor (CC) tapes, has a lower engineering critical current density under the same background magnetic field. In addition, as a result of the development in the manufacturing technology, the price of the REBCO CCs is becoming reduced. Data provided by Shanghai Superconducting Technology (SST), the dashed line presented in Fig. 2, shows that it is possible to produce REBCO CCs for magnetic fields of from 10 T to 23 T at a cost lower than those of Bi-2212 and Bi-2223 [10]. Therefore, REBCO CCs have been proposed for many high field applications, such as nuclear magnetic resonance spectrometry (NMR) [11, 12, 13, 14, 15], particle acceleration [16, 17, 18, 19, 20], and fusion energy [21, 22, 23].

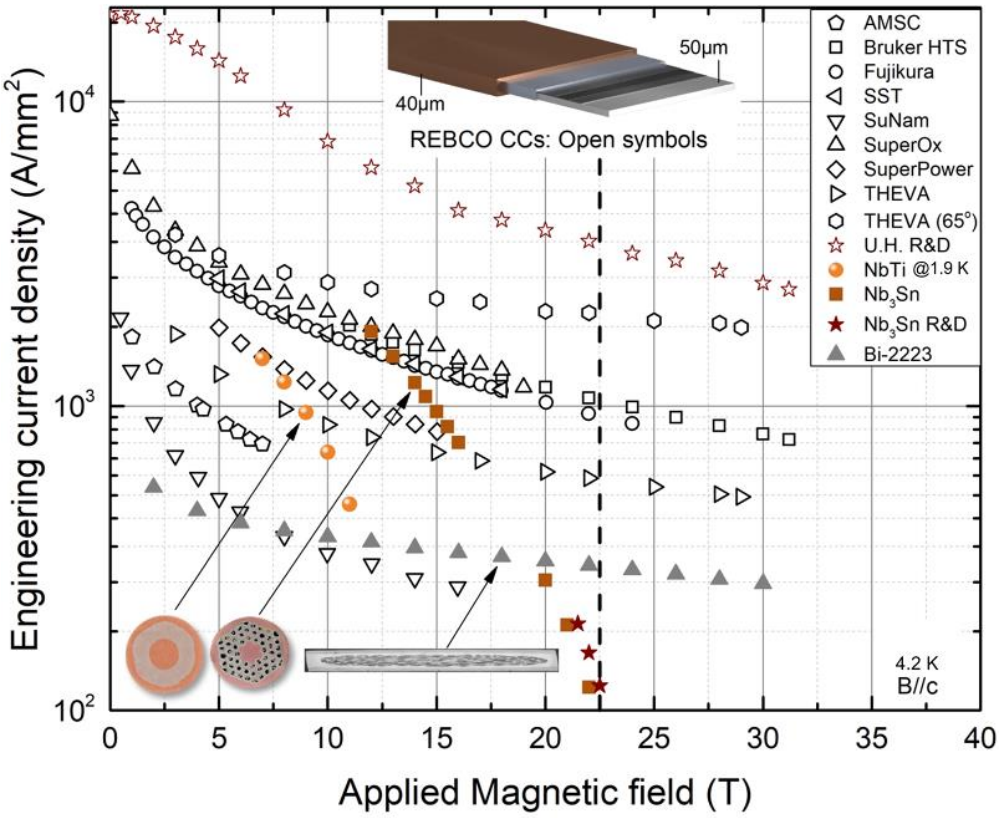

Figure 1: Engineering critical current density versus applied magnetic field at 4.2 K [1, 2, 3, 4, 5, 6].

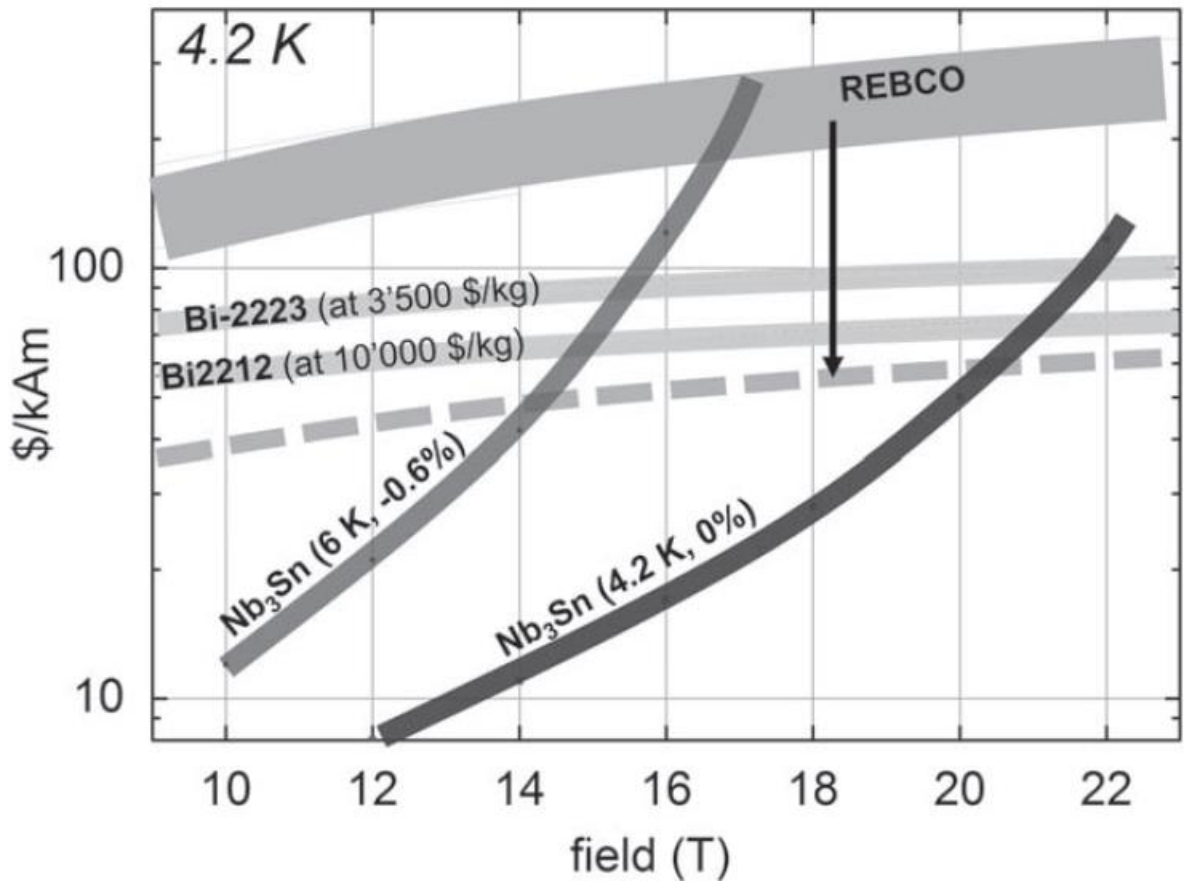

Figure 2: Price versus magnetic field at 4.2 K (dashed line indicates REBCO CCs from SST, and mechanical stress limits are not considered in this figure) [10].

1.2 Superconductivity

Superconductivity was discovered in 1911 by Heike Kamerlingh Onnes when he was performing resistivity measurements of pure metals at cryogenic temperatures. He discovered zero resistance to current flow below a critical temperature, T_c. Subsequently, Meissner showed that a superconductor could expel magnetic flux until an increasing magnetic field reached the material's thermodynamic critical field, H_c.

The superconducting state of a material is a distinct phase from its normal state at cryogenic temperature. The reduction of Gibbs free energy for the phase transitioning from normal state to superconducting state is given by Equation 1, where $f_n(T)$ and $f_S(T)$ denote the Gibbs free energy for the normal state and the superconducting state respectively, H_c is the temperature dependent thermodynamic critical field and $H_c = 0$ when the temperature reaches T_c, and μ_0 is the permeability of free space.

$$f_n(T) - f_S(T) = \frac{1}{2}\mu_0 H_c^2(T) \qquad Eq.1$$

Ginzburg-Landau theory expresses the free energy of the superconducting state as a wave function of the superconducting electrons, as shown in Equation 2 where f_n and f_S denote the free energies for the normal state and the superconducting state respectively, $\psi(r)$ is the effective wave function of the superconducting electrons at point r, $m^*$is the effective mass, e is the charge of an electron, α and β are coefficients, A is the magnetic vector potential [24]. By minimizing the free energy with respect to $\psi(r)$ and A, the two Ginzburg-Landau equations, Equation 3 and 4, are obtained [24].

$$f_S = f_n + \alpha(T)|\psi(r)|^2 + \frac{\beta(T)}{2}|\psi(r)|^4 + \frac{1}{2m}\left|(-i\hbar\nabla - \frac{2eA}{c})\psi(r)\right|^2 + \frac{1}{8\pi}|H(r) - H_a|^2 \qquad Eq.2$$

$$\alpha(T)\psi(r) + \beta(T)|\psi(r)|^2 + \frac{1}{2m}\left|\left(-i\hbar\nabla - \frac{2eA}{c}\right)\right|^2 \psi(r) = 0 \qquad Eq.3$$

$$J_s = \frac{2e}{m}\left[\psi(r)^*\psi(r)\left(-i\hbar\nabla - \frac{2eA}{c}\right) + cc\right] \qquad Eq.4$$

1.3 Coherence length and penetration depth

Based on the two Ginzburg-Landau equations, Equations 3 and 4, two fundamental length parameters are defined. (1) The coherence length, $\xi(T)$, which is distance between the two cooper pair electrons and the distance over which the superconducting parameter, $\psi(r)$, varies; (2) The penetration depth, $\lambda(T)$, over which the externally applied field penetrates the material. The Ginzburg-Landau parameter, κ, is defined as Equation 7.

$$\xi(T) = \sqrt{\frac{\hbar^2}{2m|\alpha|}} \qquad Eq.5$$

$$\lambda(T) = \sqrt{\frac{m}{4\mu_0 e^2|\alpha|}} \qquad Eq.6$$

$$\kappa = \lambda/\xi \qquad Eq.7$$

London theory also defines a penetration depth. The magnetic flux density, B, in the London theory is expressed in terms of the London parameter, Λ, as shown in Equation 8.

$$B = \Lambda \nabla^2 B \qquad Eq.8$$

Based on Maxwell's equation, the London parameter, Λ, can be expressed by Equation 9, where m is the mass of charge carrier, e is the charge of superelectrons, and n_s is the density of charge carriers.

$$\Lambda = \frac{m}{\mu_0 n_s e^2} \qquad Eq.9$$

For the simplest one-dimensional scenario, the magnetic flux density from the surface of a superconductor to a point x within the superconductor follows an exponential decay in Equation 10. Therefore, the London penetration depth, λ_L, is given by Equation 11.

$$B(x) = B_0 \exp\left(-\frac{x}{\sqrt{\Lambda}}\right) \qquad Eq.10$$

$$\lambda_L = \sqrt{\Lambda} = \sqrt{\frac{m}{\mu_0 n_s e^2}} \qquad Eq.11$$

1.4 Type-I superconductor and Type-II superconductor

The two characteristic lengths, coherence length and penetration depth, can be used to define Type-I and Type-II superconductors. Type-I superconductors, for example Nb, Pb, and Sn, exhibit perfect diamagnetism when the externally applied field is below the material's thermodynamic critical field, H_c. The expulsion of the externally applied field is due to the generation of a screening current that flows at the surface of the superconductor to a depth of λ, the penetration depth [25]. This screening current will induce a magnetization, M. Therefore, as shown in Equation 12, the magnetic field in the superconductor, B, can be calculated by adding the opposing magnetization to the externally applied field, H_a. When $T < T_c$ and $H_a < H_c$, $M = -H_a$, and hence $B = 0$.

$$B = \mu_0(M + H_a) \qquad Eq.12$$

For a type-I superconductor, the Ginzburg-Landau parameter, κ, is less than $1/\sqrt{2}$. When a current is applied through the type-I superconductor, it will experience the self-field. If the field is strong enough to penetrate the superconductor, certain parts of it will become normal.

However, as depicted in Fig. 3, the interface energy resulting from the formation of the superconducting and normal mixed state in a type-I superconductor is positive [26]. Hence, it is not possible to form such a superconducting and normal mixed state, making the Type-I superconductors not technically useful.

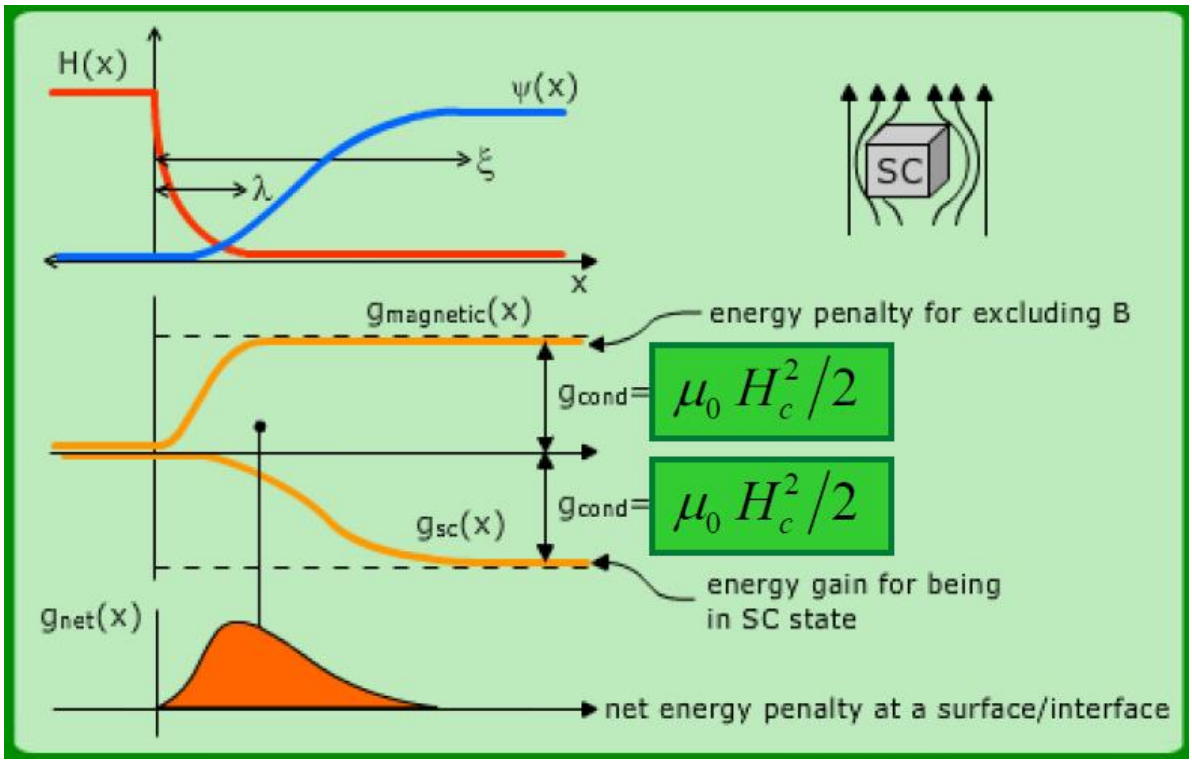

Figure 3: Gibbs free energy of the superconducting and normal interface in a Type-I superconductor [26].

On the other side, the interface energy of the superconducting and normal mixed state in a type-II superconductor is negative, Fig. 4 [26]. Therefore, when a type-II superconductor experiences an externally applied field, it will exhibit three distinct stages as the field increases. First, when the externally applied field is less than the lower critical field, H_{c1}, the type-II superconductor expels all magnetic field due to the Meissner effect. Then, when the externally applied field increases to the range greater than the lower critical field, H_{c1}, but less than the

upper critical field, H_{c2}, some field will penetrate the superconductor while the superconductor still remains superconducting, leading to the superconducting and normal mixed state. In this regime, $H_{c1} < H < H_{c2}$, the magnetic flux entering the type-II superconductor is immobilized by the flux pinning centers to be described in the next section. Finally, when the externally applied field surpasses the upper critical field, H_{c2}, the superconductivity is destroyed. Fig. 5 shows a typical superconducting domain of a technical superconductor, type-II superconductor, on the phase diagram that is defined by temperature, current density, and magnetic field [27].

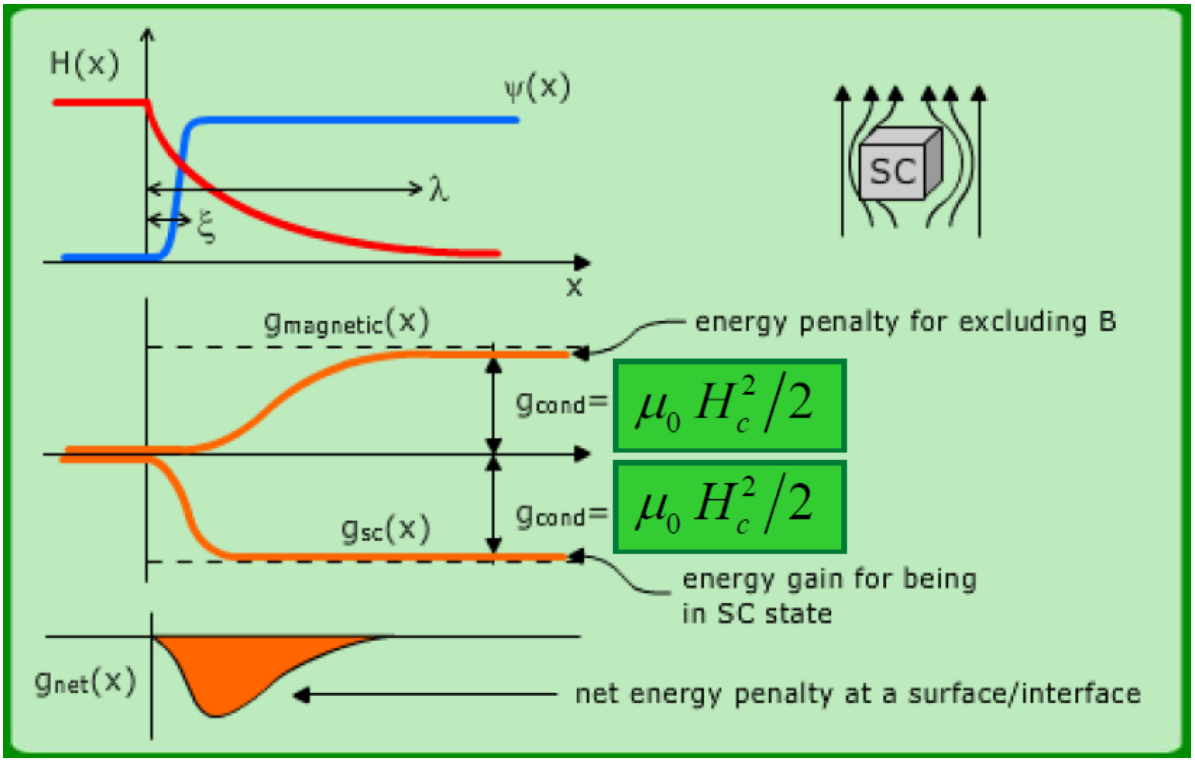

Figure 4: Gibbs free energy of the superconducting and normal interface in a Type-II superconductor [26].

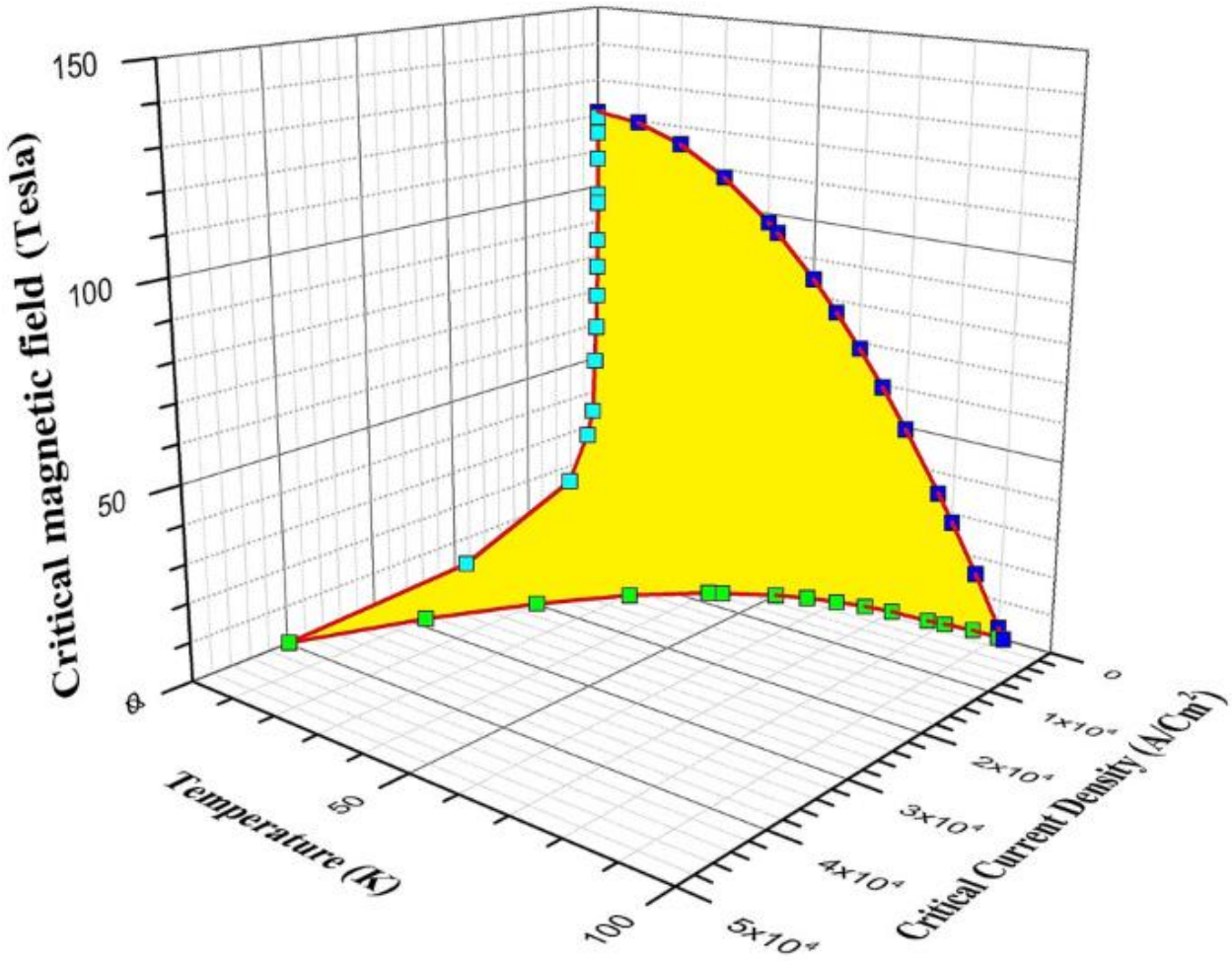

Figure 5: Phase diagram of YBCO [27].

1.5 Flux pinning

As shown in Fig. 6, a single fluxon has a core radius equal to the coherence length, ξ. At the center of the fluxon core, the supercurrent density is zero while the magnetic field is equal to the externally applied field, leading to a non-superconducting volume [28]. Supercurrent circulating around the non-superconducting core generates a magnetic field that cancels the magnetic field in normal core over the distance of the coherence length, ξ, and the magnetic flux carried by this magnetic field can be quantized as $\Phi_0 = \frac{h}{2e} = 2.0678 \times 10^{-15}\ Wb$ [29]. Hence, the magnetic

field in a type-II superconductor is the density of fluxons inside the superconductor according to Equation 13. Here n is the number of fluxons and a_0 is the distance between them.

$$B = n\Phi_0/a_0^2 \qquad Eq.13$$

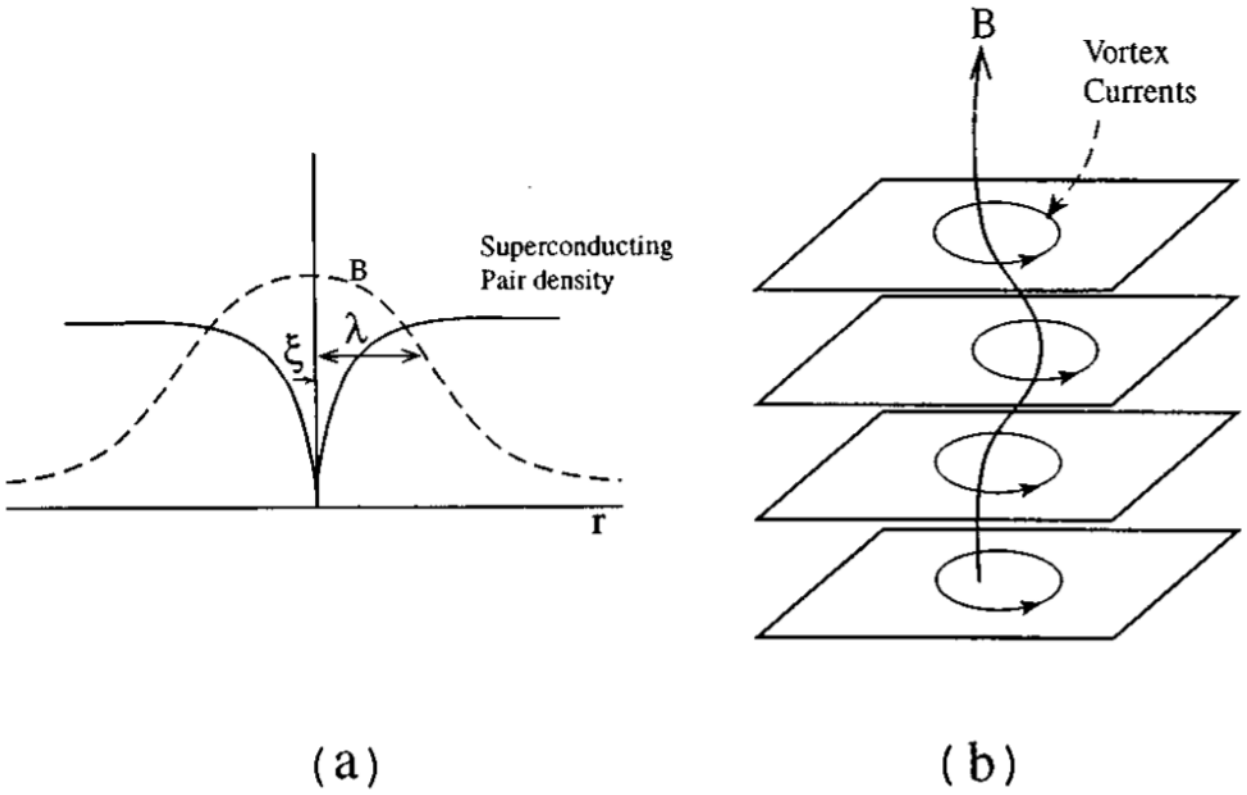

Figure 6: Cross section view of a fluxon structure [28].

The fluxons in a type-II superconductor are pinned by the pinning centers. The optimal radius of pinning centers should be comparable to the coherence length, ξ, which is affected by the temperature. Based on the size and morphology of the pinning centers, they can be categorized as zero dimensional, one dimensional, two dimensional, and three dimensional, seen in Fig. 7 [30]. Zero dimensional pinning center have size less than ξ. Typical examples of Zero dimension pinning centers are vacancies [31], cation disorder [32], and dilute doping [33]. One dimensional pinning centers include columnar defects and dislocations [34]. Two

dimensional pinning centers are usually in the form of grain boundaries [35] [36] [37] and interface between phases [38]. Three dimensional pinning centers have size comparable to or larger than ξ, which is temperature dependent according to equation 14, and exist in the form of nanoparticles or second phases [39] [40] [41] [42].

$$\xi(T) = \xi(0)\sqrt{\frac{T_c}{T_c - T}} \qquad Eq.14$$

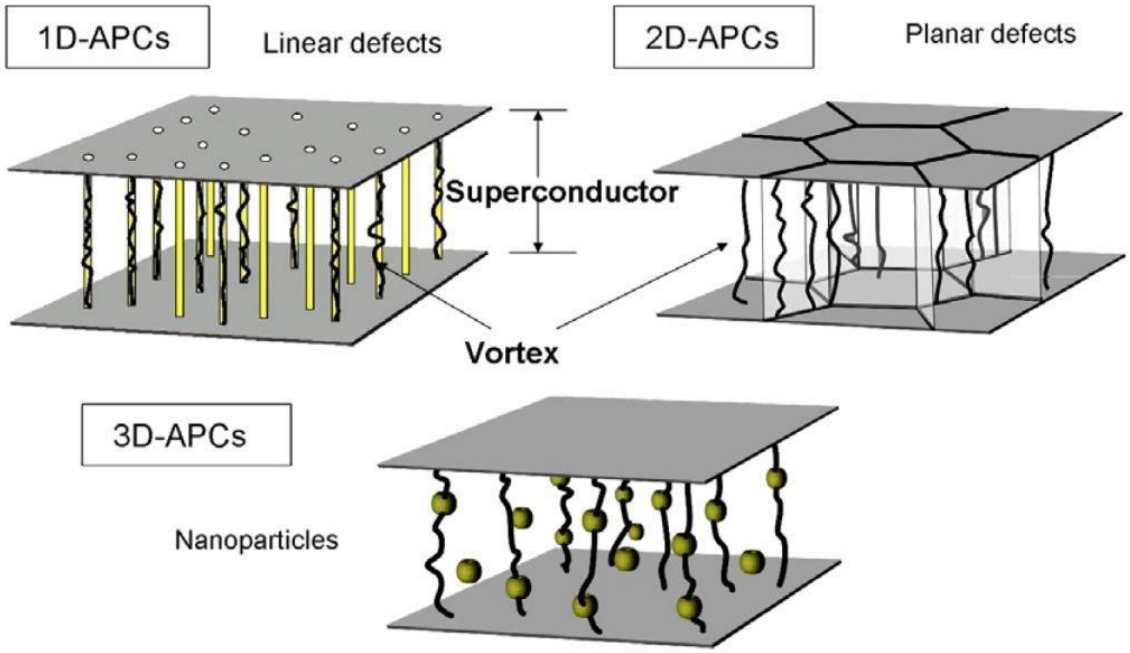

Figure 7: 1D, 2D, and 3D pinning centers [30].

Multiple pinning mechanisms can coexist in a superconductor. In the case of REBCO, weak pinning centers are oxygen vacancies. The pinning force for those weak pinning centers can be described by the collective pinning model, Equation 15, where F_p is the total pinning force, f_p is the pinning force of individual pinning center, n is the density of pinning centers, and V_c is the volume where the collective pinning forms. Strong pinning centers in REBCO are nanoparticles

and nanorods, such as $BaZrO_3$ and $BaCeO_3$, and the total pinning force, F_p, in this case can be simply calculated as the summation of the pinning force from individual pinning centers, Equation 16.

$$Weak\ pinning: F_p = \sqrt{\frac{nf_p^2}{V_c}} \qquad Eq.15$$

$$Strong\ pinning: F_p = nf_p \qquad Eq.16$$

1.6 Flux creep

Due to the magnetic flux gradient within the superconductor, magnetic flux tends to diffuse from high density region to the low density region as demonstrated in Fig. 8. This diffusional process, flux creep, is governed characterized by the Arrhenius equation, Equation 17, where t is the flux creep hopping time, t_0 is the hopping attempt time, U_{eff} is the effective pinning energy, k_B is the Boltzmann constant, and T is temperature [43].

$$t = t_0 exp\left(\frac{-U_{eff}}{k_B T}\right) \qquad Eq.17$$

The term U_{eff} in Equation 17 is affected by current. As shown in Fig. 9, the energy barrier that inhibits flux creep will be tilted by the presence of a current as described by Equation 18, where U_0 is the pinning energy without current, J is the current density in the superconductor, and J_{c0} is the critical current density required to tilt the energy barrier [43].

$$U_{eff} = U_0\left(1 - \frac{J}{J_{c0}}\right) \qquad Eq.18$$

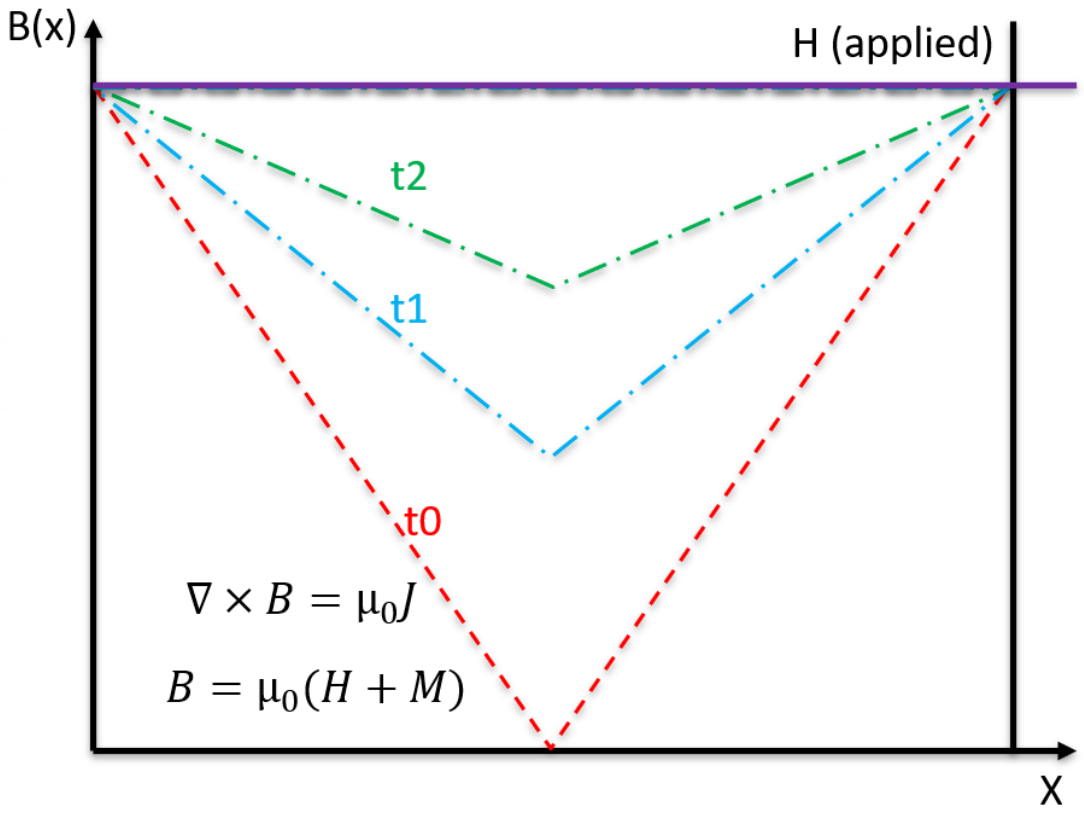

Figure 8: Flux creep within a superconductor

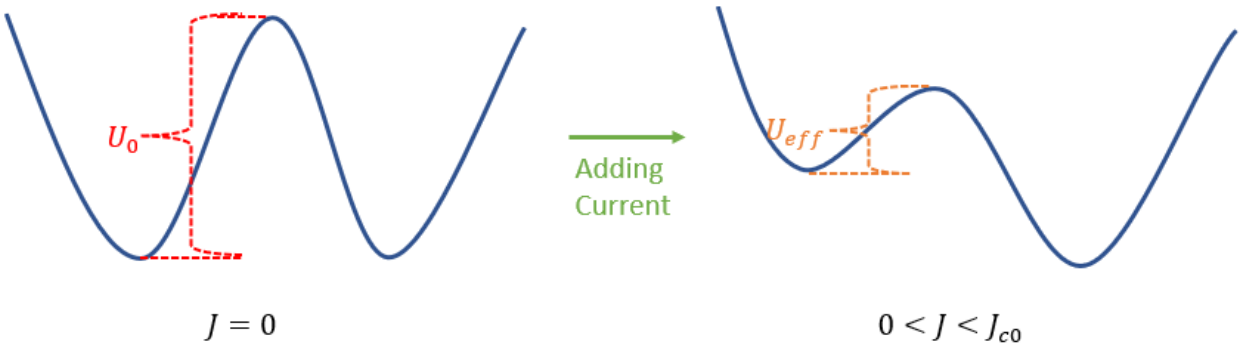

Figure 9: Energy barrier tiled at the presence of a current in the superconductor.

Since the current density in the superconductor is determined by the magnetic field gradient, a time varying magnetic field gradient will lead to a time varying current density, J, shown in

Equation 19. Because the magnetization, M, in the superconductor is proportional to J, the magnetization can be written in a time dependent form as Equation 20 [43].

$$J(t) = J_{c0}[1 - \frac{k_B T}{U_0} ln(\frac{t}{t_0})] \qquad Eq.19$$

$$M(t) = M_0[1 - \frac{k_B T}{U_0} ln(\frac{t}{t_0})] \qquad Eq.20$$

It can be concluded that flux creep is dependent on temperature, pinning strength, and current density in the superconductor. Therefore, flux creep is more prominent in high temperature superconductors (HTS) than in low temperature superconductors (LTS). HTS are able to operate at higher temperatures, which enables the flux creep to respond to the increased thermal activation energy. The critical current density is proportional to the total pinning force. As demonstrated in section 1.5, the total pining force can be increased by creating more pinning centers and introducing strong pinning centers. In the case of HTS, for example REBCO, the property of high critical current density is given by high total pinning force, which is partly ascribed to the abundance of weak pinning centers, oxygen vacancies [31]. However, from the perspective of flux creep, the combination of many weak pinning centers and high critical current density enhance the flux creep rate. Moreover, the magnetization of a superconductor is proportional to the size, diameter of round filament and width of tape, of the conductor, following the relationship $M \propto J_c d$ [44] [45]. Compared to LTS [46] [47], HTS have much bigger filament diameters [48] [49] [50], hence higher magnetizations [51] [52] [53] than LTS.

The performance of a magnet fabricated with HTS will suffer from an enhanced error field caused by the strong magnetization of the HTS. Therefore, error correction, for example using

compensation coils, needs to be included in magnet design. Flux creep will make the error field time varying. Therefore, it is important to measure the creep rates of the superconducting materials, so that a creep component can be included in the accelerator field error calculations, which are typically performed using finite-element software such as ROXIE [54] [55] and OPERA-2d [56] [57], to achieve better field quality.

1.7 AC loss

When a superconductor is exposed to an alternating field, it experiences AC loss. As shown in Fig. 10, 11, and 12 [10] [58] [59], superconductor cables consist of multiple strands or filaments such that three components may contribute to the AC loss.

Hysteretic loss originates from the magnetization of the superconductor. Derived by an alternating field, a current will be induced in the superconducting filaments to oppose the change of magnetic field. The hysteretic loss, P_h, can be described by Equation 21, where B_0 is the amplitude of the applied AC field, f is the frequency of the AC field, λ is the filling factor of the superconductor, J_c is the critical current density, and d_f is the diameter of the filament [60] [61].

$$P_h \propto B_0 f \lambda J_c d_f \qquad Eq.21$$

The coupling loss component is given by Equation 22. The coupling loss is proportional to the squares of the amplitude of the AC field, B_0^2,the frequency of the AC field, f^2, and twist pitch of the cable, L_p^2. Since the coupling current flows in between superconducting filaments, the coupling loss is inversely proportional to the effective resistivity of the matrix material, $\rho_{m,eff}$, where the superconducting filaments are imbedded [60] [61].

$$P_{coul} \propto \frac{B_0^2 f^2 L_p^2}{\rho_{m,\,eff}} \qquad Eq.22$$

Eddy current loss is generated by the current flowing near the surface of the normal materials in response to the time varying magnetic field. Therefore, this loss component, demonstrated in Equation 23, is proportional to the square of the amplitude of the sweeping field, B_0^2, the frequency of the sweeping field, f^2, and the width of the conductor, w^2, but is inversely proportional to the resistivity of the normal material, ρ_n, which serves as the stabilizer of the cable [60] [61].

$$P_{eddy} \propto \frac{B_0^2 f^2 w^2}{\rho_n} \qquad Eq.23$$

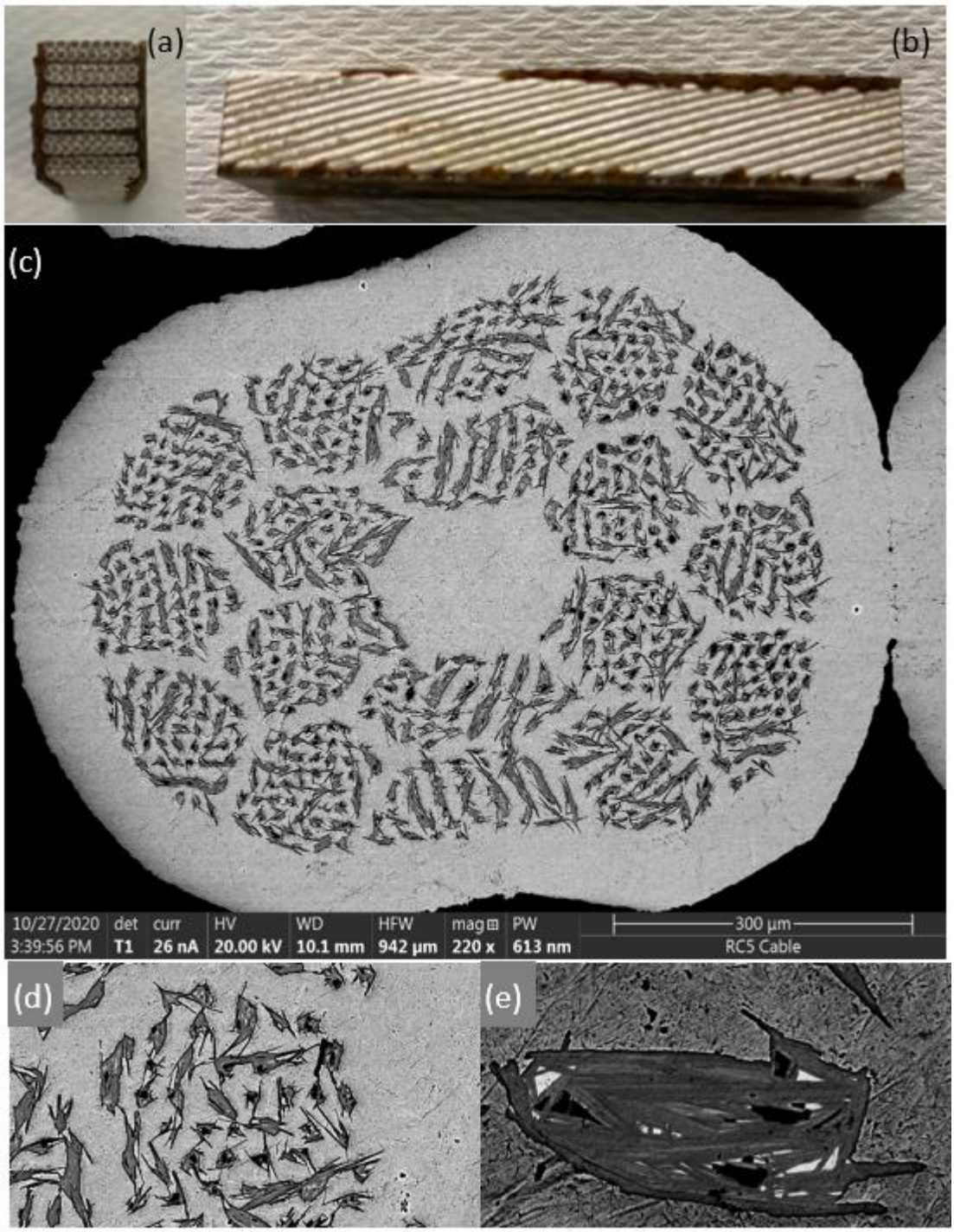

*Figure 10: Bi2212 cable (a) cable side view 17*6 strands, (b) cable top view, (c) SEM of strand, (d) SEM of filament in a strand, (e) higher magnification SEM of filament*

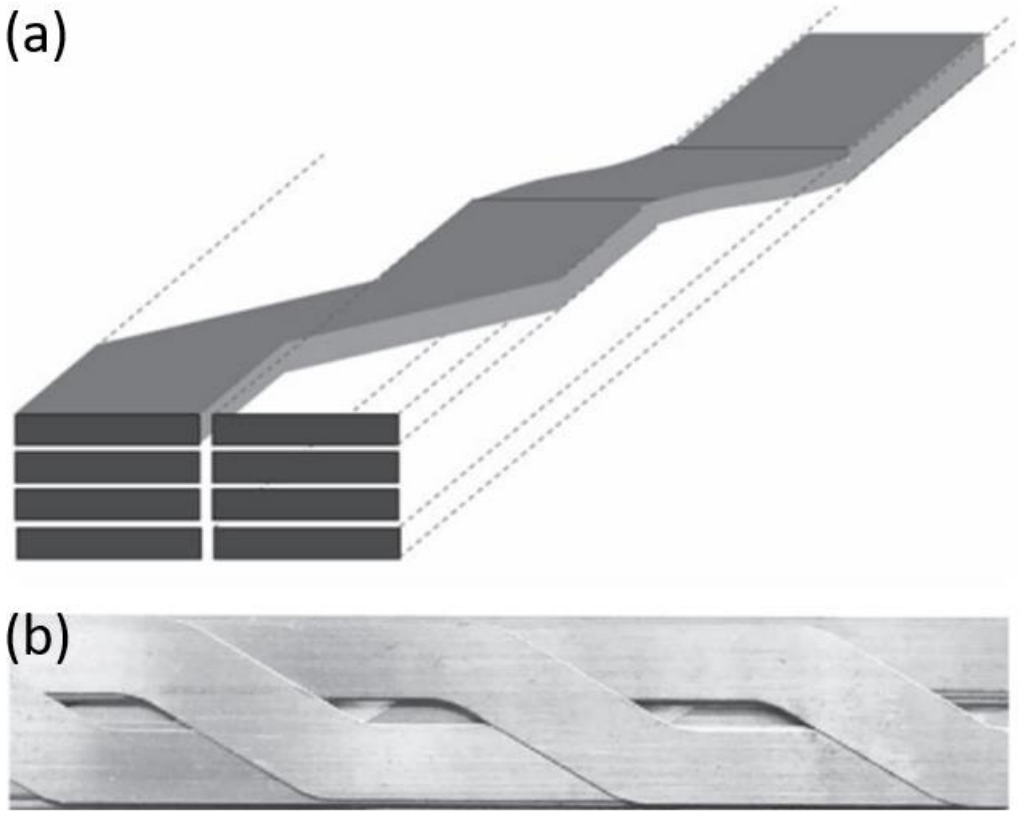

Figure 11: (a) Schematic drawing of Roebel cable, (b) Top view of Roebel cable [10]

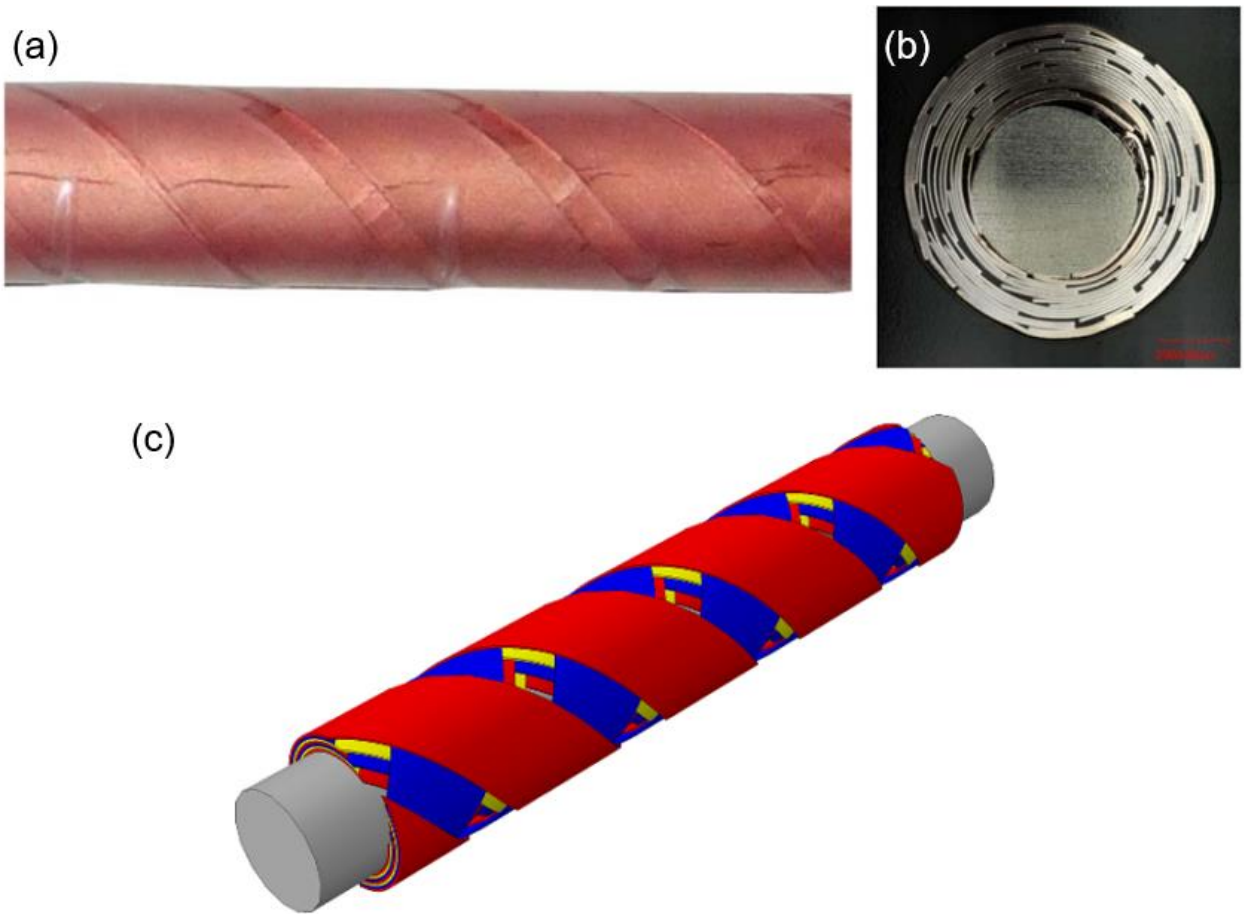

Figure 12: REBCO CORC cable (a) side view [58], (b) cross-sectional view [58], (c) oblique view [59]

1.8 Rare-earth barium copper oxide (REBCO)

The crystal structure of Yttrium (one of the rare-earth elements) barium copper oxide (YBCO) is presented in Fig. 13. It can be seen as a stack of perovskites of $BaCuO_3$, $YCuO_3$, and $BaCuO_3$ from bottom to top or a stack of alternating layers of CuO chains and CuO_2 planes [62]. With reference to the chemical formula $YBa_2Cu_3O_{6+x}$, a phase transition occurs from tetragonal to orthorhombic when x is around 0.35, and this phase transition also leads to the development of superconductivity in YBCO [63] [64]. As presented in Fig. 14, when the value of x is 0.94, the

critical temperature of YBCO, T_c, reaches the maximum of 92 K [64]. YBCO is an anisotropic material, and therefore, its superconducting properties in the a-b plane are different from those along the c-axis, as tabulated in Table 1 [65] [66] [67].

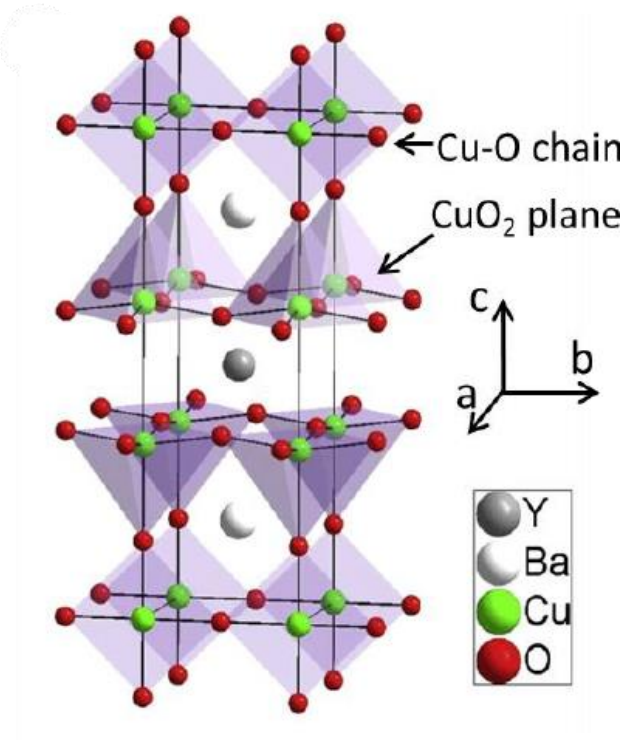

Figure 13: YBCO crystal structure [62]

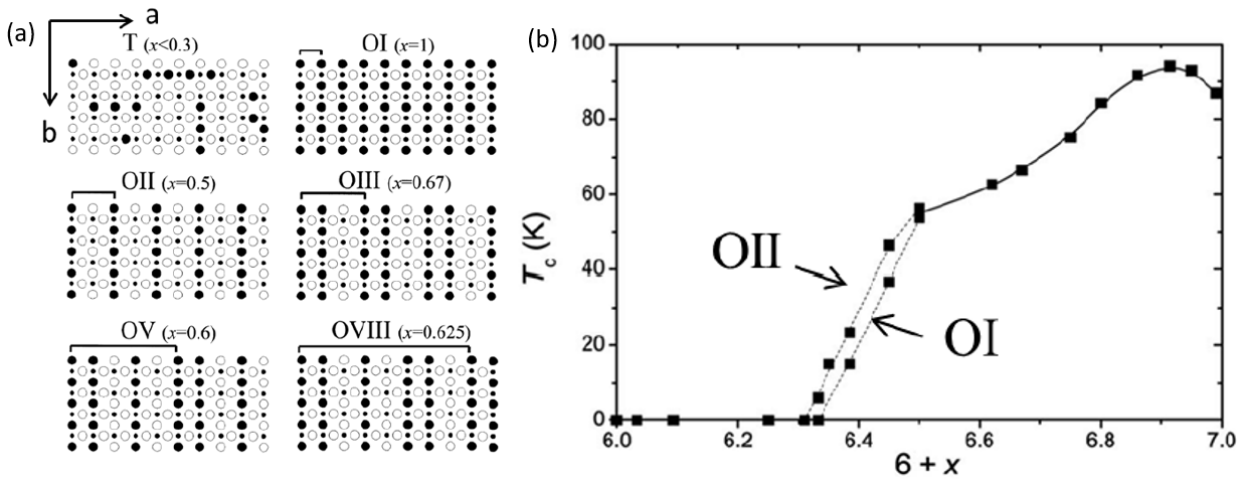

Figure 14: (a) top views of CuO chain in $YBa_2Cu_3O_{6+x}$ as the value of x varies (T denotes the tetragonal structure. OI, OII, OIII, OV, and OVIII are orthorhombic structures. Solid big circles and small circles are occupied sites of copper and oxygen, and open circles are vacancies correspondingly) [63], (b)T_c of YBCO with different values of x [64]

Table 1: Superconducting parameters of YBCO in a-b plane and along c-axis [65] [66] [67].

	a-b plane	c-axis
Coherence length, ξ (nm)	1.5-2.0	0.3-0.5
Penetration depth, λ (nm)	750	150
Upper critical field, H_{c2} (T)	>150	100-150

The processes of fabricating REBCO coated conductors (CC) are different for different manufacturers. REBCO CCs used in this study are mostly from SuperPower. The structure of the SuperPower 2G REBCO CC is presented in Fig. 15 [68]. A 50 µm Hastelloy tape is used as the substrate to provide mechanical strength of the CC. Then a buffer stack consisting from bottom

to top of alumina, Yttria, ion beam assisted deposition (IBAD) MgO, homo epitaxial MgO and $LaMnO_3$, is deposited on the Hastelloy substrate [69]. Alumina in the buffer layer serves as a diffusion barrier. Yttria is used as a seed layer for the IBAD MgO. $LaMnO_3$ plays the role of matching the lattice to REBCO. The REBCO layer is deposited on the buffer layer through a metalorganic chemical vapor deposition process (MOCVD). On top of the REBCO layer and the bottom of the Hastelloy substrate, a silver overlayer is deposited to provide good current transfer in between the REBCO layer and the copper layer stabilizer.

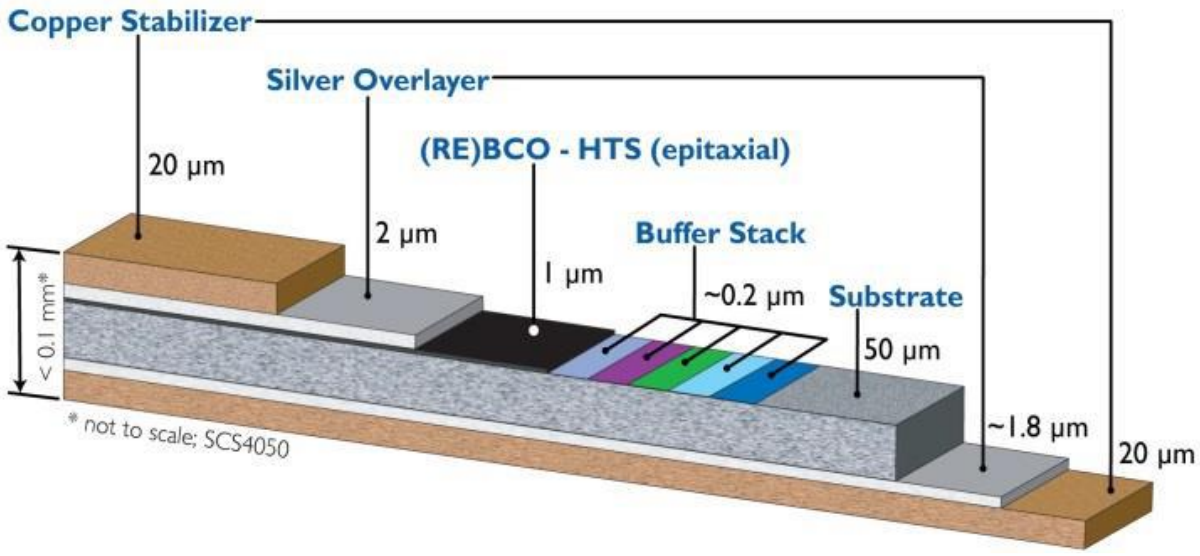

Figure 15: Structure of SuperPower REBCO 2G HTS tape [68].

1.9 Current sharing in REBCO tapes and cables

REBCO coated conductors (CCs) are promising material candidates for high field superconducting magnets. Various magnet designs with different cable/tape configurations have been proposed and constructed, such as tape-to-tape no-insulation coils [70], Roebel cables [71] [72], conductor on round core (CORC) cables [73] [74] [75], symmetric tape round REBCO (STAR) cables [76] [77], and twisted stacked tape (TSTC) cables [78].

However, unlike low temperature superconductors such as Nb_3Sn which has a normal zone propagation velocity of 1-100 m/s [79] [80], REBCO CCs have slow normal zone propagation velocities of 3-5 cm/s (driven by their higher Tc) [81] [82]. This makes the quench detection and protection major challenges for REBCO magnets development. One way to increase the stability of a REBCO coil is to introduce current sharing between the REBCO CC tapes.

REBCO CCs contains defects that can be introduced during the manufacturing process, coil winding, and operation with various sizes [83] [84] [85]. As shown in Fig. 16 [70], when current reaches the defect, a low contact resistance interface will allow the current to detour into adjacent conductor.

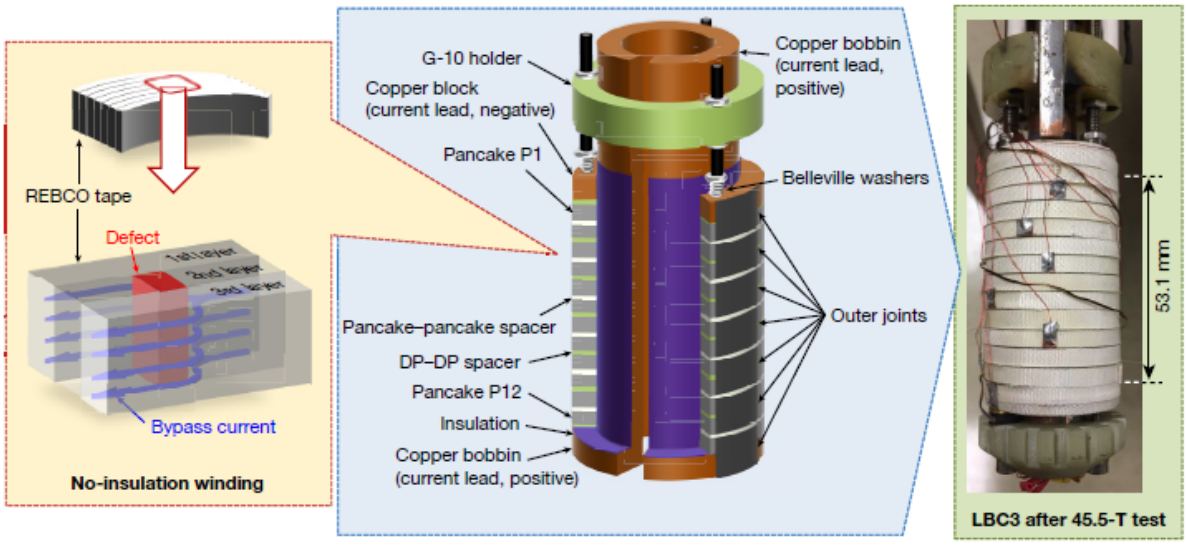

Figure 16: Current sharing REBCO tapes in a no-insulation winding; Construction design of the 45.5 T insert NI coil, actual photo of 45.5 T insert NI coil [70].

In this work we introduce the current sharing metric (CSM). In the case of LTS, current sharing refers to the inter-strand current redistribution in a multi-strand cable, so the CSM of LTS can be

defined as the ratio between maximum achievable current and the nominal current of a multi-strand cable, denoted as $CSM_{LTS} = I_{cable}/I_{c,nominal}$. The quench event in LTS is an adiabatic process which can be caused by disturbance spectrum. Hence, the limiting factor is the minimum quench energy and current sharing limit can be only controlled by the inter-strand electrical contact resistance (ICR). As presented in Fig.17, the current sharing metric of LTS, CSM_{LTS}, decreases as the ICR, and the metric is always smaller than one [86].

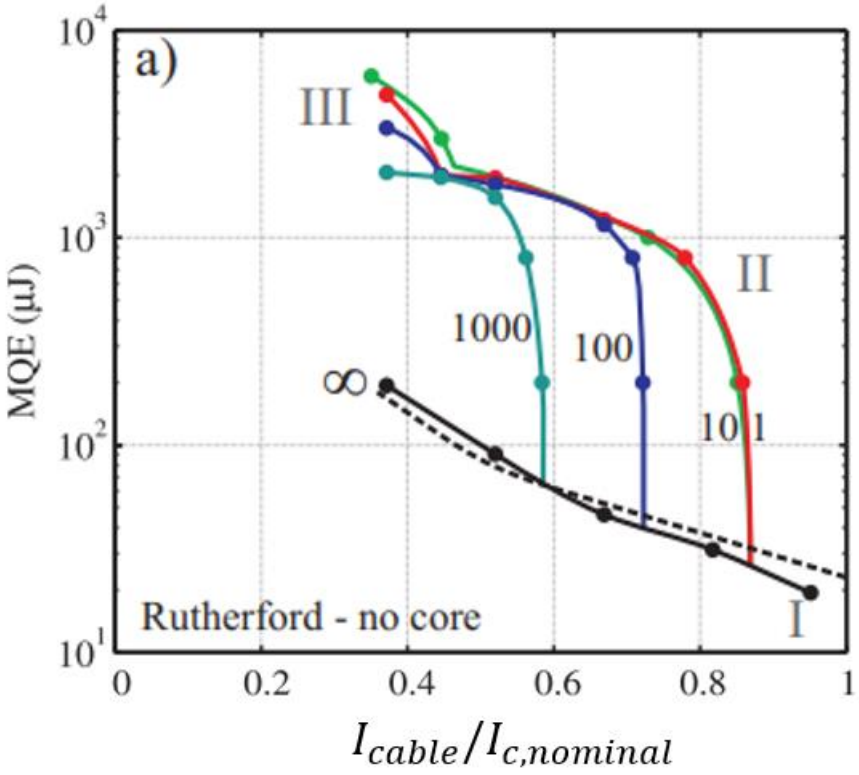

Figure 17: MQE and CSM_{LTS} as a function of inter-strand contact resistace. (A no core Rutherfold NbTi cable, inter-strand electrical contact resistance varies from 1 μΩ to 1000 μΩ) [86].

For a HTS, such as REBCO CC, because the ΔT between the operating temperature and T_c is much bigger, HTS is more tolerant to disturbance spectrum. However, the presence of defects in

the conductor tape needs to be considered. Therefore, the current sharing metric of a REBCO CC cable is determined as the ratio of the maximum achievable current in a cable with defects to the nominal critical current of a cable without any defects, denoted as $CSM_{HTS} = I_{cable\_defect}/I_{cable\_no\_defect}$. In this case, the current sharing limit is determined by inter-strand electrical contact resistance (ICR), inter-strand thermal resistance (ITR), and boundary cooling conditions.

Chapter 2- Control inter-strand contact properties through surface treatment

Numerous techniques have been applied to control the inter-strand contact resistance, including cold pressing, hot pressing, Ni plating, and conductive polymer plating. The inter-strand electrical contact efficiency, η, as defined by Equation 24 and is a dimension-independent property, for the as-received tapes is 17000 $\mu\Omega * \mathrm{cm}^2$measured at 77 K [87]. The high inter-strand electrical contact efficiency can be ascribed to the intrinsic oxide layer on the Cu surface. The following sections will introduce some of the numerous techniques that have been applied to change the inter-strand contact properties.

$$\eta = ICR * contact\ area \qquad Eq.24$$

2.1 Controlling inter-strand contact resistance by cold pressing

The first process we applied to break down the intrinsic oxide layer on the Cu surface of the REBCO CCs is mechanical pressing. This work has been published in "YBCO Coated Conductor Interlayer Electrical Contact Resistance Measured From 77 K to 4 K Under Applied Pressures up to 9.4 MPa [88]."

The electrical resistance of a 10-stacks of YBCO tapes were measured. Two different sets of measurements were performed on the samples. The first setup, shown in Fig.18, was used for tests at 77 K under pressures of up to 420 kPa. This equipment consisted of two G-10 plates with up to three steel plates which could be laid over them. The sample stack (ten tapes, 10 cm long) was inserted between the two G-10 plates, and the upper G-10 and steel plates were free to slide up and down but kept in place horizontally with the vertical guides as shown in Fig. 18. Pressure

was applied by adding a series of steel weights (plates) to the top of the upper G-10 plate of the setup. Each steel weighs 5.68 kg, supplying 55.7 N, giving 139 kPa per steel weight applied onto the REBCO tape stack with cross section of 10 cm*0.4 cm. Up to three steel plates applied on the tape stack resulted in a maximum pressure of 417 kPa. The rig sat in a closed foam box cryostat and LN2 was used to cool the rig. The level of LN2 was controlled so as to immerse the bottom G-10 and to be in contact with the bottom Cu, but not to touch the sample. A current of 0.1 A was applied between two copper plates that the REBCO tape-stack was sandwiched in between, and the voltage was measured between the two Cu plates. Cernox sensors were present on the upper and lower plates and were monitored.

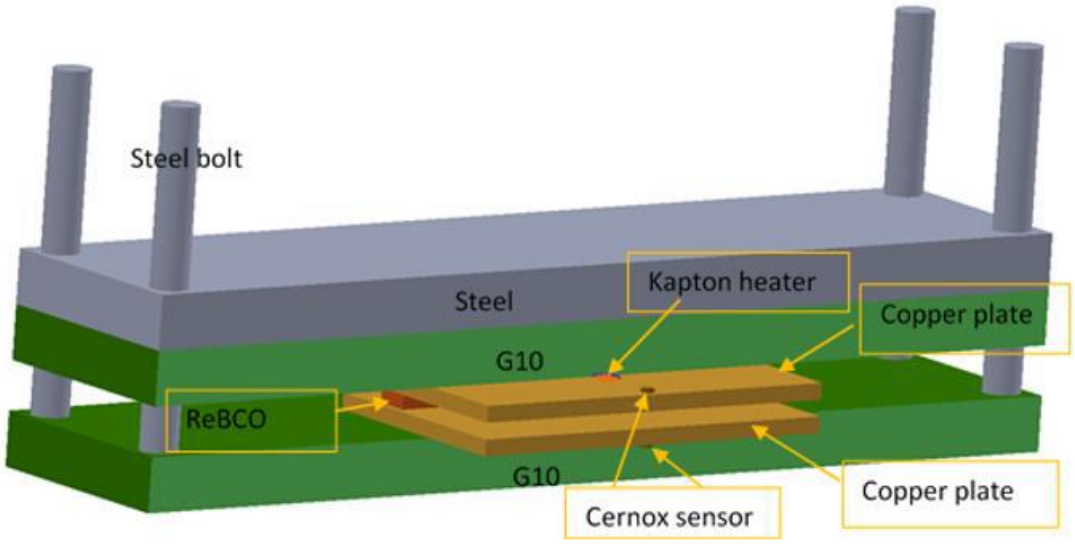

Figure 18:Rig 1, lower pressure range, fixed pressure inter-tape resistivity measurement.

We expected the native oxide which forms on metal surfaces is a key contributor to the electrical contact resistance. This native oxide layer is known to be ~4.5 nm thick for Cu. The application of mechanical pressure is known to modify the electrical contact [87] [89] [90]. This

is borne out in the results of our measurements from Rig 1, as presented in Fig. 19. Here the stack resistivity (resistance) decreased as pressure increased. At low applied pressures and 77 K, we can see that the resistance of the stack decreases from 0.234 Ω (no pressure) to 0.029 Ω (417 kPa). If we assume that the contact resistance at the tape surface dominates the stack resistance, then in terms of η this is 0.935 $\Omega * \mathrm{cm}^2$ (at zero applied pressure) to 0.1 $\Omega * \mathrm{cm}^2$ (at 417 kPa). Compared with the scenario without pressure, the resistance (contact efficiency) of the stack drops by a factor of 8 with 417 kPa applied. This η value is about 40 X higher than that measured for Cu surface NbTi strands under 77 MPa (~ 300 $\mu\Omega * \mathrm{cm}^2$) [91], and 23 X higher than the chrome plated REBCO conductor (~ 564 $\mu\Omega * \mathrm{cm}^2$) under 200 MPa pressure [87].

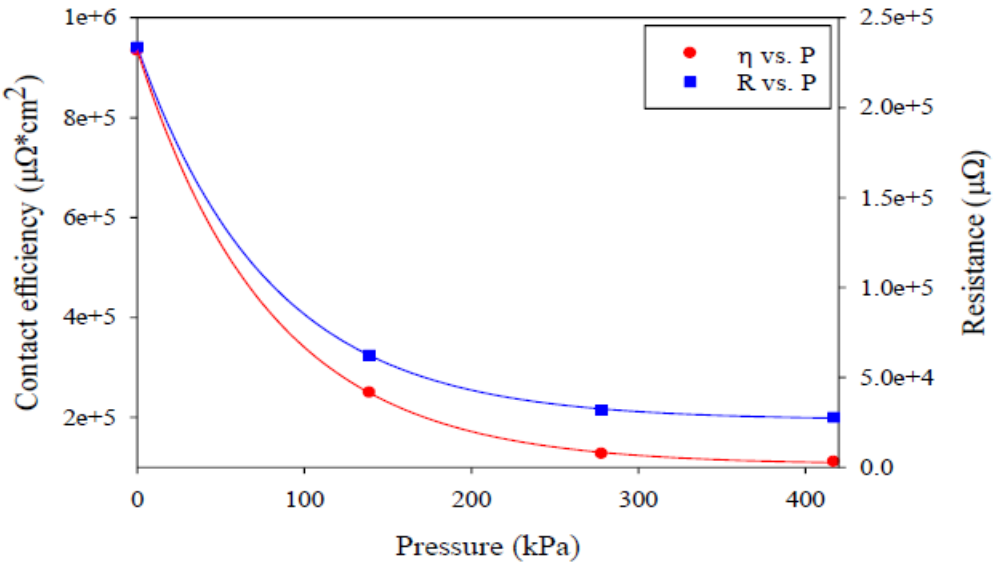

Figure 19: Stack resistance and contact efficiency vs applied pressure at 77 K.

The second rig, capable of variable temperature measurements as well as higher compaction pressures was used for a second round of experiments. The probe consisted of two copper shims, one on the top and the other on the bottom, com-pressed by G-10 plates pressurized with screws, see Fig. 20.

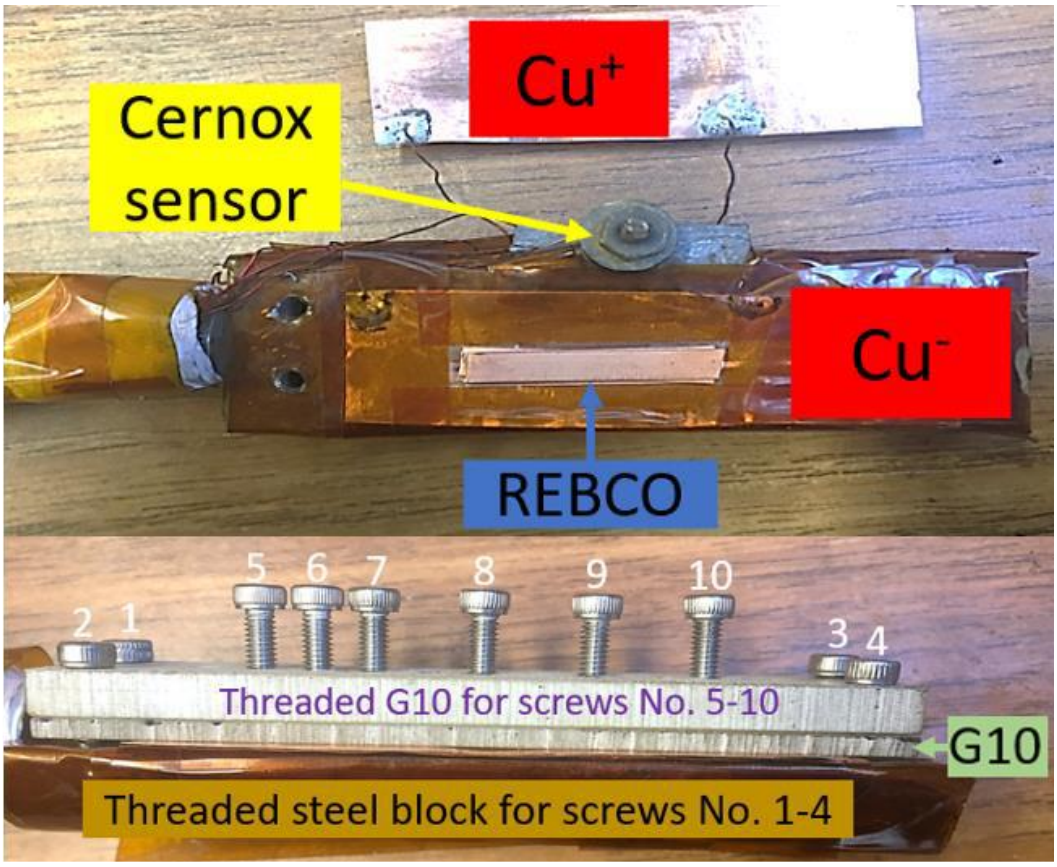

Figure 20: Rig 2, higher pressure range, 4 K-77 K, applied constraint inter-tape resistivity measurement.

A 10-layer tape stack, 2.4 cm in length, was placed on the top of the bottom copper shim, which was electrically insulated from, but in good thermal contact with, the Cu support plate that the G-10 is bolted to. The tape stack was sandwiched between the upper and lower Cu shims. One Cernox sensor was installed at the middle of the probe to monitor sample temperature. Screws No. 1 through 4 were used to position the setup and were tightened to the bottom Cu support block. The G10 had an upper (fixed) and lower (movable) plate. The top G10 piece was threaded so that screws No. 5-10 could be driven through it and therefore apply a certain pressure to the bottom G10 piece across the tape stack. In addition to the pre-stress introduced by positioning the setup through screws No.1-4, pressure (pre-stress) of 4.97 MPa, 6.63 MPa, 8.31

MPa, and 9.94 MPa were applied sequentially to the tape stack by utilizing a precision torque driver. For each pressure, we used a (virgin) tape stack. Pressure was applied at room temperature, and then the sample probe was inserted into a half-filled liquid helium tank and the sample could be cooled to between 4.2 K to 77 K by selecting the height of the probe above the helium. The temperature gradient has been measured for this probe and is less than 0.3 K along the length of the sample.

It is important to note that the method of pressure application is in a pre-stress mode. That is, the pressure is applied at room temperature, and acts as a constraint. When the probe is cooled down, the probe, as well as the tape stack undergo thermal contraction, which modifies the level of applied pressure. This protocol, which a variety of published articles have used [87] [90] [91], does mean that the pressure applied to the stack is some-what different than what was applied at room temperature. We can make an estimate of the change in applied pressure by making estimates of the thermal contraction of the sample and the holder, and using the modulus of the tape stack, estimate the change in applied pressure. However, it should also be noted that in some ways the applied constraint protocol is more interesting and relevant for actual magnets, since magnets will be fabricated with an applied constraint, and then cooled down to the point of operation.

Under a nominally zero applied pressure at 4.2 K, η = 5400 $\mu\Omega * \mathrm{cm}^2$, dropping to 178 $\mu\Omega * \mathrm{cm}^2$ at 9.94 MPa; at 77 K η ranged from 6900 $\mu\Omega * \mathrm{cm}^2$ at no applied pressure to 232 $\mu\Omega * \mathrm{cm}^2$ at 9.94 MPa. The temperature dependence for samples measured under nominally zero pressure is given in Fig. 21 (a), and the temperature dependence for various applied pressures in Fig. 21 (b). The η value at 9.94 MPa is comparable to that of the Cu surfaced NbTi strands under 77 MPa

[91] and the Cu surfaced REBCO strands under 20 MPa [87]. Previous measurements on NI coils yielded η varying from 20 $\mu\Omega * cm^2$ to 70 $\mu\Omega * cm^2$ [90] [92], this level of contact efficiency is achievable by applying compressive force without degrading the performance of the REBCO superconducting tapes and coils (~261 $\mu\Omega * cm^2$at 140 MPa [93], ranging from 16 $\mu\Omega * cm^2$ to 180 $\mu\Omega * cm^2$ at 20 MPa under varying cyclic loading [94], ~1 $\mu\Omega * cm^2$ at ~2 MPa for a solenoid coil [95]).

As noted above, the thermal contraction of both the stack and the rig modifies the pressure as applied at cryogenic temperatures. We can make an estimate for this pressure modification (which can be thought of as an error in the nominal pressure) in the following way. Let us estimate the error at 4.2 K. The thermal contraction (*ΔL/L*) for Cu, Steel, Hastelloy, and G-10 are $3.2*10^{-3}$, $3.0*10^{-3}$, $2.4*10^{-3}$, and $2.45*10^{-3}$, respectively. The contraction of the active length of the four corner screws will result in compression, while the contraction of the tape stack and the contraction of the top and bottom G10 plates will lead to relaxation. The YBCO coated conductor consists of 40 μm Cu, 50 μm Hastelloy, and 10 μm YBCO+buffer. Here we only take Cu and Hastelloy into consideration, so based on the fractional thermal contraction factors, the total contraction of the tape is ~$2.4*10^{-3}$ mm (0.128 mm for Cu and 0.12 mm for Hastelloy). Similarly, the contraction of the two top G-10 pieces (7.67 mm total thickness) in total is $1.9*10^{-2}$ mm. When applying pressure the top screws extended about 1.5 mm, so the contraction of the pressing screws is $4.5*10^{-3}$ mm. The four corner screws will also shrink, and the portion that can affect the pressure on the sample is the total thickness of the (two G- 10)+(the sample stack) which is 7.67+1 = 8.67 mm, so the contraction is about $2.6*10^{-2}$ mm. Hence, the resultant total thermal contraction is $2.6*10^{-2}$ mm - $4.5*10^{-3}$ mm - $1.9*10^{-2}$ mm - $2.4*10^{-3}$ mm = $1*10^{-4}$ mm. A

similar calculation at 77 K gives a larger value (2.25 x 10^{-3} mm), so we take that as our error limit. In order to use this number, we must measure the modulus of the stack, or rather its compression-pressure curve. The modulus of the tape stack is much different from the tape itself, because the tapes in the stack are not completely flat and straight, even as carefully assembled into a pack. The initial compression, or pre-stress as applied to the pack serves to compact the ten-layer stack, removing gaps. Only when fully compacted will the pack behave like the individual conductors. We measured the effective modulus in the low pressure regime to be 17.6 MPa with the initial ten stack thickness of 1.82 mm. This leads to an error in the pressure of ~21 kPa. Therefore, in comparison with the applied pressure from 4.97 MPa to 9.94 MPa, the error due to thermal contraction is small, and we report the results in terms of nominal pressure in Fig. 21 and 23.

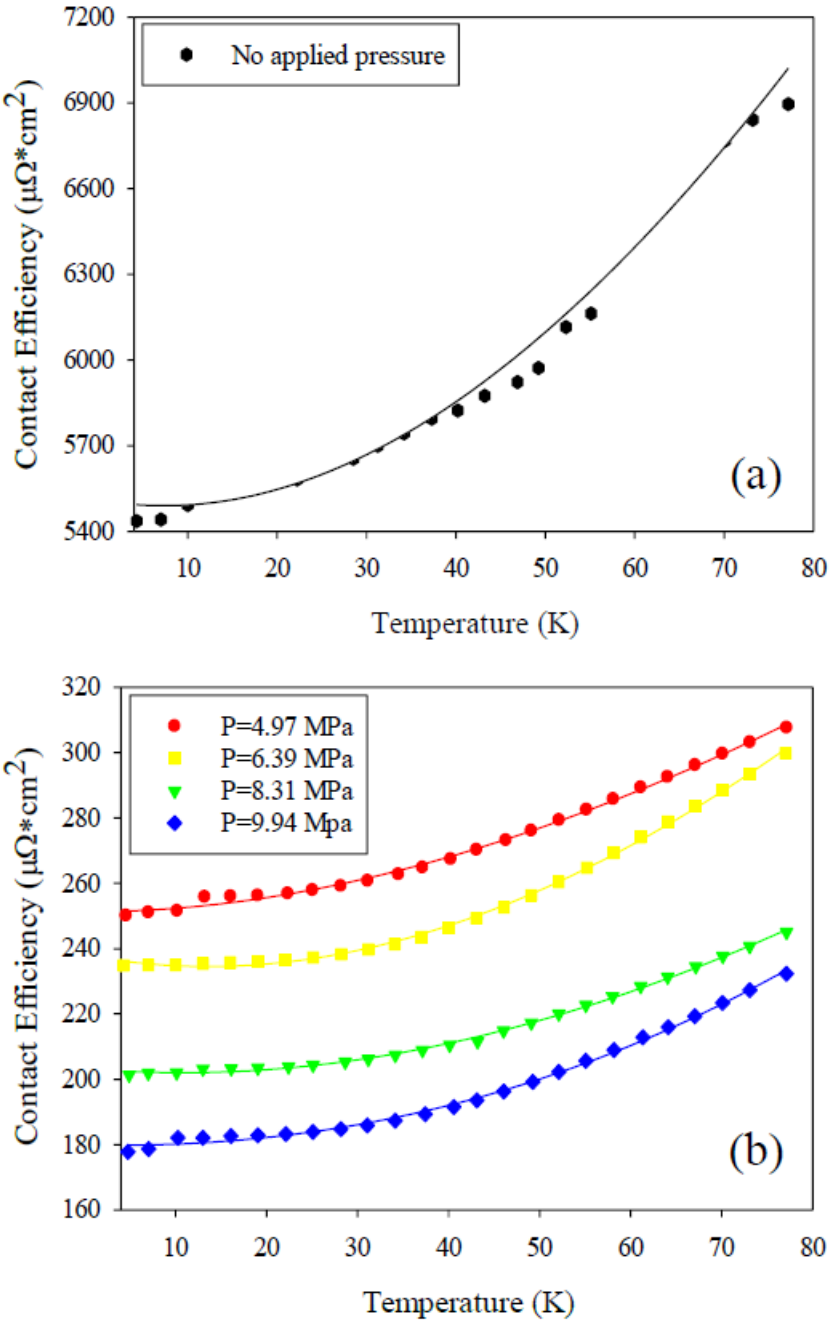

Figure 21 :(a) Contact efficiency vs temperature without external pressure, (b) Contact efficiency vs temperature at 5-10 MPa.

Fig. 22(a) demonstrates that the measured resistance across the stack is dominated by surface contact rather than the strand internal resistance. In flowing through this stack, the current must of course pass through every tape-to-tape interface, experiencing the interface

contact resistance 9 times. In addition, there is also the bulk resistivity as the current flows through the tape. Let us consider the tape to be a network of three parallel resistors, one associated with the Cu on each of the tape edges, and one associated with the central region (containing the YBCO and Hastelloy, as shown in Fig. 22). As shown there, the average thickness of the plated copper near the tape edge was 34.4 μm. We calculated the resistance of the copper path based on $R = \rho L/A$. At 77 K, ρ of copper is 22.2 μΩ*cm, the path length L is 0.1 cm, and the cross-section area is $2 \times 3.44 \times 10^{-3} \times 2.4$ cm^2. Therefore, the copper path resistance is calculated to be 1.34 μΩ at each edge of the tape, or 0.67 μΩ per tape based on the edge conduction. The conduction through the tape middle is smaller than this contribution, but would in any case tend to reduce the resistance per tape even further. The total resistance of the tape stack based on these internal contributions would be 6.7 μΩ. If the current spread out along the interface between tapes to minimize interface contract resistance, this number would be on the order of 40 X higher, based on a current path along the tape width instead of along its thickness, which leads to an upper bound for the contribution of the internal resistance components to the ten stack resistance of 268 μΩ. Comparing with resistance across the stack which is 2.15 mΩ based on our direct measurement, the copper path resistance is negligible, and therefore we can conclude that the measured resistance is mainly the contact resistance of the tape surfaces.

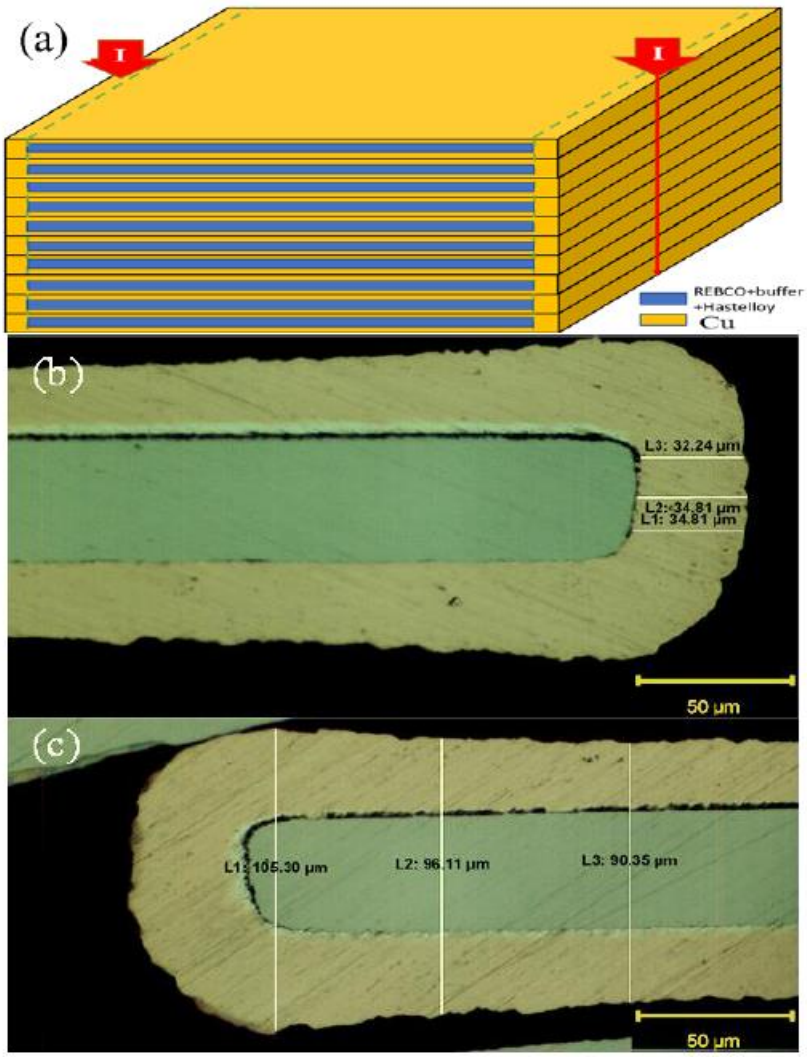

Figure 22: (a) Schematic of Coated conductor stack showing majority of current flow passing through the tape edges (Cu). (b) Optical microscopy of the tape cross section near the tape edge. (c) Thickness along the tape.

We note that the η is slightly dependent on temperature; it is interesting to consider if this is due to the intrinsic properties of the oxide layer. As noted before, there is also a decrease with applied pressure. It can be noticed that there is a significant difference in contact efficiency for the two nominal non-pressurized cases measured in Rig 1 and Rig 2. This error is likely due to differences in the nominal "zero pressure state" for these two measurements. Indeed, as shown in Fig. 23, η drops quickly with increasing pressure in this low applied pressure regime, flattening

out at higher pressures, where the agreement is better, and also the agreement with previous measurements on both Cu-surface REBCO stacks [87] [90] [93].

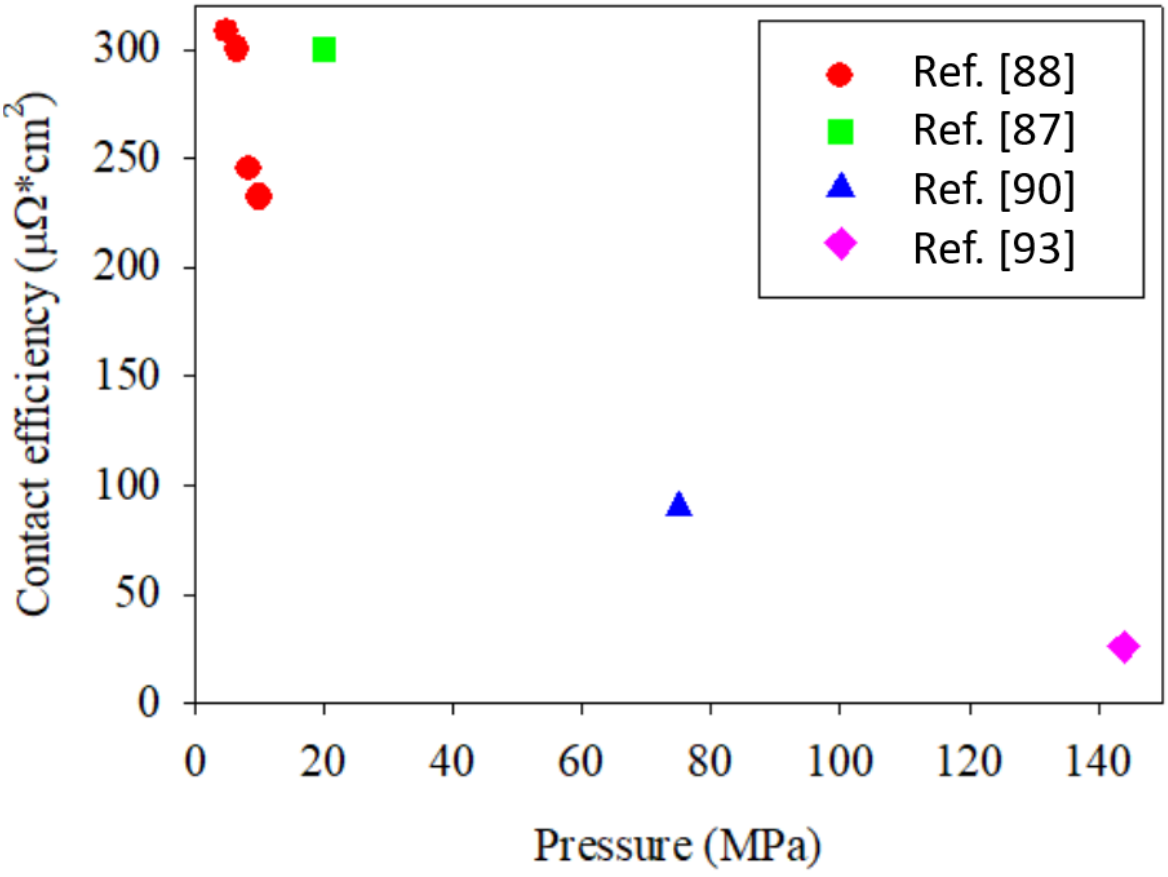

Figure 23: Contact efficiency vs nominal applied pressure at 77 K.

2.2 Controlling inter-strand contact resistance by hot pressing

A η of 180 $\mu\Omega * cm^2$ was achieved under a pressure of 10 MPa. However, based on some 2D simulation studies, the onset value of η that can initiate effective current transferring in a REBCO tape stack is around 10 $\mu\Omega * cm^2$ [96] [97] [98]. Hence, we tried hot pressing to further decrease η between REBCO CCs.

The hot pressing protocol has been published in the paper titled as "Electrical Contact Resistance in REBCO Stacks and Cables With Modified Surfaces [97]." Ten-layer REBCO coated

conductor tape stacks with a length of 2.4 cm were sintered in the setup depicted in Fig. 24. The two end screws were used to hold the fixture. Using a precision torque wrench pressures from 15 MPa to 33.4 MPa were applied by the top 5 screws (Major diameter = 4.170 mm) to the middle steel plate and hence the planar stress could transfer to the tape stacks. Although the real thickness of REBCO CCs can vary along the length and width, in this study, we assumed the stress was uniformly distributed along with the tapes. For heat treatment under Ar, the stacks were ramped at 10 °C/min to 300 °C, held for 30 min, and furnace cooled. The applied torque is converted to force based on $\tau = c * D * F$, where τ is the applied torque, c is the coefficient of friction of threads with the subscripts specifying different contacts ($c_{steel-steel}$ = 0.42, $c_{steel-G10}$ = 0.21), D is the major diameter of the bolt, and F is the resulted axial force.

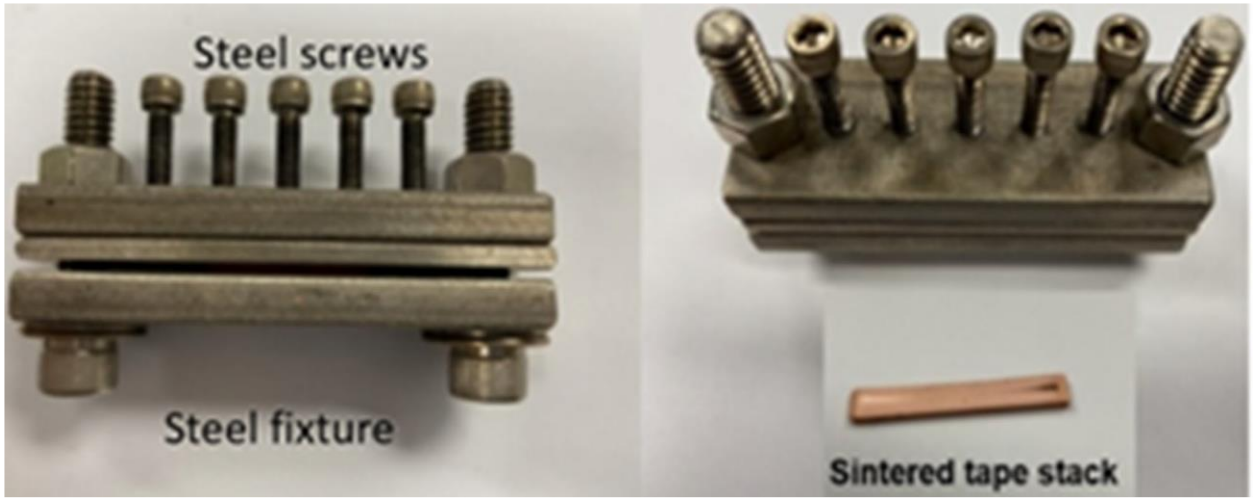

Figure 24: Heat treatment setup made with steel.

During the coil winding of a solenoid magnet, the applied tension can result in radial compressive stress in the range of 20-60 MPa [99]. For a dipole magnet, the winding forces are different. But, in any case, when the coil is operating, Lorentz force will generate radial stress in the range of 1

0-50 MPa to the cables [100]. Hence, we chose 15-33.4 MPa for heat treatment and 13.3 MPa for all the measurements.

As listed in Table 2, five 10-layer tape stacks were heat-treated under different pressures at 300 °C for 30 min. Then the tape stacks were released, transferred to the measurement rig, Fig. 20, and measured under 13.3 MPa. Sample S1, consisting of 10 layers of as-received REBCO coated conductor tapes and measured under 13.3 MPa from 4.2 K to 77 K without any pre-treatment, was used as a baseline reference.

Table 2: Heat treated and Ni-plated samples

S1	Cold press sample; measured under pressure 13.3 MPa
S2	Heat treated sample, 20 MPa, measured under pressure 13.3 MPa
S3	Heat treated sample, 23.4 MPa, measured under pressure 13.3 MPa
S4	Heat treated sample, 26.7 MPa, quenched; measured under pressure 13.3 MPa
S5	Heat treated sample, 26.7 MPa, measured under pressure 13.3 MPa
S6	Heat treated sample, 33.4 MPa, measured under pressure 13.3 MPa
S7	Ni-plated sample; measured under 13.3 MPa

The minimum treatment required to build metallic bonding between tape surfaces was found to be 20 MPa at 300 °C. Although previous research showed that the crystal structure and lattice parameter change of REBCO in an oxygen deficient environment starts at a temperature above 530 °C [101], the critical current decreased as the REBCO CCs were heated to about 195 °C as a result of the oxygen out-diffusion effect [102] [103]. However, we performed only low current

measurements. Tests on the heat-treated tape revealed an onset critical temperature of about 90 K, which is similar to that of the as-received tape.

Looking at the results, we find η for S1 is 106 $\mu\Omega * \mathrm{cm}^2$ at 4.2 K and 145 $\mu\Omega * \mathrm{cm}^2$ at 77 K under a pressure of 13.3 MPa. However, a further increase of pressure up to 200 MPa did not significantly reduce η which remained ~ 100 $\mu\Omega * \mathrm{cm}^2$ at 77 K [90]. As shown in Fig. 25(a), in response to heat treatment under pressure above 23.4 MPa, the values of η of samples S3, S5, and S6, dropped to around 10 $\mu\Omega * \mathrm{cm}^2$ at 4.2 K and 19 $\mu\Omega * \mathrm{cm}^2$ at 77 K. Increase of pressure from 23.4 MPa to 33.4 MPa did not produce any further lowering of the η. It is interesting to note that S4's η was higher than that of any other sample sintered under pressure higher than 23.4 MPa over the entire measuring temperature range. This is because S4 had been quenched instead of furnace cooled. Evidently, furnace cooling favors an ICR reduction.

It can be observed that the ICR of the heat-treated sample increased with temperature. However, the changes in the measured ICR values with respect to temperature for sintered tape stacks, S3, S5, and S6, were smaller above 40 K than those of S1 and the samples described in [88]. We normalized the ICR data of each sample (S1-S6) to their corresponding ICR value measured at 4.2 K and presented the results in Fig. 25(b) as $\eta_T/\eta_{4.2}$. As the temperature increases, we observed some divergence of the curve envelopes, due to the fact that the contribution of the metal stabilizer resistance is also included with these ratios. However, the fact that the divergence is much smaller than the normalization ratios suggests that the main mechanism for the ICR reduction is a "cleaning" of the surface – a reduction in the area coverage of the surface

oxide layer by sintering. That is, ICR reduction can be explained at the zeroth order by the reduction of intrinsic surface oxide in the oxygen deficient environment at 300 °C [104].

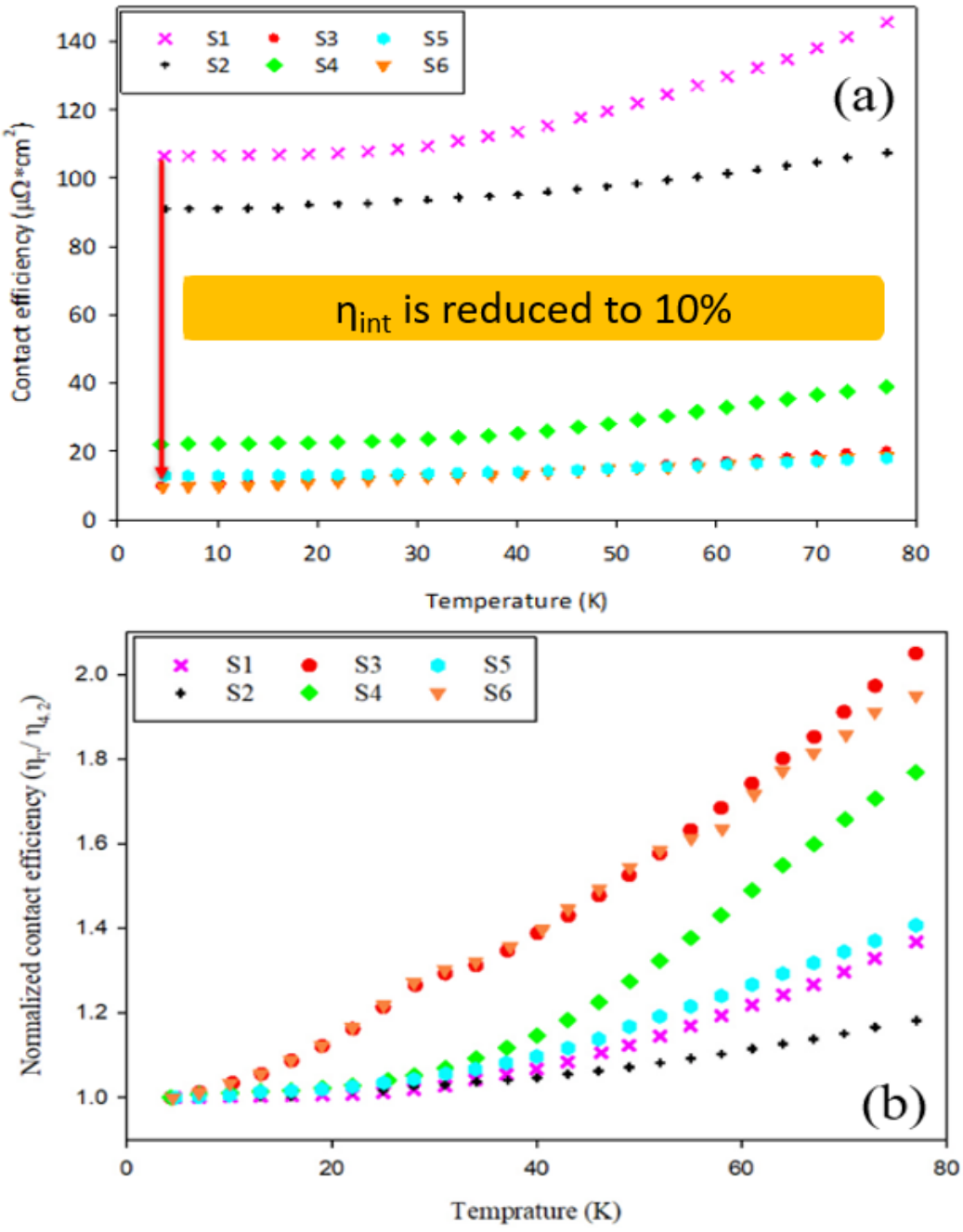

Figure 25：(a) ICR reduction from heat treatment, (b) normalized ICR.

2.3 Controlling inter-strand contact resistance by Ni-plating

Although the hot pressing process can provide an η that satisfies the onset requirement of effective current transferring from one REBCO CC tape to another, this technique can only be used at the sacrifice of the I_c of the conductor. Therefore, I tried the Ni-plating process.

Ni-plating was performed using the standard two-electrode configuration depicted in Fig. 26. Two 99.6% Ni plates (anode) on each side of the REBCO coated conductor tape (cathode) were deposited. A magnetic rotor was used to agitate the solution, reduce dendrite formation, and remove gas bubbles. The plating solution consisted of:

- $NiSO_4 \cdot 6H_2O$ (223.5 g/L)
- $NiCl_2 \cdot 6H2O$ (72.5 g/L)
- H_3BO_3 (39.5 g/L)

The solution was adjusted to a pH ~3.71, and no leveling agent was added. We tried different plating temperatures from room temperature to 40 °C and varying processing time ranging from 10 min to 30 mins with a current density of 20 mA/cm^2. For the particular sample shown in Fig. 27, we performed the Ni-plating at room temperature for 10 min, and thickness of the Ni layer is 10 µm.

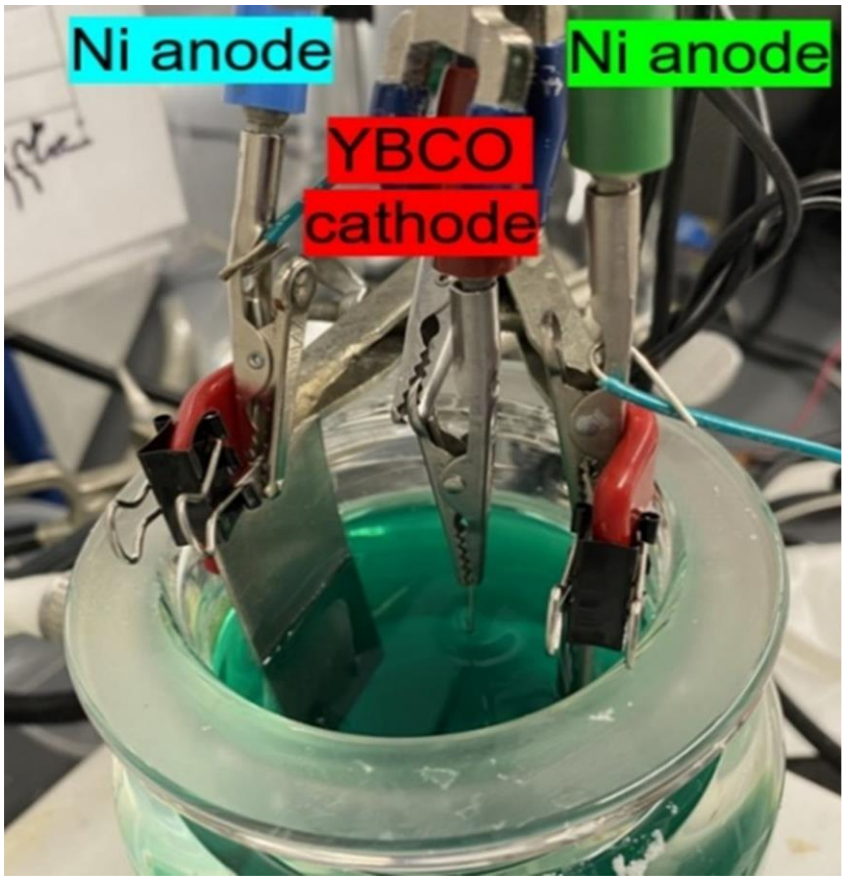

Figure 26:Nickel plating setup

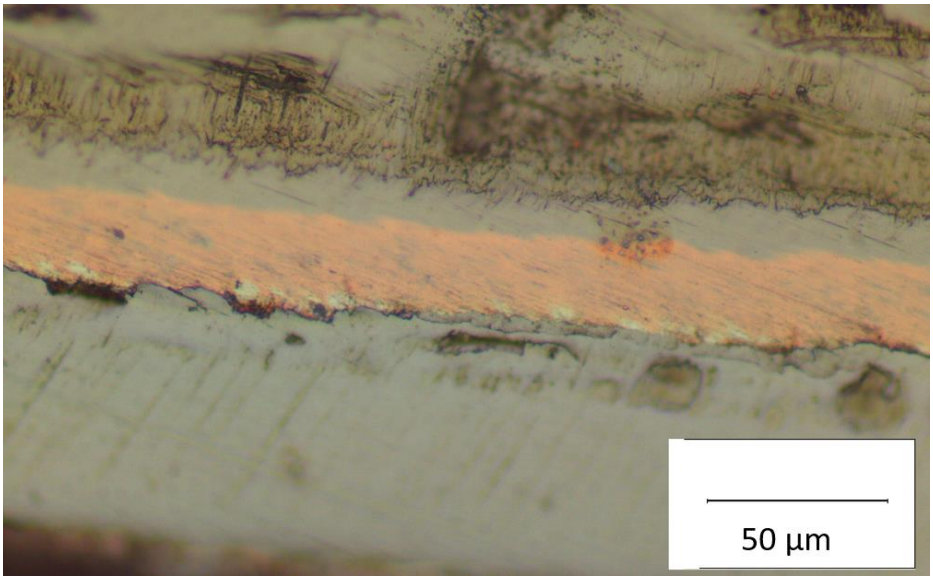

Figure 27: Ni-plated REBCO CC

The aqueous plating solution described above in the previous section was acidic with a pH of about 3.71. Moreover, the Cl^- content in the solution was very high, almost that of a saturated aqueous solution of $NiCl_2$. The YBCO coated conductor tape was immersed in the solution for about 3 min prior to plating. A magnetic rotor immersed in the plating bath, agitated the acidic solution containing a high concentration of Cl^-, and was able to assist in the removal of the passivation layer (mainly CuO) on the tape surface.

After plating, the tapes were placed in air for 30 days to fully develop a native oxide layer on the Ni surface before they were assembled into a tape stack for measurement. To ensure a minimal impurity level, no leveling agent was used in the process. As a result, the surface roughness after Ni plating was similar to that of the as-received tape, as shown in Fig. 28. Measurements depicted in Fig. 29 showed the η_{int} of the 10-layer Ni-plated REBCO coated conductor tape stack to be 2.7 $\mu\Omega * \mathrm{cm}^2$at 4.2 K and 4.6 $\mu\Omega * \mathrm{cm}^2$ at 77 K. Also, the temperature dependence of η was low, even lower than those of the sintered samples. We ascribed the reduction of ICR to the thinner native oxide layer on the Ni surface ($\sim$1 nm) compared to that on the Cu surface ($\sim$4 nm) [91] [105]. In addition, because the samples were measured under 13.3 MPa of compression, a thinner native oxide could facilitate the breakdown of the passivation layer, and a lowering ICR.

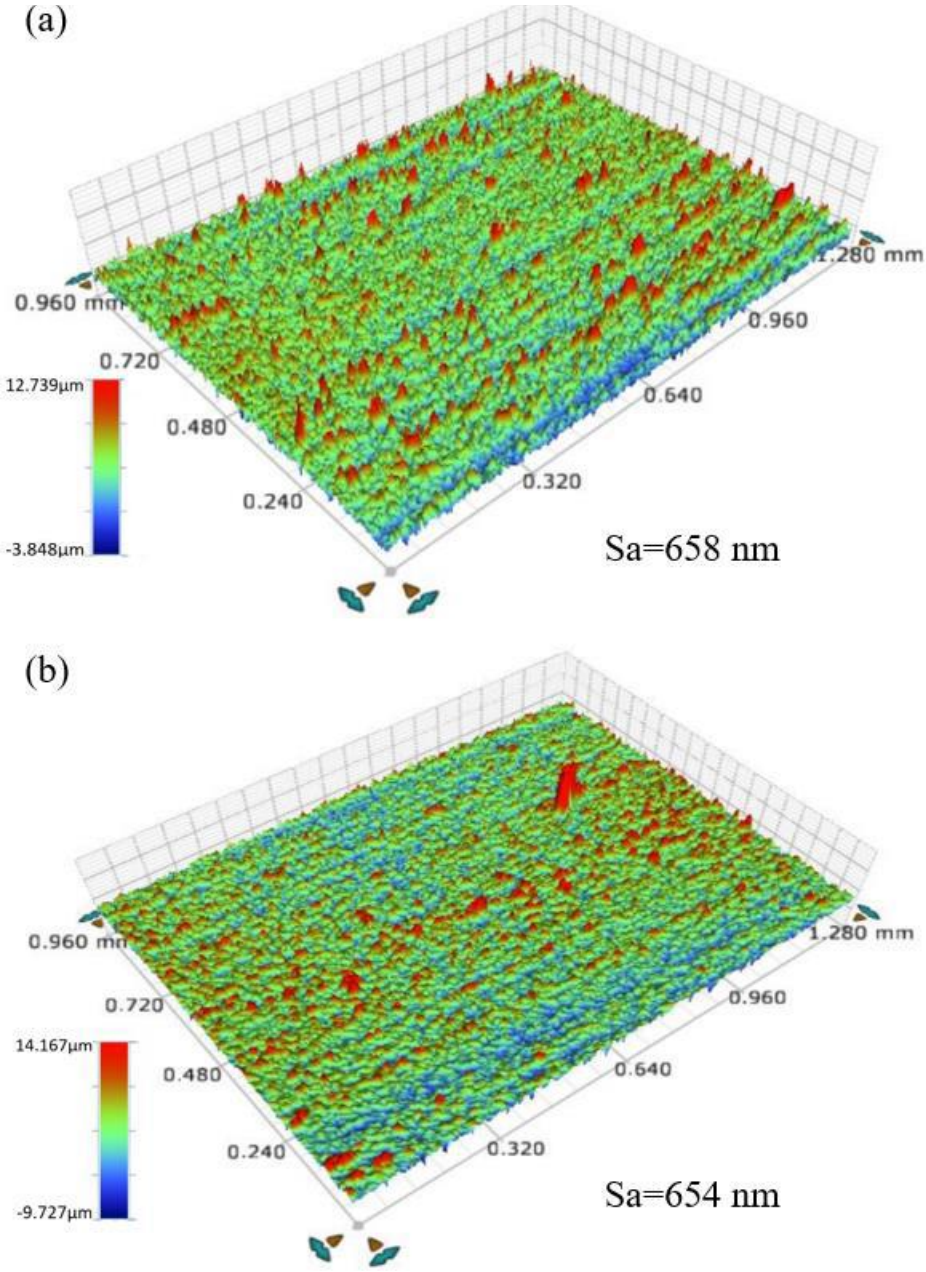

Figure 28: Surface roughness (Sa, the arithmetical mean height) measurement for a) as received YBCO coated conductor tape and (b) Ni-plated tape.

In combination with the results of other studies by our group [96] [88], Fig. 30 depicts the values of ICR achieved through various processing techniques and how these values relate to current sharing in a particular REBCO coated conductor coil model [96]. In Fig. 30, the term, loss power in defect, is the power dissipated in a localized defect that occurs in one of the turns of a

coil. Therefore, for a given size defect (which does not change) a lower power loss means that the current is bypassing the defect more readily without causing large power dissipation because of the lower ICR (i.e., the coil has a better current sharing ability). Based on the simulated results, power loss in a defect will start to decrease when the η is smaller than 10 $\mu\Omega * \mathrm{cm}^2$, and this regime can be achieved by the aforementioned two techniques (sintering and Ni plating). Of course, the specific curve shown is for a particular coil, different coil geometries (or cables) would have different curves, but in any case, a comparison of such curves with achievable ICR values is of value. Further work on the control of ICR and modeling of current sharing/protection vs η is ongoing.

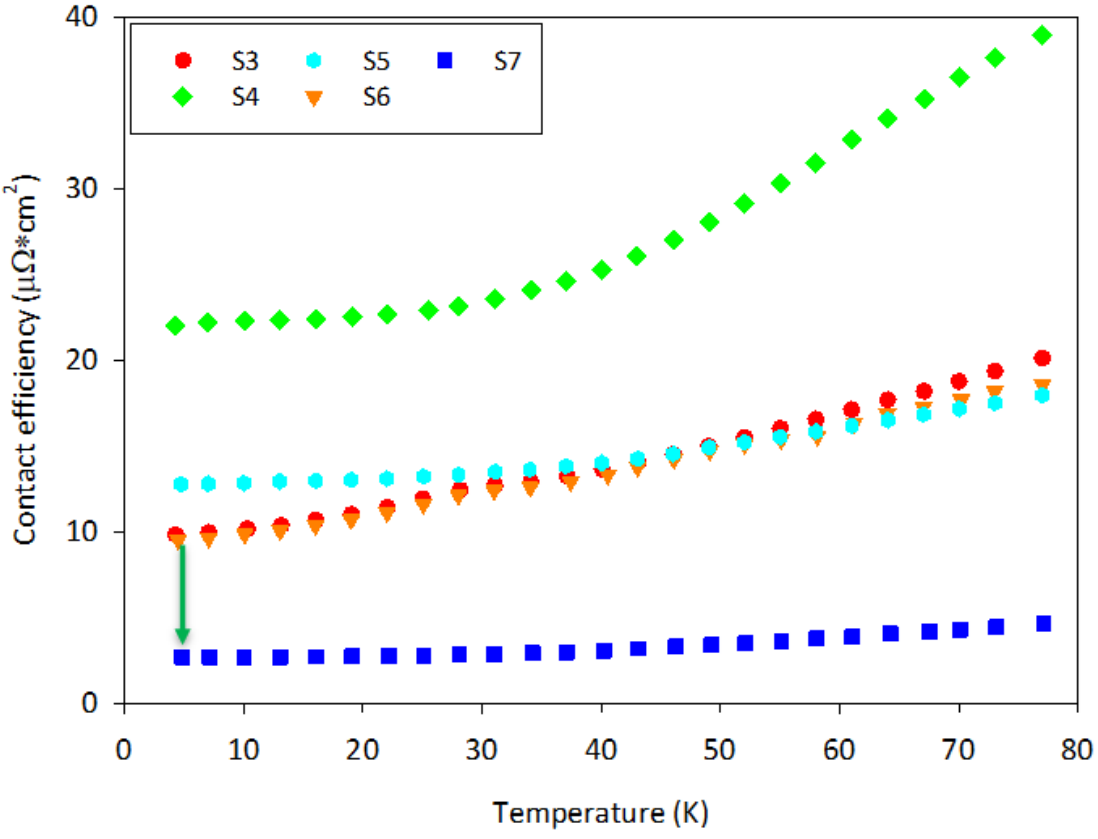

Figure 29: ICR reduction from Ni-plating

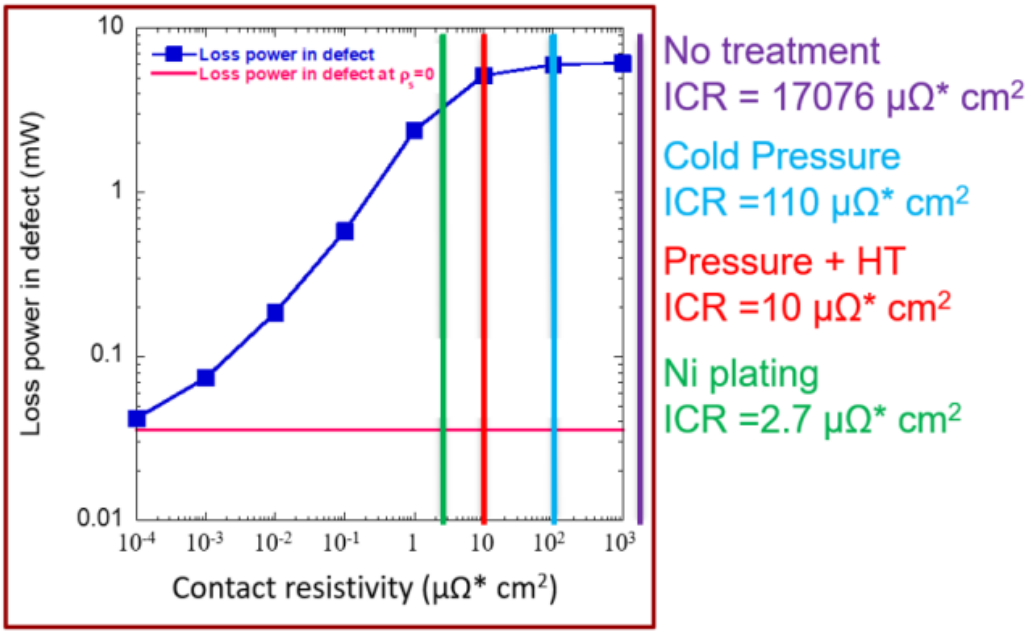

Figure 30: ICR from different processing techniques and correlation with current sharing ability (Loss power in defect) in a multi-tape YBCO cable

2.4 Controlling inter-strand contact resistance by Ni replacement

From the previous section, we found that Ni-plating can significantly reduce the ICR between REBCO CCs. Therefore, we conceived the idea to replace the Cu stabilizer with Ni. First, we dissolved the Cu layer on the REBCO CCs via an electrochemical process. The REBCO CC was connected to the anode and was immersed in an electrolyte consist of 1 M H_2SO_4 and 0.3 M $CuSO_4 \cdot 5H_2O$. A Cu rod was used as cathode, and a saturated calomel electrode (SCE) was used as the reference electrode. By applying a working voltage of 0.15 V, the Cu stabilizer layer could effectively be dissolved in 3 hours while the Ag overlayer could be reserved. Then Ni-plating was performed for 5 min with the same electrolyte introduced in the previous section. The final structure of the processed conductor tape was presented in Fig. 31. The uniformity of the Ag overlayer on the REBCO side was much better than that of the Ag overlayer on Hastelloy side and

had a better surface conductivity. Therefore, the Ni-plating thickness on the REBCO side was ~4.5 µm, while the Ni-plating thickness on the Hastelloy side was ~2.1 µm.

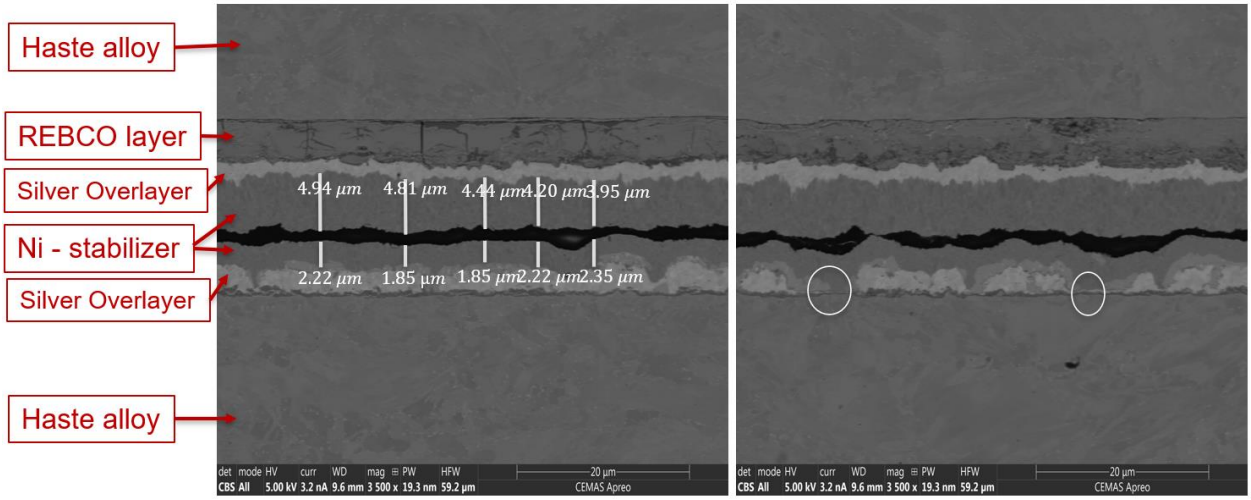

Figure 31: Structure of Ni-replacement sample

Then we made a 10-layer tape stack with the Ni-replacement sample and measured the ICR across the taps stack. As shown in Fig. 32, the measured η is ~40 $\mu\Omega * \mathrm{cm}^2$ at 4.2 K and ~75 $\mu\Omega * \mathrm{cm}^2$ at 77 K. Surprisingly, the measured η of the Ni-replacement sample is about 15 times higher than that of the Ni-plated sample. We ascribed the higher η to the increased surface roughness due to the non-uniformity of the Ag overlayer on the Hastelloy side. The as-received tape had a surface roughness of 658 nm, Fig. 28 (a). As presented in Fig. 33, although the surface roughness of the Ni-layer on the REBCO side dropped from 658 nm to 439 nm, the surface roughness of the Ni-layer on the Hastelloy side increased from 658 nm to 1125 nm.

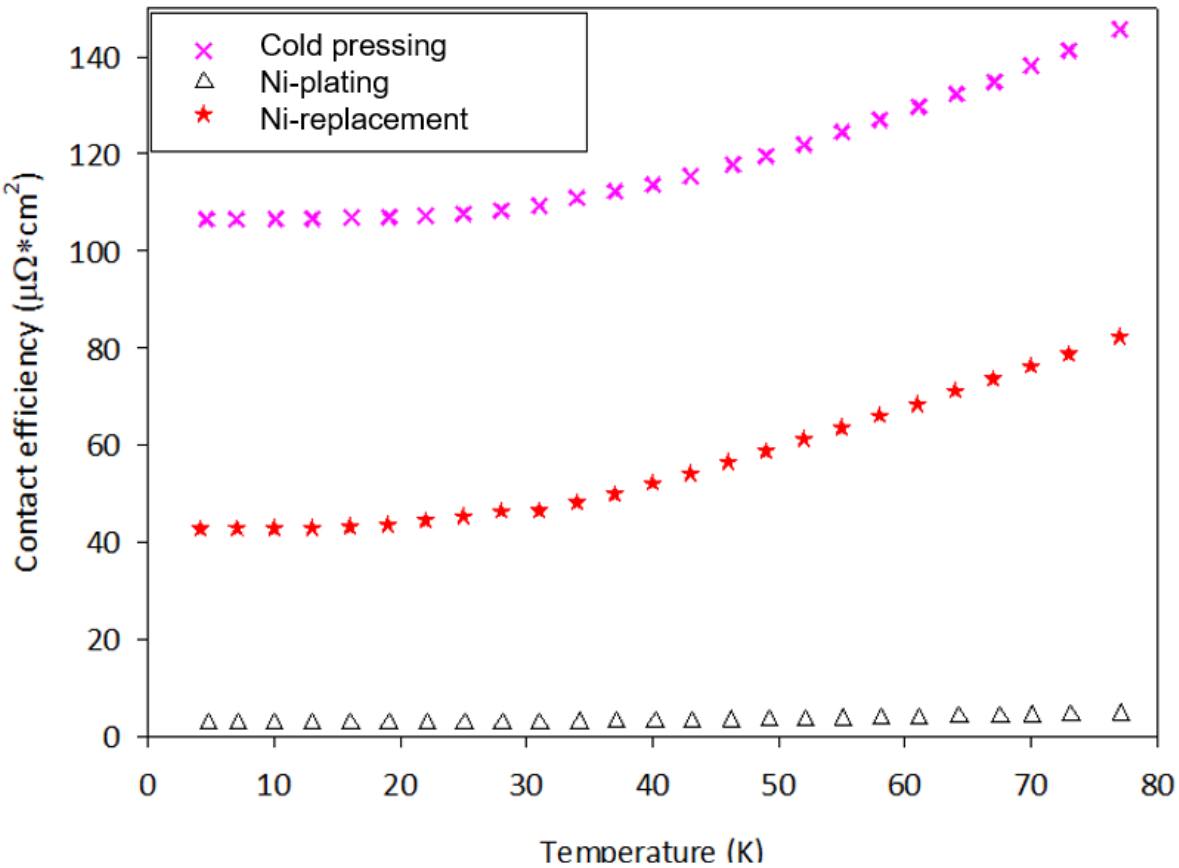

Figure 32: ICR measurement of Ni-replacement sample

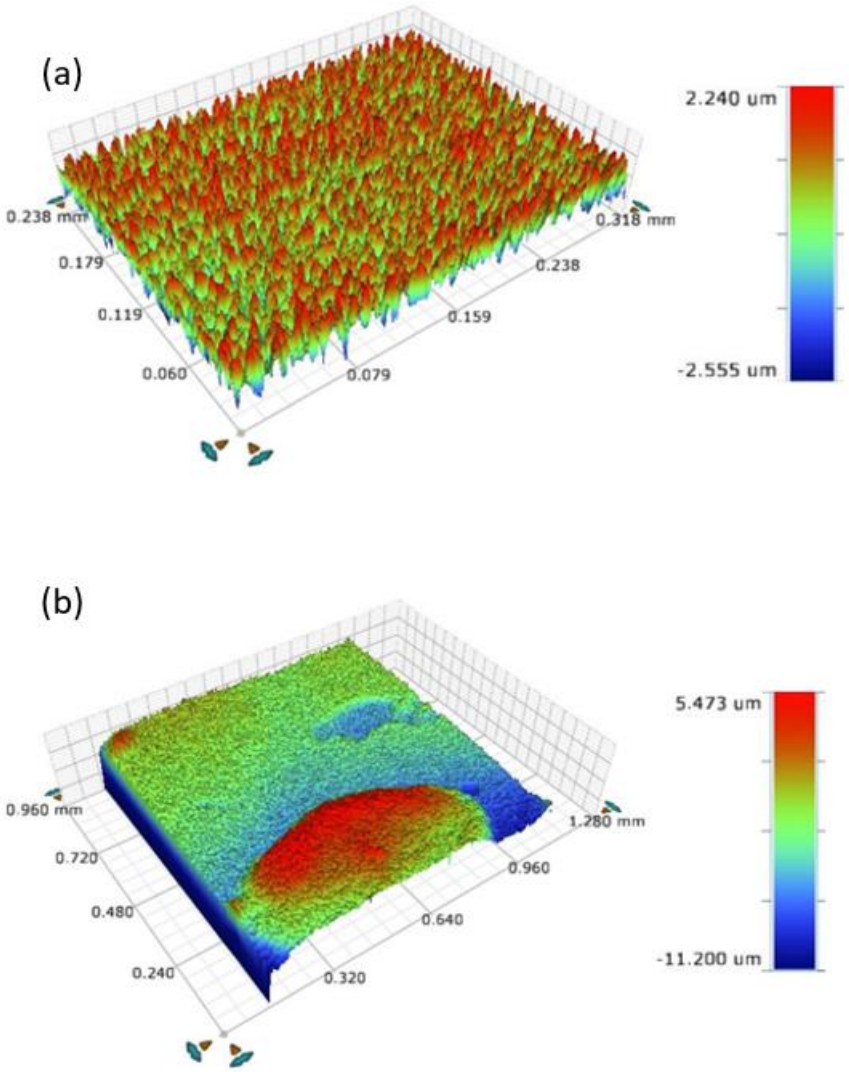

Figure 33:Surface roughness (Sa, the arithmetic mean height) measurement for a) Ni-layer on the REBCO side (b) Ni-layer on the Hastelloy side.

2.5 Controlling inter-strand contact resistance by PANI-coating

The designs of REBCO turn-to-turn magnets or coils mainly follow two concepts, no-insulation (NI) [70] [106] [107] and epoxy impregnation [108] [109] [110]. The no-insulation design can provide good current sharing. On the other side, the epoxy impregnation design can provide mechanical support and the insulating nature of epoxy can reduce the flow of coupling current. In general, these two concepts can give the two extreme values of η, metallic contact and

insulating contact. However, a wide range of η values that can exist in between these two extremes offers a tradeoff between current sharing and coupling current loss. Therefore, achieving a low η is not necessarily an end goal. The value of η should be practically determined by applications.

As material scientists, we seek to provide as many options of η as possible. In addition, the technique needs to be reproducible, easily controlled, and potentially converted into a continuous process for large scale production. Therefore, we developed the conductive polymer coating technique. The conductive polymer we chose is polyaniline (PANI), which has three distinct oxidation states. The molecular structure of PANI is shown in Fig. 34 [111]. When y = 1, it corresponds to the fully reduced state of PANI, leucoemeraldine. When y = 0, it corresponds to the fully oxidized state of PANI, pernigraniline. When y = 0.5, it corresponds to the partially oxidized state of PANI, emeraldine. For each different state there are base and salt forms depending on protonation state, as exemplified in Fig. 35 [112]. Table 3 summarizes the different forms of PANI and their color and electrical conductivities [113].

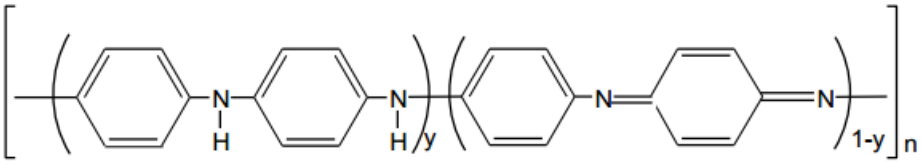

Figure 34: Molecular structure of PANI [111]

Table 3: Different forms of PANI [113]

PANI form	Oxidation protonation state	Color	Electrical conductivity
Leucoemeraldine salt	Reduced and protonated	Transparent yellow	10^{-12} S*cm^{-1}
Leucoemeraldine base	Reduced and deprotonated	Yellow	10^{-12} S*cm^{-1}
Emeraldine salt	Partially oxidized and protonated	Green	10^{-4}-10^{2} S*cm^{-1}
Emeraldine base	Partially oxidized and deprotonated	Blue	10^{-12} S*cm^{-1}
Pernigraniline salt	Oxidized and protonated	Violet	10^{-12} S*cm^{-1}
Pernigraniline base	Oxidized and deprotonated	Violet	10^{-12} S*cm^{-1}

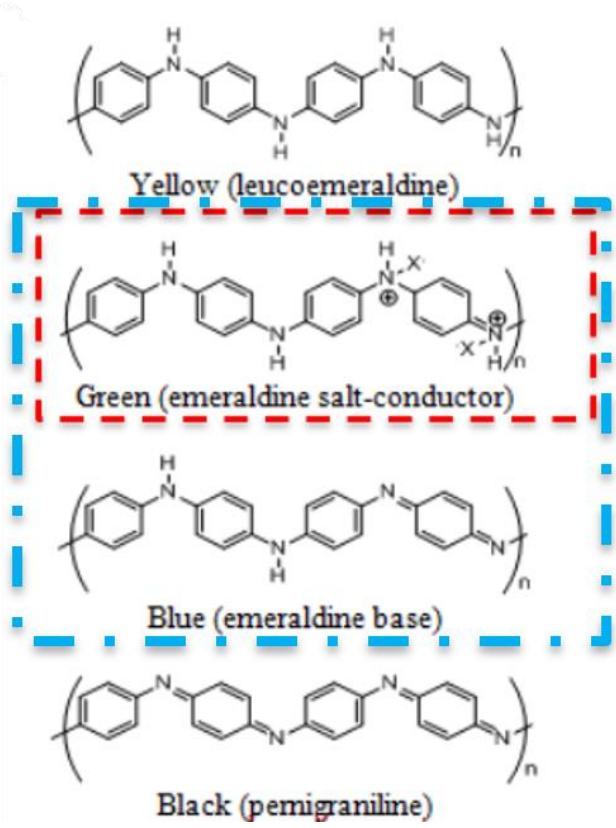

Figure 35: Different forms of PANI [112]

We were particularly interested in the emeraldine salt form of PANI, the only conductive form. It can be synthesized through an electrochemical process at working voltages of from 0.5 V to 0.9 V [111] [112] [114] [115] [116]. A schematic of the PANI coating setup is shown in Fig. 36. The Ni-plated REBCO CC is connected to the anode, a graphite rod is used as the cathode, and a saturated calomel electrode (SCE) is used as the reference electrode. We prepared three different types of electrolytes:

1. 0.5 M H_2SO_4 and 0.3 M Aniline
2. 0.5 M H_2SO_4, 0.3 M Aniline and 0.3 M $CuSO_4 \cdot 5H_2O$
3. 0.5 M H_2SO_4, 0.3 M Aniline, 0.3 M $CuSO_4 \cdot 5H_2O$, and carbon nanotube (CNT)

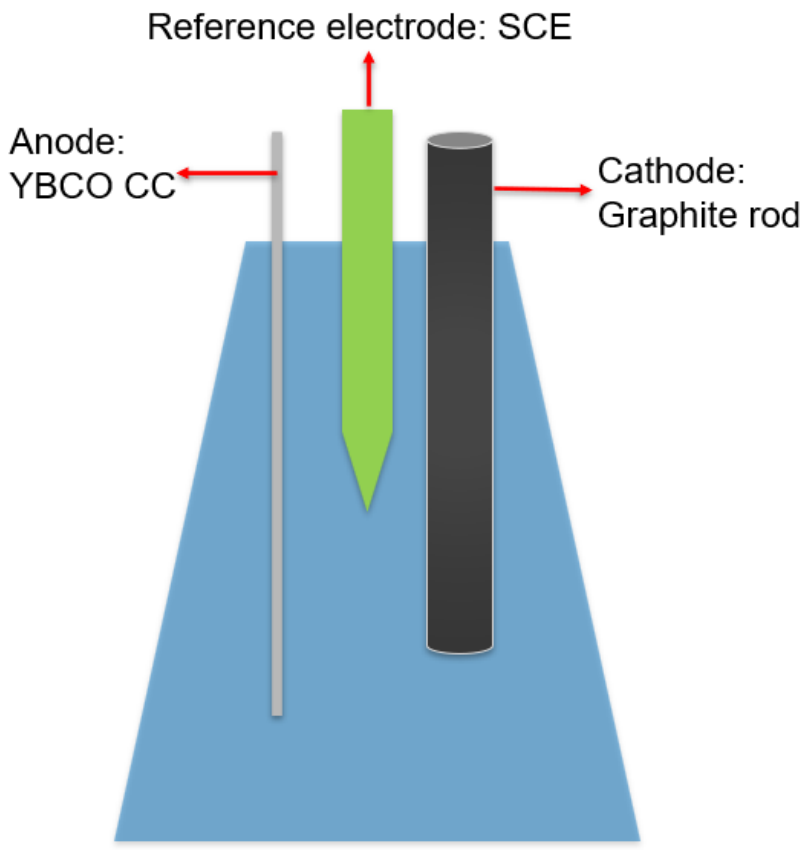

Figure 36: Schematic of PANI coating setup

For all the three electrolytes, we set the working voltage to 0.8 V, at which voltage we can produce a green conductive form of PANI on the tape surface. Because the compositions of the electrolytes are different, the solution conductivities are different. Therefore, we conducted the polymerization process in 3 min for electrolytes 1 and 2, and 1.5 min in electrolyte 3. After the coating process, we made tape stacks of the three types of coated tapes. Each tape stack consisted of 10 layers and was heat treated at 50 ℃ under a compression of 23.4 MPa for 5 hours, a process that turned the loose stack into a solid piece. Then, the electrical contact efficiency, η, of the heat treated stacks were measured in the rig shown in Fig. 20 under a pressure of 13.3 MPa.

Fig. 37, 38, and 39 are the SEM images of the three aforementioned tape stacks. The thickness of the pristine PANI interlayer is ~20 μm. The thickness of the $CuSO_4$ doped PANI interlayer is also ~20 μm. The thickness of $CuSO_4$ doped PANI interlayer with carbon nanotube (CNT) inclusion is ~ 14 μm.

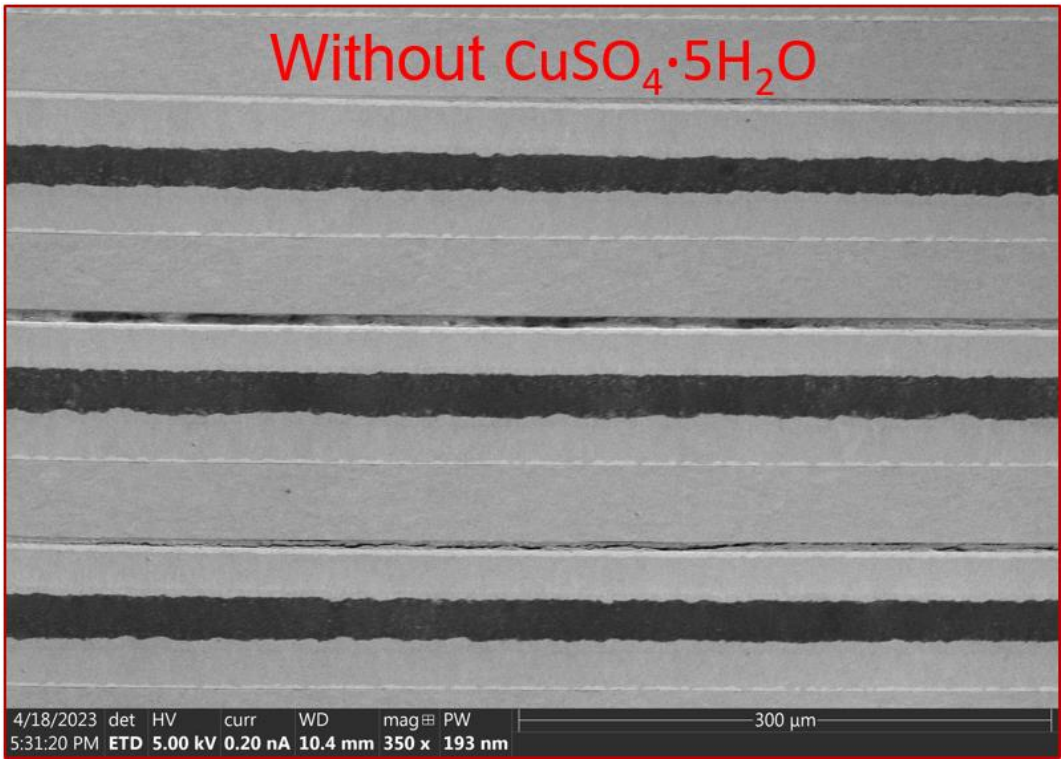

Figure 37: PANI coated REBCO CC tape stack.

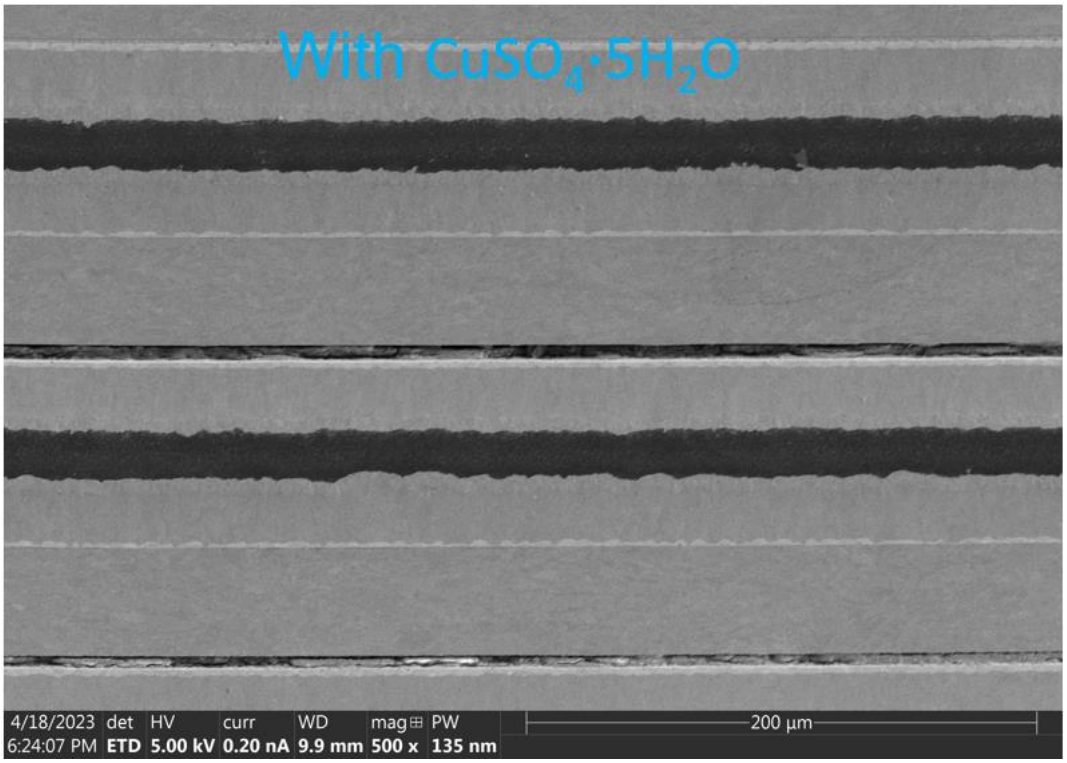

Figure 38: PANI ($CuSO_4$) coated REBCO CC tape stack.

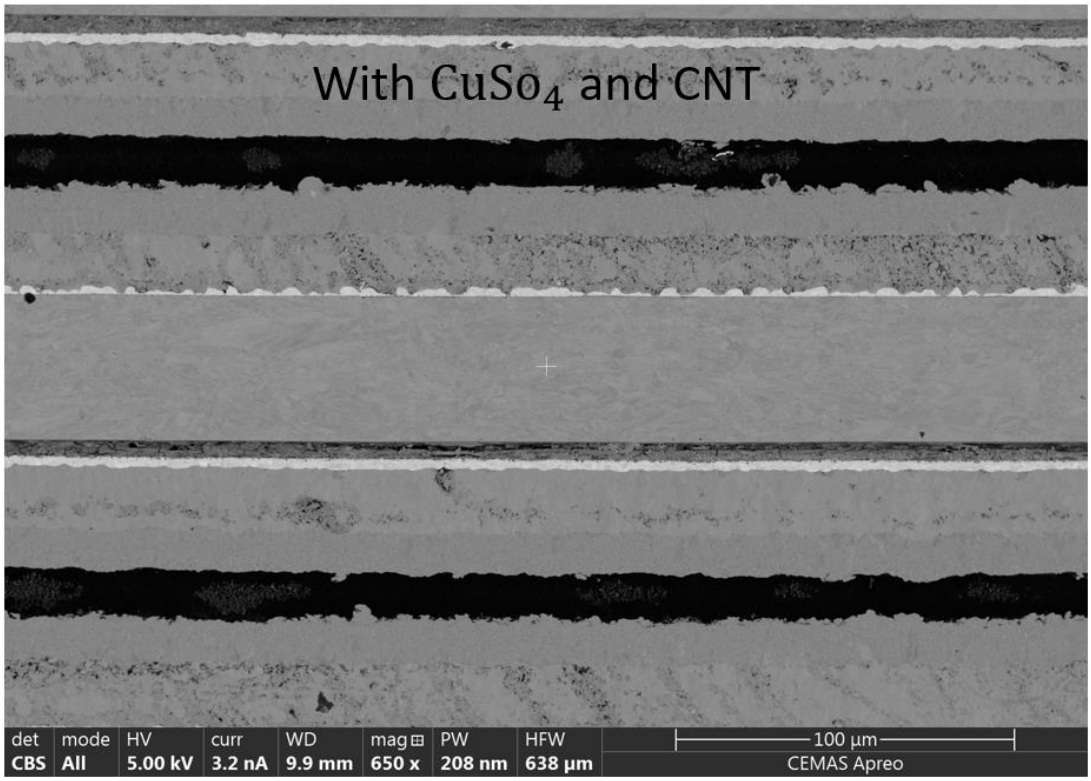

Figure 39: PANI ($CuSO_4$ and CNT) coated REBCO CC tape stack.

The inter-strand electrical contact efficiency, η, measurements of the three types of PANI coated REBCO CCs are shown in Fig. 40. The pristine PANI interlayer produced a η-value of 10000 $\mu\Omega * \mathrm{cm}^2$ at 4.2 K and 13000 $\mu\Omega * \mathrm{cm}^2$ at 77 K. When $CuSO_4$ is added in the electrolyte solution, the resulting Cu^{2+} doped PANI gave a η-value of 6000 $\mu\Omega * \mathrm{cm}^2$ at 4.2 K and 7500 $\mu\Omega * \mathrm{cm}^2$ at 77 K. For the Cu^{2+} doped PANI with CNT inclusion, the measured η-value is 2000 $\mu\Omega * \mathrm{cm}^2$ at 4.2 K and 2300 $\mu\Omega * \mathrm{cm}^2$ at 77 K.

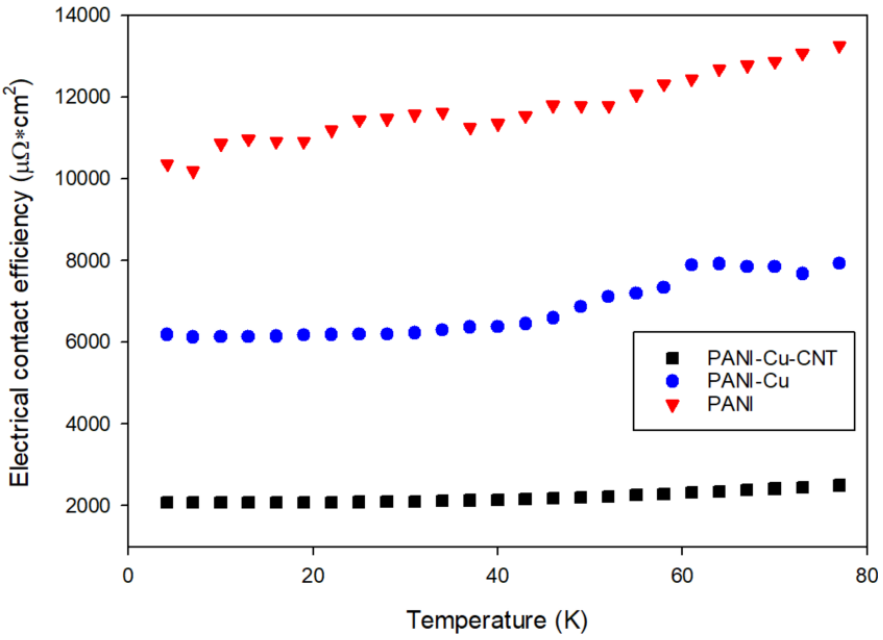

Figure 40: η vs. Temperature for different types of PANI coating

The η-values achieved through the PANI coating process are more controllable than those in which previous cases where η is governed by the surface passivation layer. The conductivity can be adjusted by performing different levels of doping and adding different CNT concentrations. In addition, the η-values will be proportional to the coating thickness which can be easily controlled by changing the processing time.

Chapter 3- FEM simulation of current sharing in REBCO coated conductors

As demonstrated in section 1.9, current sharing in HTS is controlled by inter-strand electrical contact resistance (ICR), inter-strand thermal contact resistance (ITR), and boundary cooling condition. In this chapter, we apply finite element method (FEM) simulation to a single tape and three-tape cables, to study the current sharing behaviors in REBCO coated conductor (CC) tape and cables. Part of this chapter was published in Ref. [117].

For the single tape model, we assumed a total length of 3 cm, with a pre-existing defect in the middle of the tape. Defects of various sizes, ranging from 0.01 mm to 2 mm, in REBCO CCs have been measured and studied [83] [84]. In this study, we assumed the defect had a length of 0.1 mm, across the entire tape width, and with a current ampacity of 0.1 J_c (Fig. 41). The 20 μm of copper stabilizer was considered to be on both the top and bottom wide surfaces (i.e., 40 μm total) and on the side surfaces. More details are presented in Table 4.

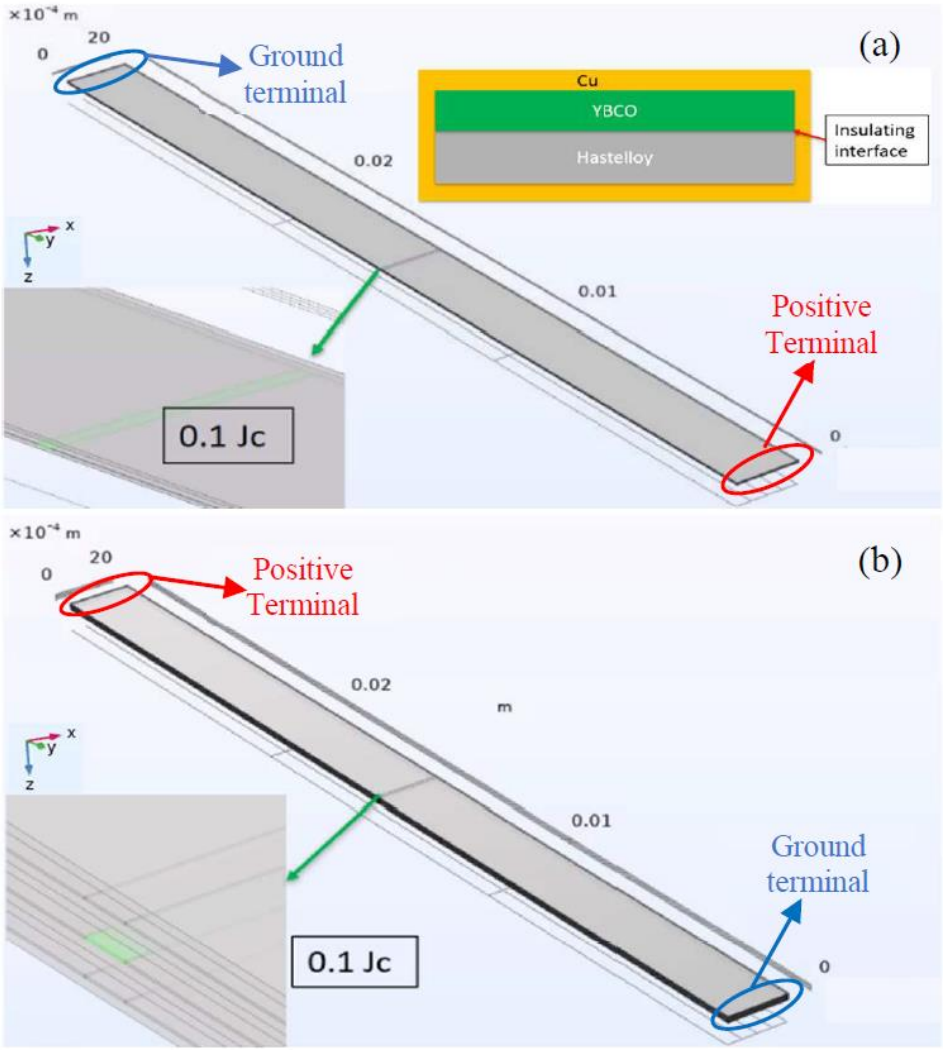

Figure 41: Geometry of half-tape (a) single tape model, and (b) three-tape stack model, with positive and ground injection sites ("terminals") shown. For minimization of computational time, we only modelled the positive-x direction of the tape, assuming the y-z plane to give symmetry.

Table 4: Details about tapes used in both modes.

Width of REBCO	4 mm
Thickness of Cu	20 µm (40 µm total)
Thickness of Hastelloy	50 µm
Thickness of REBCO	5 µm
Length of tape	3 cm
Length of defect	0.1 mm

E_C	100 μm/m
n-value	15
I_C (4.2 K,8 T)	596 A
J_C (4.2 K,8 T)	$2.98*10^{10}$ A/m^2

A three-tape model "cable" was constructed by sandwiching one tape (with one small central defect) between two tapes without defect.

ComsolMultiphysics was used for FEM numerical modelling of the temperature and current distributions in the models. For both the single-tape model and three-tape model, the wide surface of the tape was in the x-y plane, the conductor cross section was in the *x-z* plane, and a mirror symmetry plane was assumed in the *y-z* plane at the half width of the conductor [118] [119], this allowed us to reduce computational time by one half (we calculated current distributions on the positive x-direction of the tape only and assumed symmetry, as shown in Fig. 41). The width, length, and thickness of the conductor were along the *x*-axis, *y*-axis, and *z*-axis, respectively. To capture the properties of the buffer layers, we set the interface between REBCO layer and the Hastelloy to be insulating. Voltages were applied to the ends of the conductors (the conductor "terminals"), as circled in Fig. 41, with one end corresponding to a positive voltage (current injection site) and with the other end of the conductor, to a "ground", and the current flowed from the positive terminal to the ground.

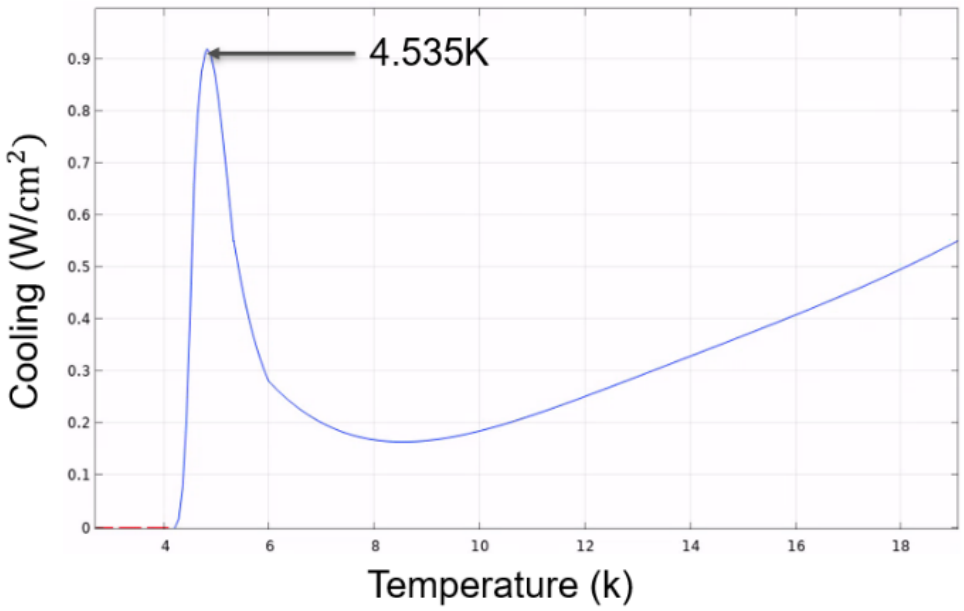

Figure 42: Liquid helium cooling curve [120] [121].

In this work, we assumed that the conductors were immersed in liquid helium, cooling the conductor's surface. In the longitudinal direction, heat transfer was governed by the thermal conductivity of the respective materials, REBCO, Hastelloy and copper, and the terminal surfaces (the cross section of the ends of the conductor) were defined to be electrically conducting but thermally insulating. The thermal conductivity of the Hastelloy, copper, and REBCO were obtained from Ref. [119], [120], and [122], respectively. The electrical conductivity of Hastelloy and copper were obtained from Ref. [119] and [123]. Based on Ref. [120] and [121], we used the cooling curve shown in Fig. 42. Cooling from nucleate boiling peaks at 4.54 K, followed by a transition to film boiling and a significant decrease in cooling power and heat transfer. Different values of the inter-strand electrical contact efficiency, η (η = inter-strand contact resistance ∗ contact area), and inter-strand thermal insulance, ω (ω = inter-strand thermal resistance ∗ contact area), were used as input parameters to define contact properties, ICR and ITR. In addition, the temperature

dependence of J_c was taken into account, this led to an electrical conductivity for the REBCO as defined in Equation 25.

$$J = \sigma E;\ \frac{E}{E_c} = \left(\frac{J}{J_c}\right)^n;\ J_c = J_{c0}\left(1 - \frac{T}{T_c}\right)$$

$$\sigma = J_{c0}\left(1 - \frac{T}{T_c}\right)\left(\frac{1}{E_c}\right)^{\frac{1}{n}} E^{(\frac{1}{n}-1)} \qquad Eq.25$$

3.1 Current sharing limit in single tape model

In a real physical scenario, a power supply can operate in either voltage control mode or current control mode. However, in either mode, in reality the power supply accomplishes this task by manipulating the voltage drop (potential) across the sample. Thus, to model a scenario similar to the physical case where a power supply attempts to maintain a fixed current through a conductor (a power supply in current control mode), we defined the cross-sectional surface of the entire tape end (including YBCO, buffer layers, substrate, and stabilizer), circled in Fig. 41 (a), to be an equipotential surface. There was one such equipotential surface at the positive terminal, and another at the ground, and the voltage drop across the tape (positive terminal to ground) was set by the (FEM) program to result in a given current (and thus current density) through the tape. In this manner we ran simulations at a series of defined current densities ranging from 0.5 J_c to 0.96 J_c, with the simulation showing the resulting distribution of current density and temperature throughout the sample (tape) at each value of current density. Our goal was to determine, for a given set of electrical and thermal conditions, the current density for thermal runaway.

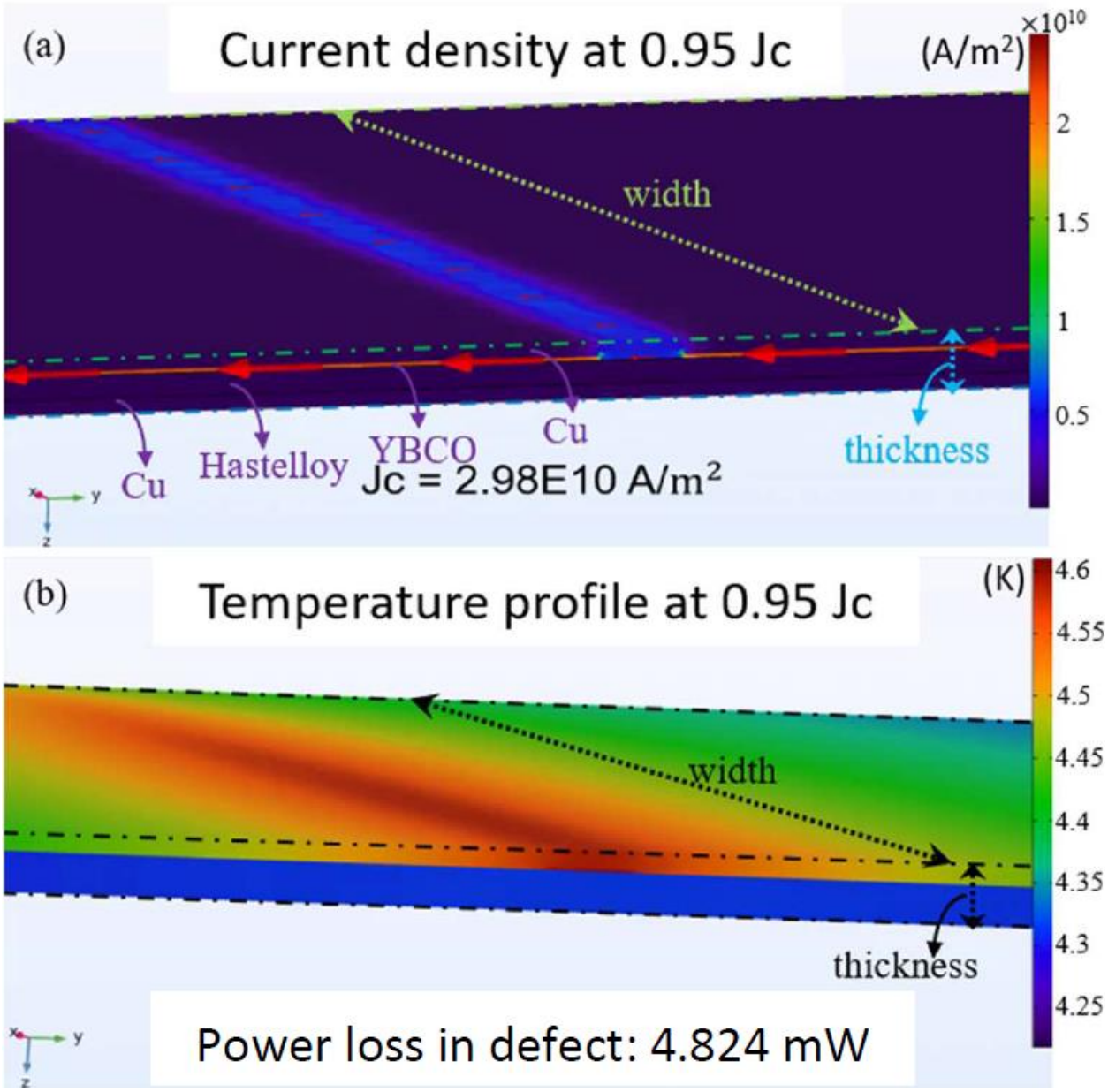

Figure 43: Single tape model (a) current profile (red arrows indicate the direction of current flow and relative magnitude of current density). Note that we are looking at the y-z plane where the symmetry plane is inserted and the top surface x-y plane. The tape length along y, width along x, and thickness along z. The defect is in the REBCO layer at a particular value of y. (b) temperature profile.

As noted above, the defect (0.1 mm long) had a critical current density of 10% of J_c, and the tape was immersed in liquid helium. The current density limit was 0.95 J_c, i.e., above 0.95 J_c, the tape exhibited thermal runaway. The current distribution and temperature profile of the single

tape model at J = 0.95 J_c are presented in Fig. 43. As indicated by the red arrows in Fig. 43 (a), current was carried by the REBCO layer before and after the defect (i.e., at value along the y-axis closer to the positive or negative end of the tape), while this current redistributed into the top copper stabilizer at y-positions near the defect region. The highest temperature of the tape was found near the defect, and was 4.6 K; near here the current was redistributed into the copper stabilizer. The power dissipated in the defect due to resistive heating was 4.824 mW. We see that the tape could carry 95% of the nominal J_c with minimal ΔT. Near the defect, the current was shared into the matrix, and some local temperature rise was seen. Nevertheless, even with a spatially small defect carrying only 10% of the nominal J_c, the excellent liquid He cooling enabled minimal temperature rise.

3.2 Current sharing limit in cable model (bad contact, single central tape excitation)

First, we considered the case of bad inter-strand contact. Therefore, η was set at 5400 $\mu\Omega * \mathrm{cm}^2$ [88]. We assumed that the thickness of the native oxide on the copper surface is 4 nm, and calculated a resistivity based on η. Then we calculated the ratio between the η-based resistivity and the resistivity of copper, and used the same ratio to conclude that the inter-strand thermal insulance, ω (ω = ITR $*$ contact area), was 5.54 $\mathrm{K} * \mathrm{m}^2/\mathrm{W}$.

Some models have demonstrated that at steady-state condition, current sharing was determined by the termination resistances [124] [125] [126] [127]. Therefore, to better capture the essence of current sharing around a defect, we ran a simulation where we only "applied current" to the central tape (the one with the defect); more precisely we defined the positive terminal equipotential to be only on the cross section of the end of the central tape (the one

with the defect), and the ground terminal was defined to be only at the other end of the central tape , including REBCO layer, buffer, substrate, and stabilizer. The central tape was in electrical and thermal contact (with defined interfacial values) with the upper and lower tapes via the tape surfaces, but not the tape ends.

The voltage drop across the cable was chosen to drive set currents of up to 0.6 I_c (single tape I_c) to flow in the cable. The current redistributed as it neared the cable's middle point between the terminations (near the defect); here the REBCO layer of the central tape only carried 0.17 I_c. The maximum temperature of the defect was 6 K (Fig. 44 (b)). The current redistributed around the defect mainly into the copper stabilizer. As demonstrated in Fig. 44 (c), due to the high ICR and ITR, the REBCO layers in the lower and upper tapes carried only a small fraction of the redistributed current, $5*10^{-6}$ I_c ($1.5*10^5$ A/m^2) in each tape, the majority of the current being shared into the Cu stabilizer. As the current bypassed the defect, the redistributed current in the Cu stabilizer and the REBCO layers of the top and bottom tapes went back into the REBCO layer of the central tape and traveled to the ground terminal via the least resistive path.

In this case, a high inter-strand electrical contact resistance (ICR) and inter-strand thermal contact resistance (ITR) kept the level of current sharing small. In comparison with the single tape model, section 3.1, as a result of reduced cooling and minimal current sharing, the maximum allowed power dissipated in the defect (2.601 mW) of the 3-tape cable is smaller than that in the single tape.

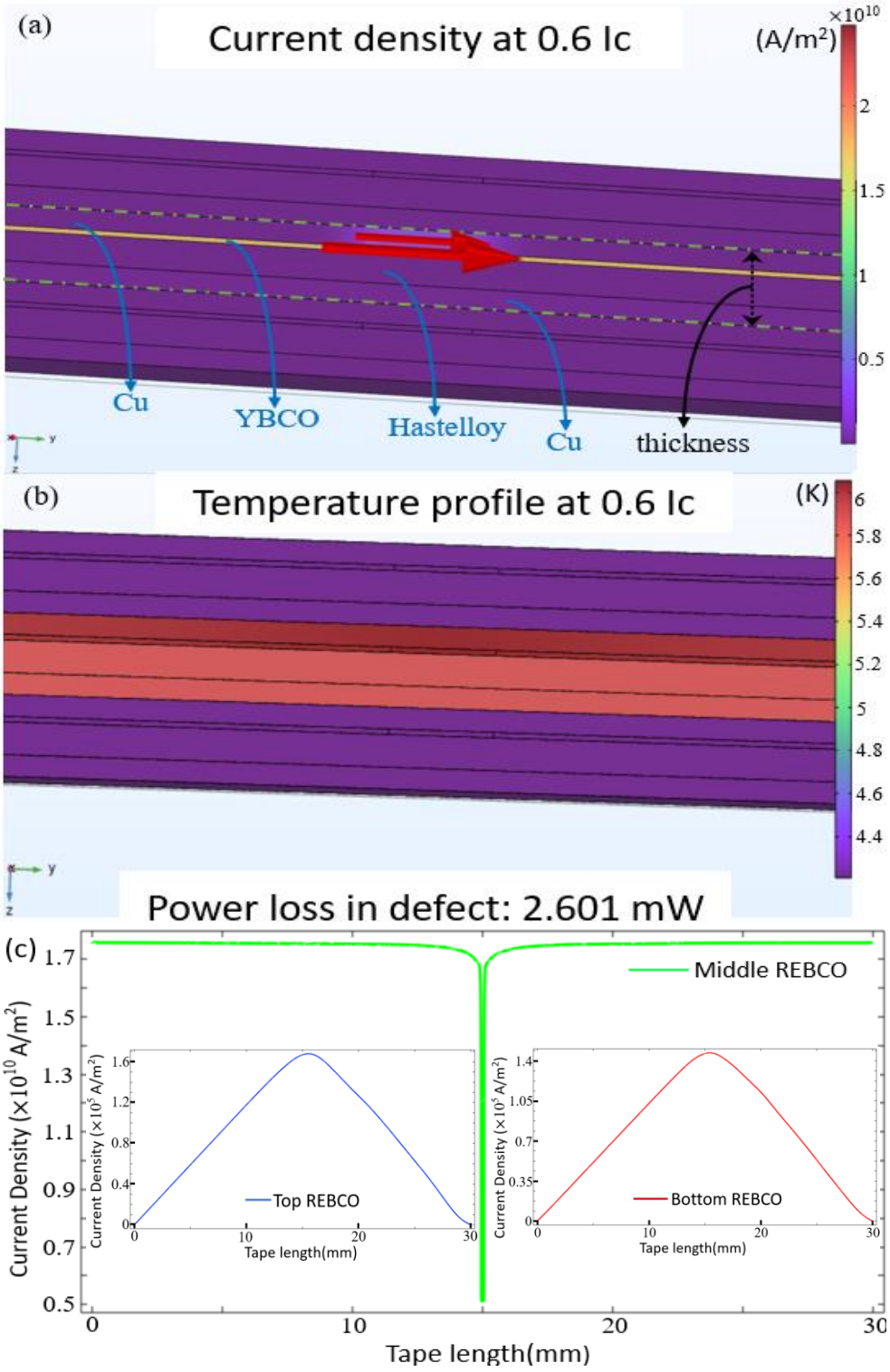

*Figure 44: Three-tape stack model and we are looking at yz plane (η = 5400 μΩ*cm², ω = 5.54 K*m²/W) (the middle tape is marked by the two green dashed line); (a) current profile (red arrows indicate the direction of current flow and relative magnitude of current density), (b) temperature profile, (c) current distribution in the REBCO layers along tape length.*

3.3 Current sharing limit in cable model (good contact, single central tape excitation)

Next, we considered the case of good inter-strand contact. We assumed a η of 10 $\mu\Omega * \mathrm{cm}^2$ [97] and used the same method as described in section 3.2 to calculate the inter-strand thermal insulance, ω, which turned out to be 0.01 K*m^2/W. As shown in Fig. 45 (b), compared to section 3.2, given the same current input (0.6 I_c of one tape), due to reduced ICR and ITR, the maximum temperature at the defect spot decreased from 6 K to 4.8 K, and the power dissipated in the defect (2.564 mW) also decreased. Based on the current profile, Fig. 45 (a) and (c), a current of 0.004 I_c (J_c = 1.2*10^8 A/m^2) became redistributed to each of the REBCO layer of the upper and lower tapes. Following the defect, the redistributed current went back to the REBCO layer of the central tape. This is because only the cross-section surface of the end of the middle tape was set to be the equipotential ground terminal and the REBCO layer was the least resistive path for current transferring through the tape. Current sharing to the adjacent REBCO CC tapes increased about 800 times due to the reduction of ICR and ITR. In addition, 0.6 I_c is apparently not the limiting current in this three-tape cable, given the lower temperature and reduced power loss in the defect.

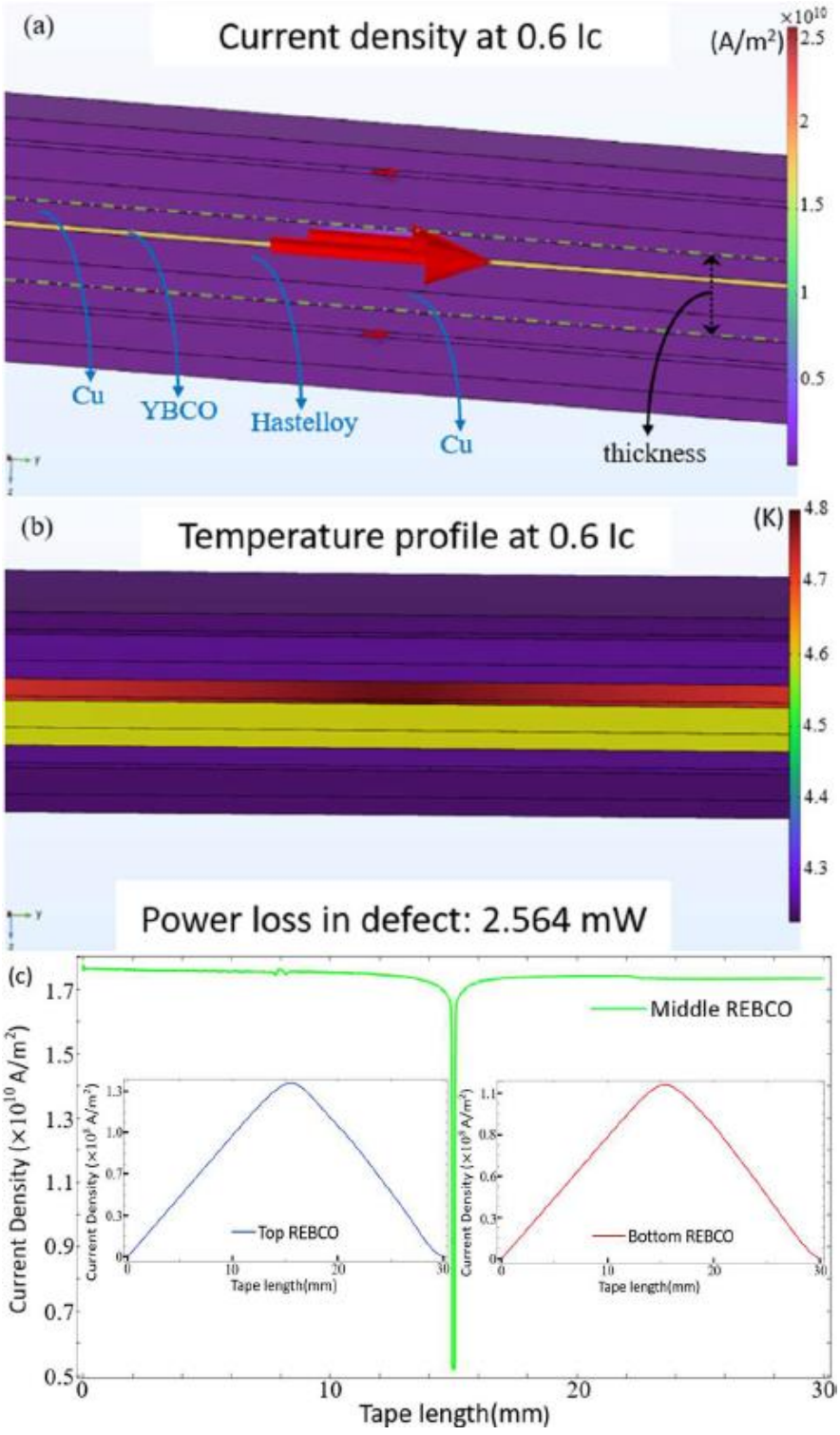

*Figure 45: Three-tape stack model and we are looking at yz plane (η = 10 μΩ*cm², ω = 0.01 K*m²/W) the middle tape is marked by the two green dashed line); (a) current profile (red arrows indicate the direction of current flow and relative magnitude of current density), (b) temperature profile. (c) current distribution along tape length.*

3.4 Current sharing limit in cable model (thermally insulating inter-strand contact)

To better demonstrate the contribution of ITR and cooling to the current sharing limit in REBCO cable, we set the inter-strand thermal contact to be insulating, and performed two addition simulations with two different values of η for good electrical contact, 10 $\mu\Omega * \mathrm{cm}^2$, and bad electrical contact, 5400 $\mu\Omega * \mathrm{cm}^2$.

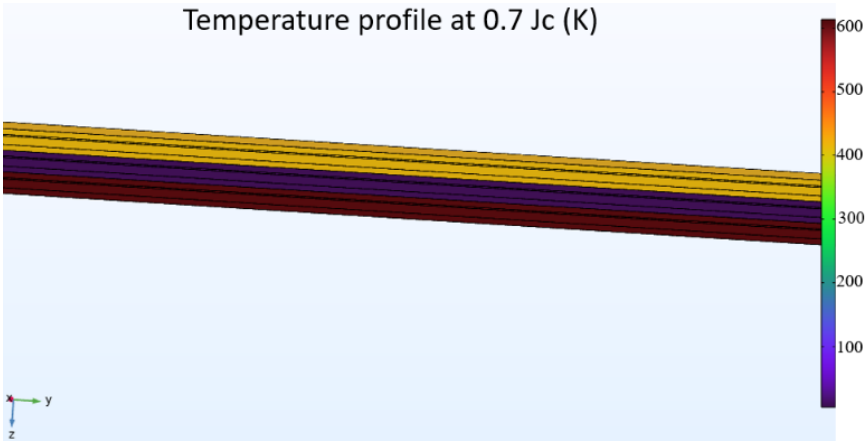

Figure 46: Thermal runaway in REBCO cable with insulating inter-strand thermal contact and an inter-strand electrical contact efficiency of 10 $\mu\Omega * cm^2$

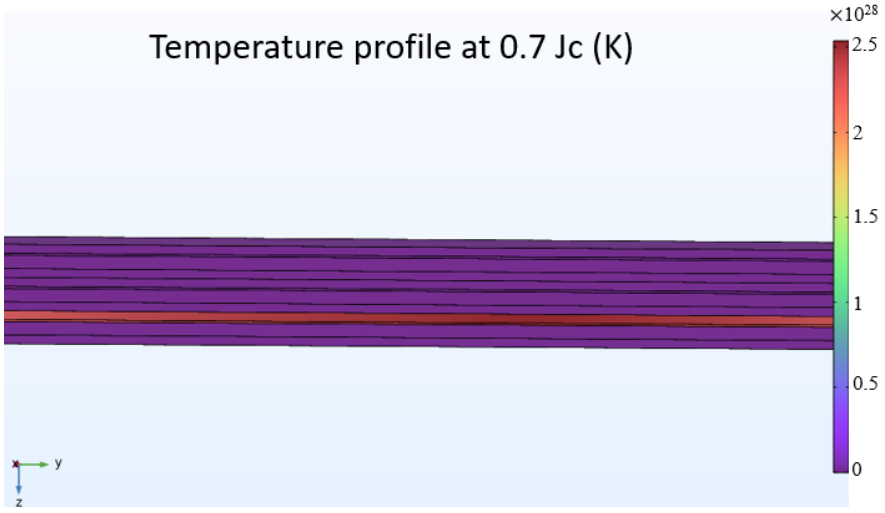

*Figure 47: Thermal runaway in REBCO cable with insulating inter-strand thermal contact and an inter-strand electrical contact efficiency of 5400 μΩ*cm^2*

The results are presented in Fig. 46 and 47. When 0.6 I_c was applied though the cable, thermal runaway happened in both cases.

3.5 Current sharing limit in cable model (metallic contact, defined voltage)

In this simulation, the cross-sectional areas of the ends of the three tapes, at for example the positive terminals, were set to be at one equipotential, and the cross-section of the ends of the three tapes at the ground end of the cable were set to a second equipotential (zero in this case). Again, the whole of the tape (and cable) cross section was set to these equipotentials, including REBCO, buffer layers, substrate, and stabilizer. The voltage drop across the cable was chosen to achieve a set current density of 3.05 I_c. As presented in Fig 48 (a) and (c), the current density in each tape changes along the length of the cable, as we might expect in the presence of a defect. At the positive terminal of the cable, the top and bottom tapes carried 1.05 I_c, with the middle tape carrying 0.95 I_c and currents were carried by the REBCO layer within each tape. Towards the defect, the current in the REBCO layer of the central tape became redistributed away from the defect, into the top and bottom tapes and to a small extent into the copper stabilizer. Halfway between the two terminals (the longitudinal location of the defect), the current density in the REBCO layers of the top and bottom tapes became 1.28 times I_c of the tape, while the current density in the REBCO layer of the central tape was 0.16 I_c. Here I_c always refers to the I_c for an undamaged single tape. The result was consistent with previous studies [84]. Moreover, from the temperature profile, Fig. 48 (b), the temperature at the defective spot was near 4.37 K, which is still below the nucleate boiling peak temperature. Hence, even 3.05 I_c does not appear to be the limiting current. Compared with the single tape model, section 3.1, given two additional neighboring tapes, a defective cable (3-layer tape stack) can carry a current density (3.05 I_c) that

is greater than the nominal critical current density (3 I_c), while a single defective tape can only carry 0.95 I_c. In addition, because the current in the central defective tape can be shared into its neighboring tapes, the power dissipated in the defect due to joule heating is reduced.

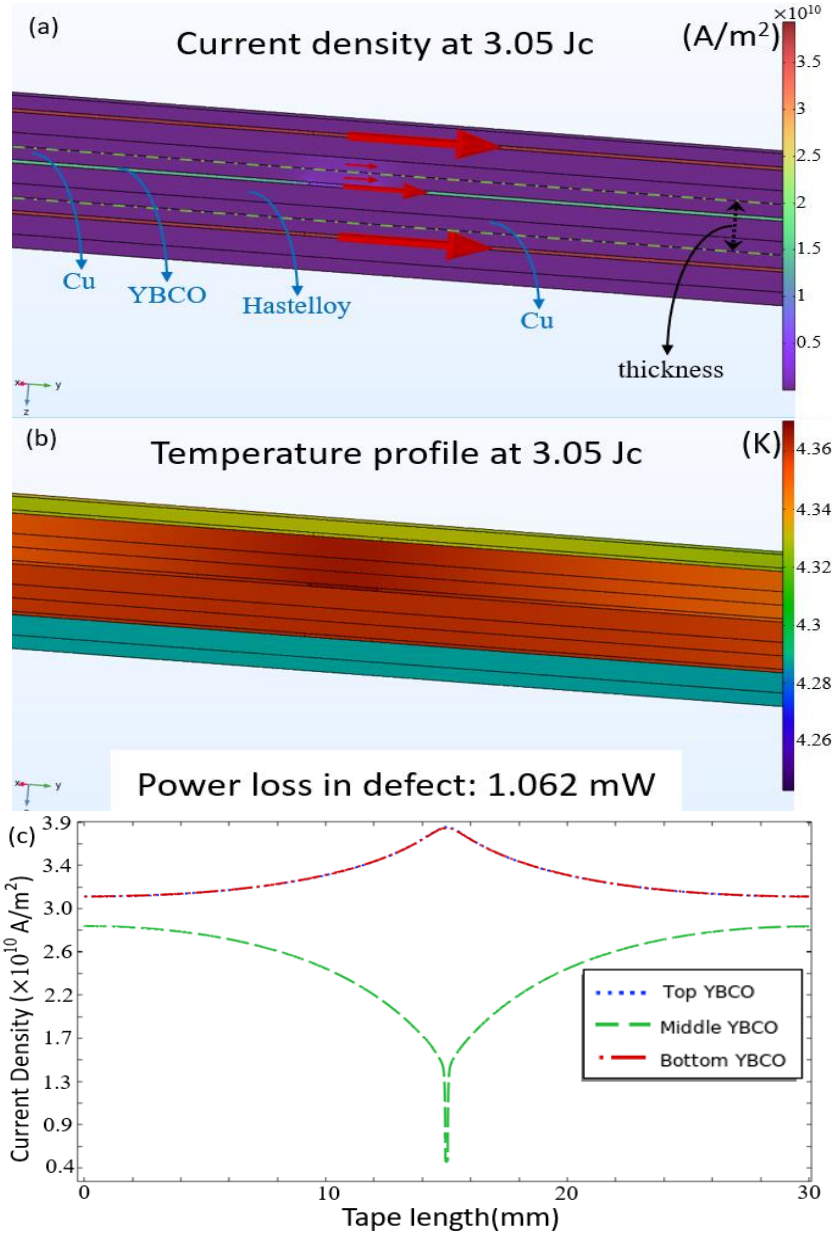

Figure 48: Three-tape stack model (no contact resistance) and we are looking at y-z plane (the middle tape is marked by the two green dashed line); (a) current profile (red arrows indicate the direction of current flow and relative magnitude of current density), (b) temperature profile, (c) current distribution in the REBCO layers along tape length.

We kept on increasing the applied current through the cable to investigate the current sharing limit in this scenario. As shown in Fig. 49, the maximum achievable current is 4.0 times I_C of a single tape, which gives a current sharing metric of 1.33.

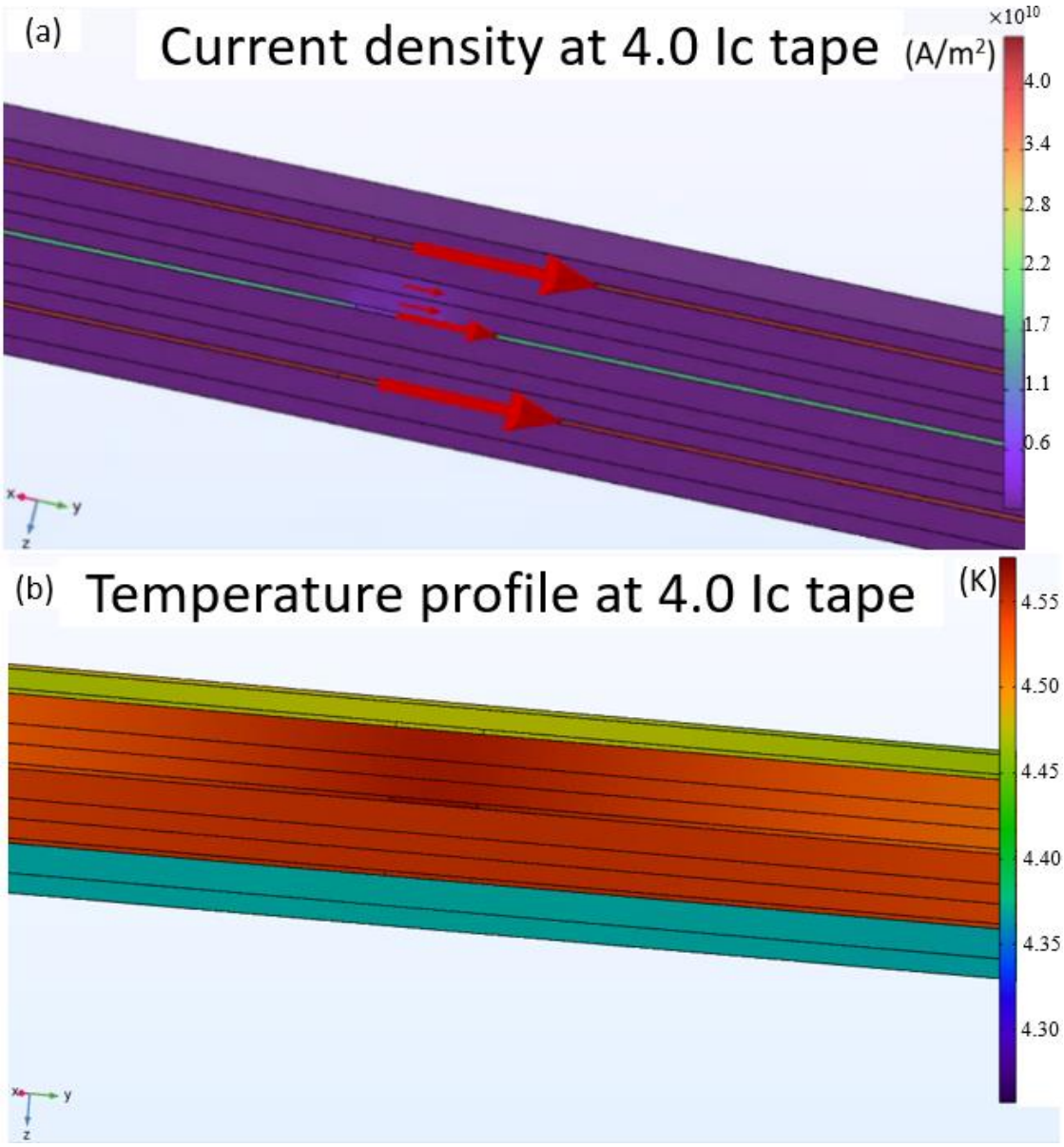

Figure 49: Current sharing limit in REBCO cable given metallic inter-strand contact (a) Current distribution in the cable, (b) Temperature profile of the cable.

3.6 Current sharing limit in cable model (good contact, defined voltage)

Section 3.5 describes the most ideal case where the inter-strand contact is purely metallic. We now want to consider some real cases. First, we considered the case of good inter-strand contact. Hence, in this simulation the η and ω were set to be 10 $\mu\Omega * \mathrm{cm}^2$ and 0.01 $\mathrm{K} * \frac{\mathrm{m}^2}{\mathrm{W}}$, respectively. We found that the maximum achievable current in this cable is 3.15 I_c of a single tape, which led to a current sharing metric of 1.05. As shown in Fig.50, the current distributions at the defect were 1.19 I_c, 0.18 I_c, and 1.19 I_c in the top, central, and bottom REBCO layers, respectively. The copper stabilizer in the middle defective tape carried the remaining 0.59 I_c. The maximum temperature at the defect was 5.2 K. Because the current terminals were set to be equipotential surfaces, current transfer actually took place at the terminals where the current distributions to the top, central, and bottom REBCO layers were 1.19 I_c, 0.77 I_c, and 1.19 I_c.

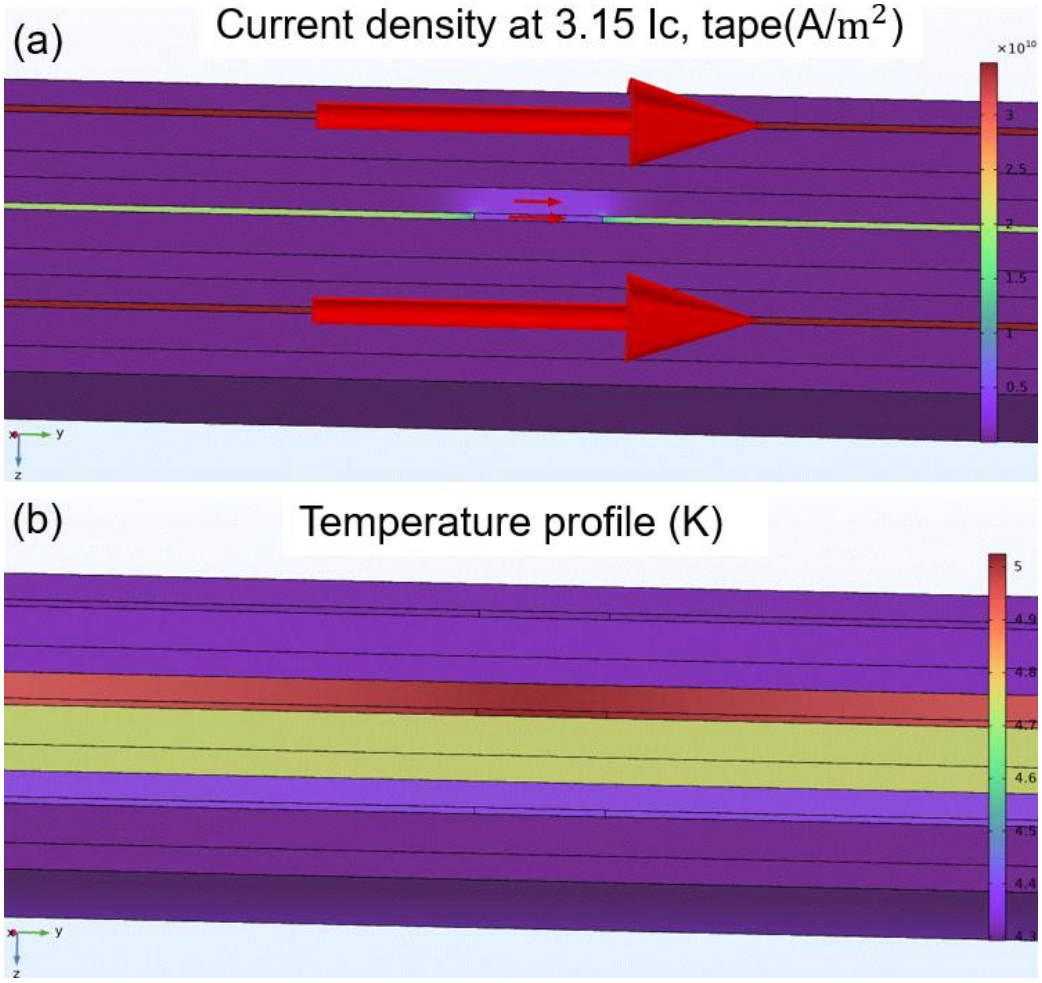

Figure 50: Equilibrium state current sharing limit in REBCO cable given good inter-strand contact (a) Current distribution in the cable, (b) Temperature profile of the cable.

3.7 Current sharing limit in cable model (bad contact, defined voltage)

Then we investigated the current sharing limit for bad contact scenario, where η and ω were set to be 5400 $\mu\Omega * \mathrm{cm}^2$ and 5.54 $\mathrm{K} * \mathrm{m}^2/\mathrm{W}$ respectively. By setting the current terminals to be equipotential surfaces, the maximum achievable current though this cable was 2.70 I_c, giving a current sharing metric of 0.9. Compared to the cases discussed in section 3.5 and 3.6, the reduced current sharing metric is caused by the increased inter-strand contact resistance. Fig. 51 shows the current distribution and temperature profile in the cable. At the defective spot, the maximum

temperature reached 5.1 K. Also, the current distribution in the top, central, and bottom REBCO layer was 1.18 I_c, 0.17 I_c, and 1.18 I_c respectively, and the copper stabilizer in the central defective tape carried 0.17 when the applied current reached the defect. In this case, current transfer happened at the current terminal as well, and the current distribution at the current terminal was 1.18 I_c, 0.34 I_c, and 1.18 I_c in the top, central, and bottom REBCO layers.

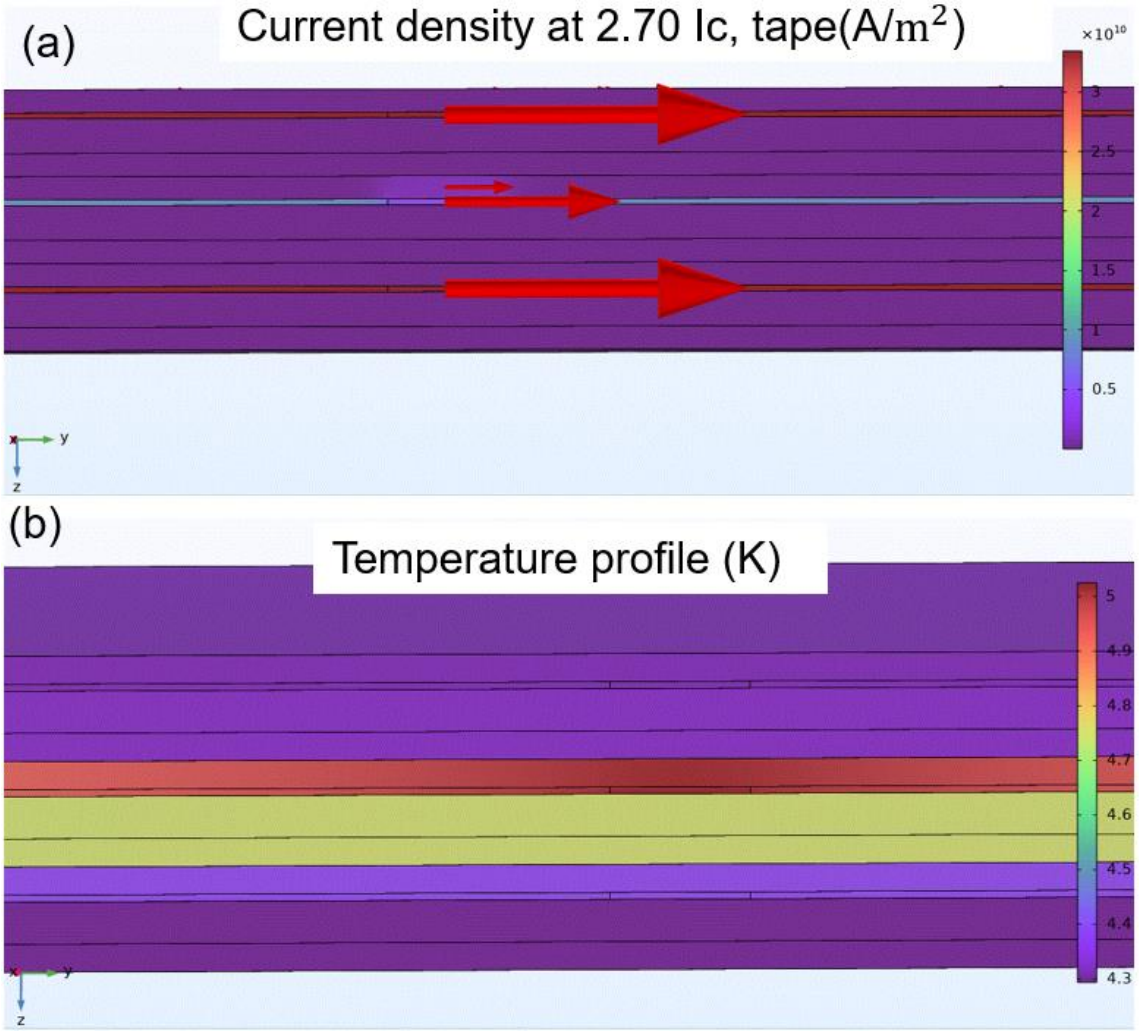

Figure 51: Equilibrium state current sharing limit in REBCO cable given bad inter-strand contact (a) Current distribution in the cable, (b) Temperature profile of the cable.

The cases discussed in section 3.6 and 3.7 can be regarded as equilibrium states. The defect is pre-existing in the cable, and current is gradually applied to the cable until it reaches its maximum value.

3.8 Current sharing limit in cable model (good contact, defined current)

We are also interested in the transient current sharing limit in the REBCO cable when the defect is created during operation. By setting the inter-strand electrical contact efficiency, η, to be 10 $\mu\Omega * \mathrm{cm}^2$ and the inter-strand thermal insulance, ω, to be 0.01 $\mathrm{K} * \mathrm{m}^2/\mathrm{W}$, we found that, given good inter-strand contact, the current sharing metric is 0.9. As shown in Fig. 52, when the same amount of current was applied to each individual tape, the maximum current that could pass this defective cable with good inter-strand contact was 0.9 I_c in each tape (3*0.9=2.7I_c in the cable). At the current terminal a current of 0.9 I_c was applied to each tape. At the defective position, current transfer took place, leading to a current distribution in the top, central, and bottom tapes of 0.91 I_c, 0.18 I_c, and 0.9 I_c respectively. The Cu stabilizer of the central tape carried 0.71 I_c at the defective position. The hotspot reached a temperature of 5.8 K.

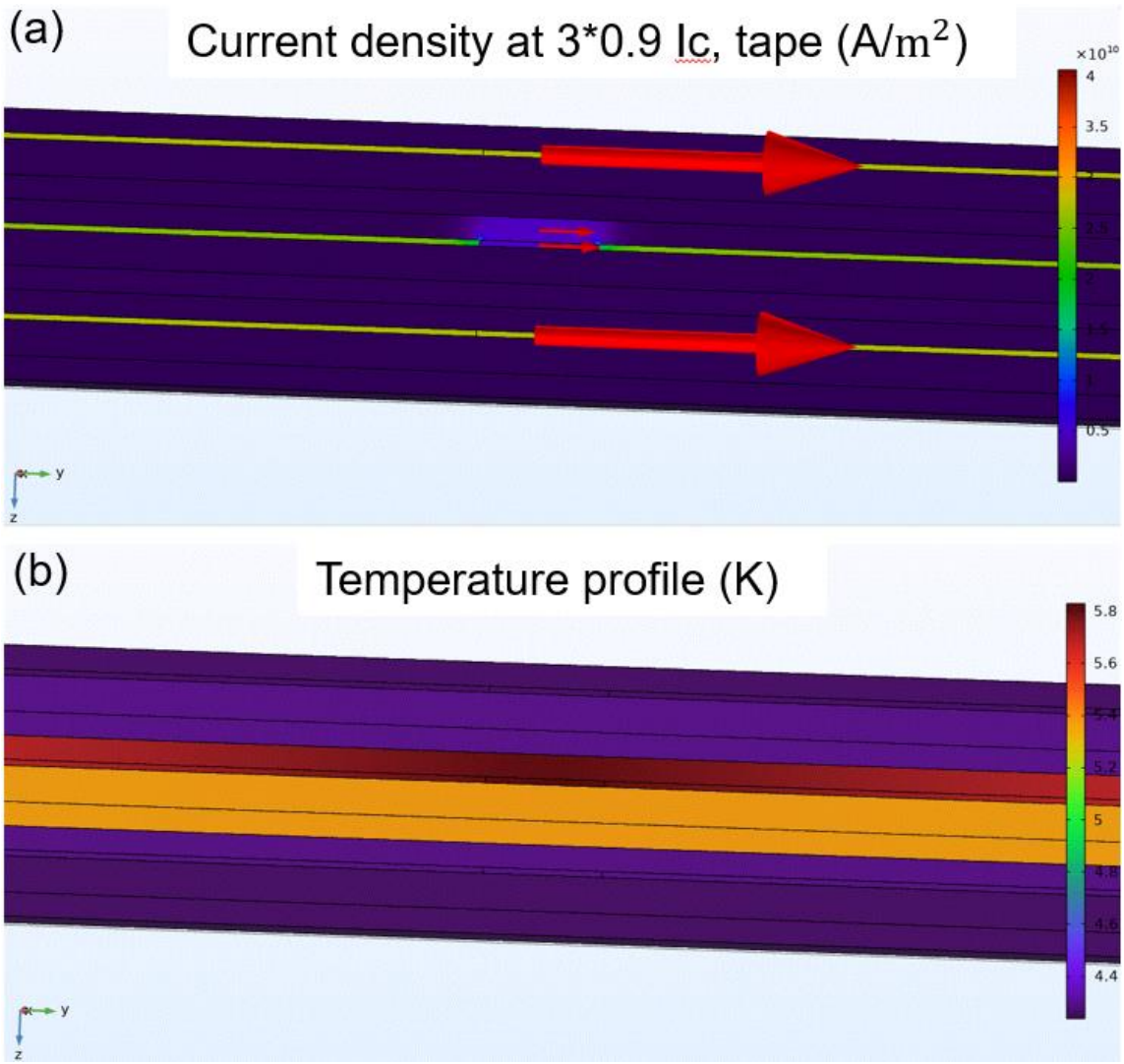

Figure 52: Transient state current sharing limit in REBCO cable given good inter-strand contact (a) Current distribution in the cable, (b) Temperature profile of the cable.

3.9 Current sharing limit in cable model (bad contact, defined current)

We then instigated the transient state current sharing limit in the defective cable with bad inter-strand contact. As shown in Fig. 53, the maximum current that could be applied from the terminal to each tape of the cable is 0.55 I_c, giving a current sharing metric of 0.55. At the defect, the hot spot temperature reached 5.9 K, and current redistributed to 0.55 I_c, 0.17 I_c, and 0.55 I_c in the top, middle, and bottom tape respectively.

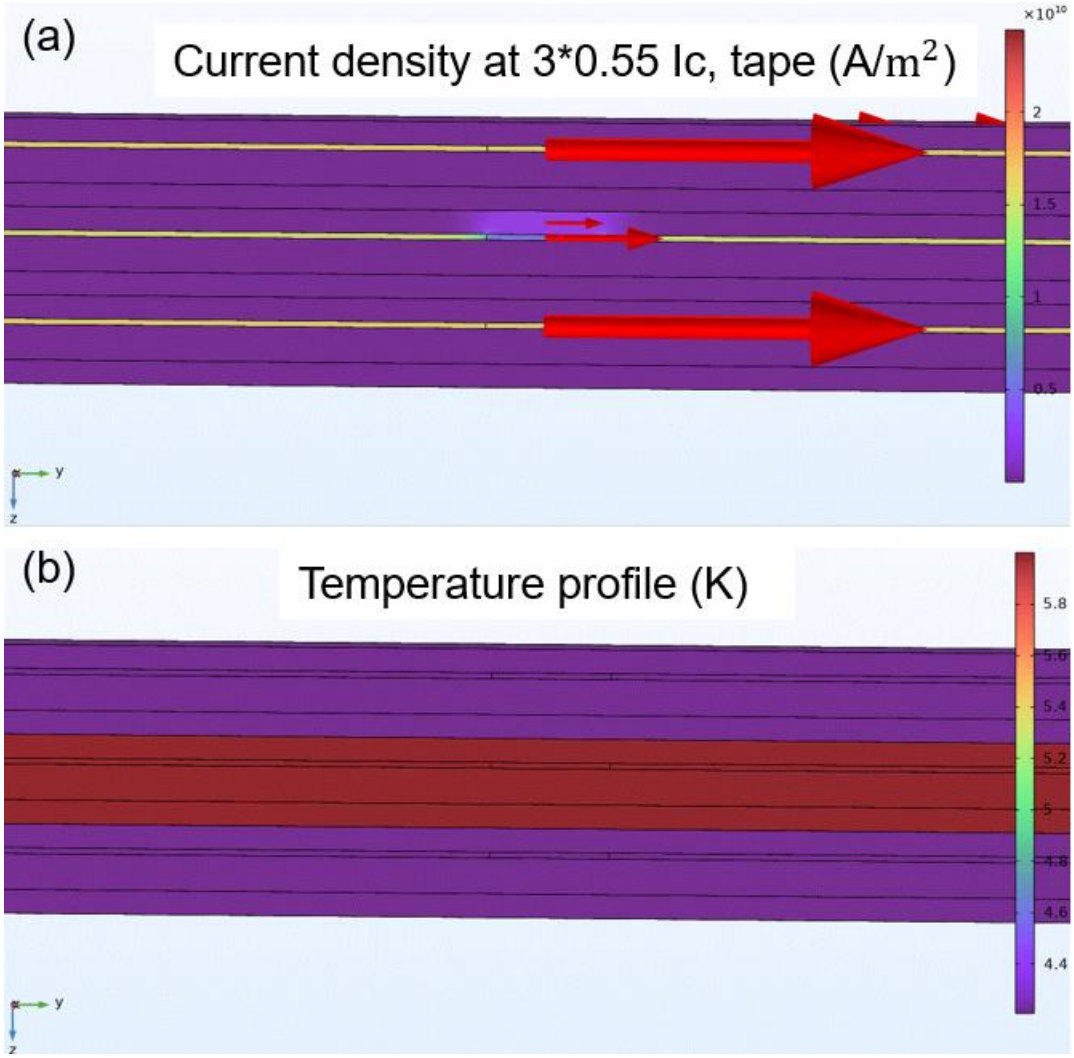

Figure 53:Transient state current sharing limit in REBCO cable given bad inter-strand contact (a) Current distribution in the cable, (b) Temperature profile of the cable.

Comparing the cases described in section 3.8 and 3.9 to their counterparts in section 3.6 and 3.7, we found the transient state current sharing limit/metric for a REBCO cable given certain inter-strand contact properties and cooling condition is much lower than the equilibrium state current sharing limit/metric for the same cable with identical cooling condition. Hence, we conclude that the lower limit needs to be considered during magnet design.

Chapter 4- Magnetization, flux creep, and AC loss measurement for REBCO tapes and cables

HTS are being considered promising materials for manufacturing high field dipole, quadrupole, and insert magnets. The field quality of a magnet can be significantly affected by both geometric (or winding) error field and magnetization error field. The geometric error field is a fixed and predictable error that can be easily corrected. However, the error field from conductor magnetization is more difficult to remove. There are two contributions to magnetization: eddy currents, whether in the sheath itself, or as coupling currents within or between strands [128] [129], and the magnetization from hysteretic (or "persistent currents") [128] [130]. This magnetization is proportional to the critical current density and filament diameter of the superconductor [45]. Compared with low temperature superconductors (LTS) [46] [47], HTSs have much larger filament diameters [48] [49] [50], hence magnetizations, than LTS. In addition, the magnetization in a HTS also suffers from flux creep due to week flux pinning. Therefore, it is necessary to quantify the magnetization and its creep component and to control the error field.

4.1 Magnetization and flux creep in STAR cables

Symmetric Tape Round (STAR) REBCO wire fabricated with REBCO CCs by advanced MOCVD is a promising candidate for high field applications because of its outstanding current carrying ability and current retention under bending radii as small as 15 mm [131] [132] [133]. We received a STAR cable from the University of Houston and AMPeers LLC., and took a segment of the cable for magnetization and flux creep measurements. Table 5 tabulated detailed specifications of this STAR sample.

Table 5: Specifications of STAR sample

Cable properties	
Wire OD (mm)	2.25
Cu core OD (mm)	0.81
No. tapes	11
Tape width (mm)	1.4 (x1), 1.95 (x2), 2.55 (x8)
Cu plating thickness (µm)	25
Substrate thickness (µm)	20
Ic at 77 K (A)	725
Sample properties	
Sample length (cm)	2.78
$V_{cable}\ (cm^3)$	0.1105
$V_{tape}\ (cm^3)$	0.0564

The magnetization and flux creep of the STAR sample were measured by a 12-T hall probe system [51] [53] [134] [135], Fig. 54. The conduction cooled solenoid can generate a magnetic field from -12 T to 12 T. The system includes is a varitemp dewar with its tail inserted into the bore of solenoid. The hall probe, along with the sample to be measured are inserted into the dewar. In our STAR cable measurements, the dewar was filled with liquid He and all measurements were conducted at 4.2K.

Figure 54: 12 T hall probe system

Because there was a small amount of ferromagnetic materials in the setup, several M-μ_0H were measured without the presence of the sample to acquire the background signal as a function of applied field and applied field history.

We first measured a 99.5% pure Ni standard with dimensions of 2 mm * 10.5 mm * 28.8 mm. The theoretical saturation magnetic moment of Ni is 0.64 T, equivalent to 509.5 emu/cm^3. Given the dimension of the Ni standard, we calculated the theoretical magnetization of the Ni strander. By comparing the theoretical value to the measured field difference between the sample and no sample cases, a calibration constant was determined and then used to convert the measured *B* to *m,* as shown in Fig. 55 [53]. This Ni-calibration constant was applied to the later data analysis for the STAR cable.

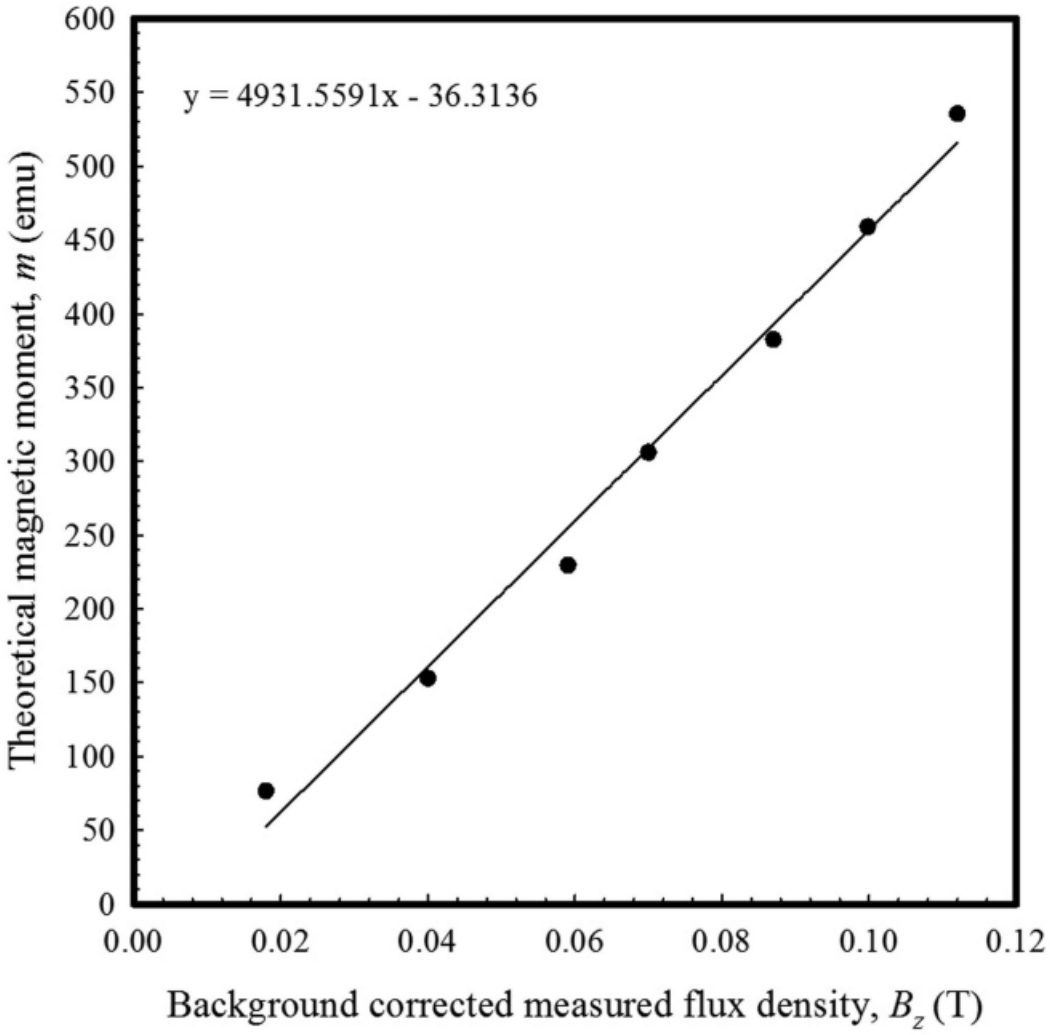

Figure 55: Plot of expected nickel magnetic moment vs measured background corrected magnetic flux density. The slope of the fit is the calibration constant that converts a measured background corrected magnetization to a magnetic moment.

In addition, because the active area of the Hall sensor is smaller than the size of our sample. A shape sensitivity factor was needed. The Meissner effect in a superconductor leads to complete magnetic flux exclusion from the inside of a superconductor as long as the externally applied field is smaller than its flux penetration field. Therefore, theoretically the susceptibility of a superconductor is -1, giving $M = -H_{applied}$. In real cases, geometrically dependent demagnetization needs to be taken into account. For a round cylinder, for example the STAR cable,

the demagnetizing factor is 0.5, leading to a relation of $M = -2H_{applied}$. Hence, by correcting the slope of the measured data at the initial ramp up to -2, we determined the shape sensitivity factor. With both the Ni-calibration factor and the shape sensitivity factor, we processed the measured data.

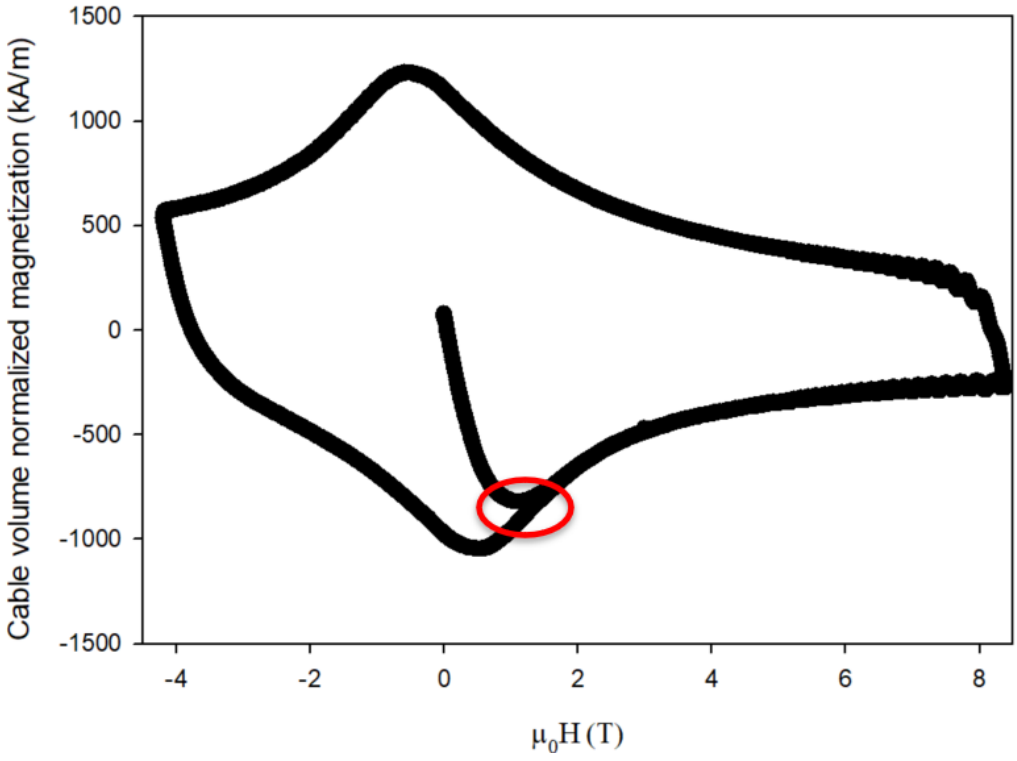

Figure 56: Cable volume normalized M-μ0H of STAR sample

Fig. 56 shows the M-μ_0H curve of this STAR sample measured from -4 T to 8 T. The magnetization of the sample was normalized to the total cable volume. The maximum cable volume normalized magnetization of the STAR cable was 1140 kA/m. The flux penetration field was around 1.2 T at which field the cable volume normalized magnetization was 820 kA/m.

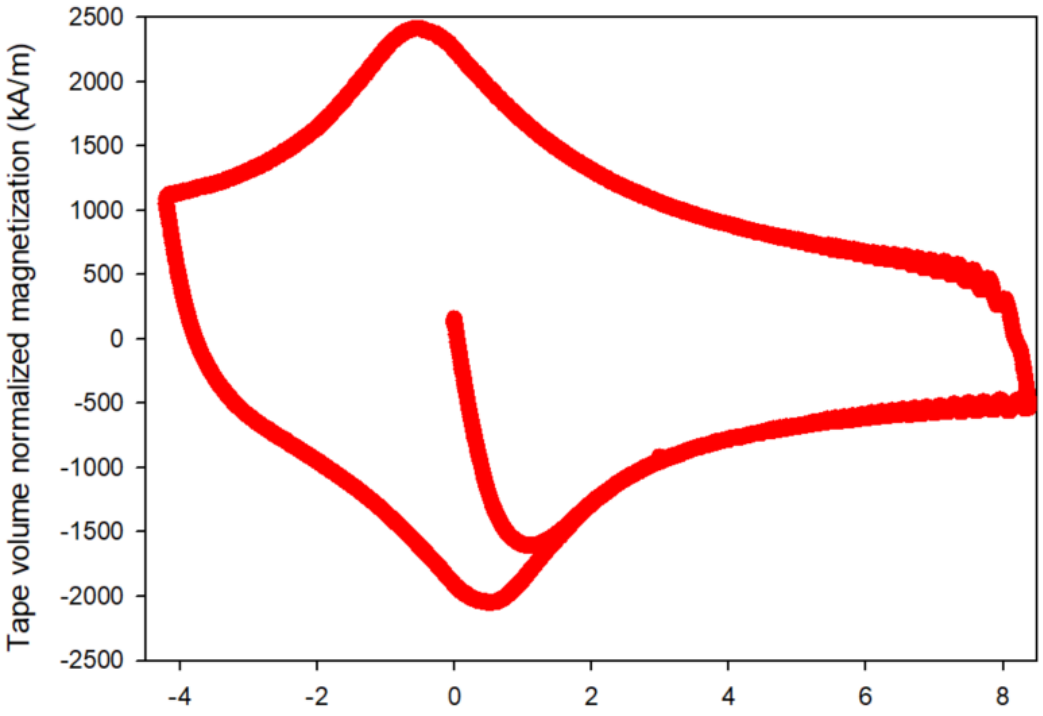

Figure 57: Tape volume normalized M-μ0H of STAR sample

We were also interested in the magnetization of the constituent tapes. Therefore, after completion of the measurements, we dissembled the cable, measured the volume of the tape, and calculated the tape volume normalized magnetization. As shown in Fig. 57, the maximum tape volume normalized magnetization based on our direct measurement was 2233 kA/m. We want to verify our measurement with theoretical calculation. The magnetization of a tape, M_{tape}, with helical structure can be calculated based on Equation 26, where J_c is the critical current density of the superconductor tape, a is the half width of the tape, and $\frac{2}{\pi}$ is a geometric factor to take into account the helical structure [52] [136]. Theoretical calculation gave us the tape volume normalized magnetization of 2098 kA/m, which was in reasonably good agreement with our direct measurement. 2233 kA/m.

$$M_{tape} = \frac{2}{\pi} * \frac{J_c * a}{2} = \frac{2}{\pi} * \frac{J_c * w}{4} \qquad Eq.26$$

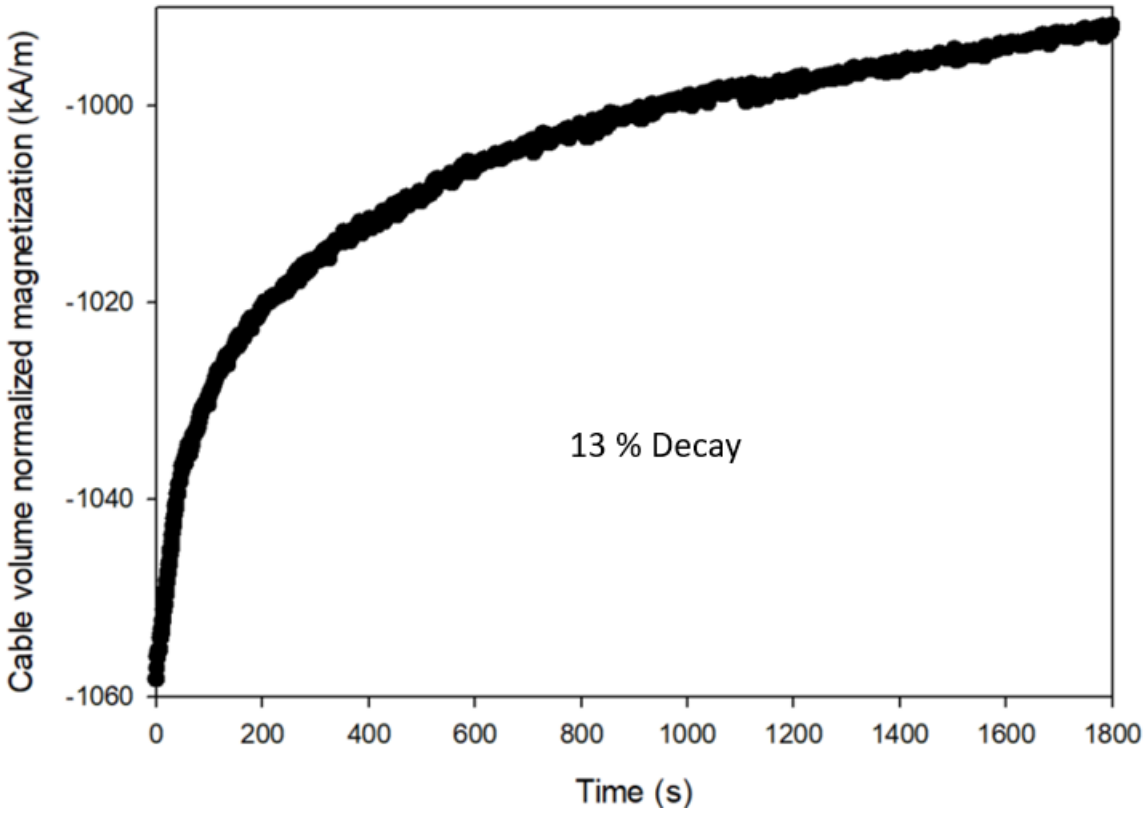

Figure 58: Magnetization decay for 1800 s for fully flux penetrated STAT cable.

Next, we investigated the flux creep behavior of the STAR cable. We applied the field sequence as 0→4 T→-2 T→1 T to make sure the sample reached the fully flux penetrated state, and then held the sample under 1 T for 1800 seconds to observe the flux creep. As shown in Fig. 58, the initial magnetization at the fully flux penetrated state was around 1060 kA/m. After 1800 s, the magnetization decayed by 13% to 920 kA/m.

As introduced in section 1.6, flux creep in a superconductor is proportional to the initial magnetization, according to Equation 20, $M(t) = M_0[1 - \frac{k_B T}{U_0} ln(\frac{t}{t_0})]$. Hence, reducing the initial magnetization is a viable method to reduce flux creep. The initial magnetization can be controlled

by applying pre-injection field cycles [134]. Hence, in the following set tests, we applied the field sequence 0→4 T→x→1 T, where the values of x were 0 T, 0.2 T, 0.4 T, and 0.8 T. The M-μ_0H curves with different hold fields, x, are displayed in Fig. 59. Then the sample was held for 1800 s under 1 T. The flux creep with different initial magnetizations due to different hold fields are displayed in Fig. 60.

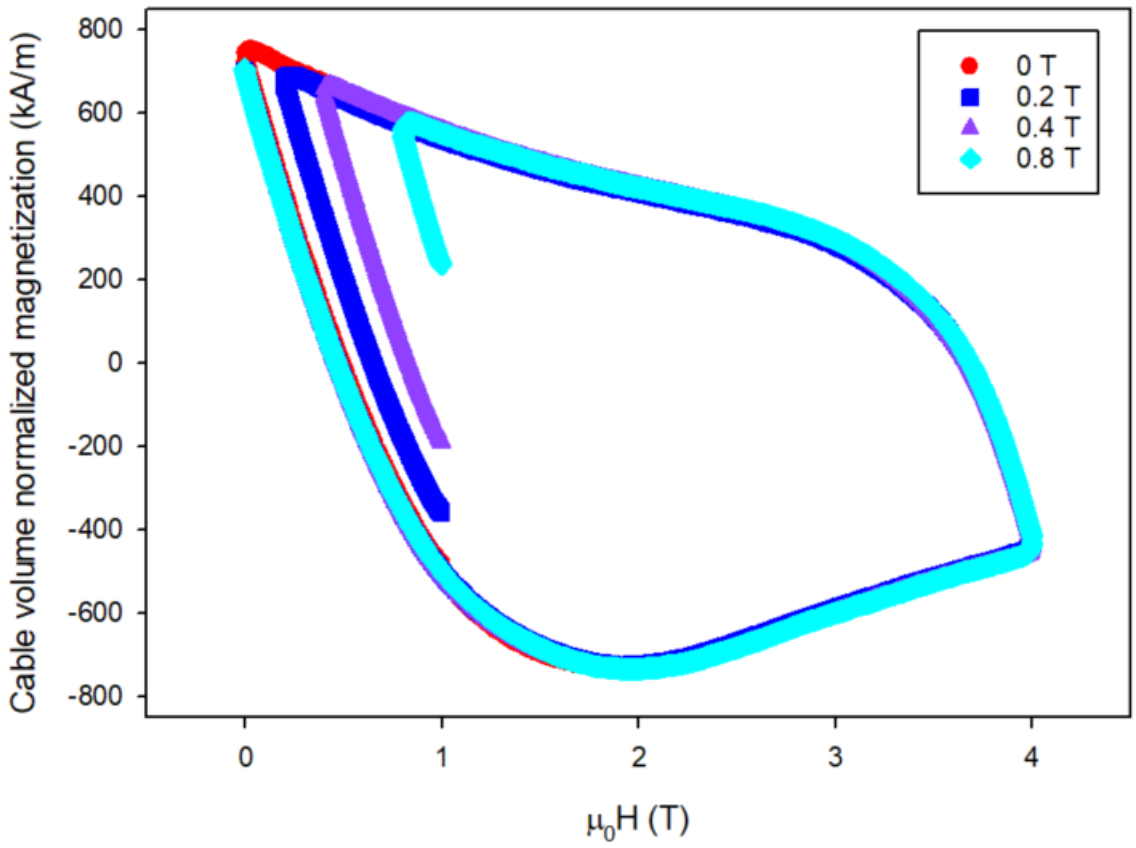

Figure 59: Cable volume normalized M-μ0H of STAR sample with different hold fields.

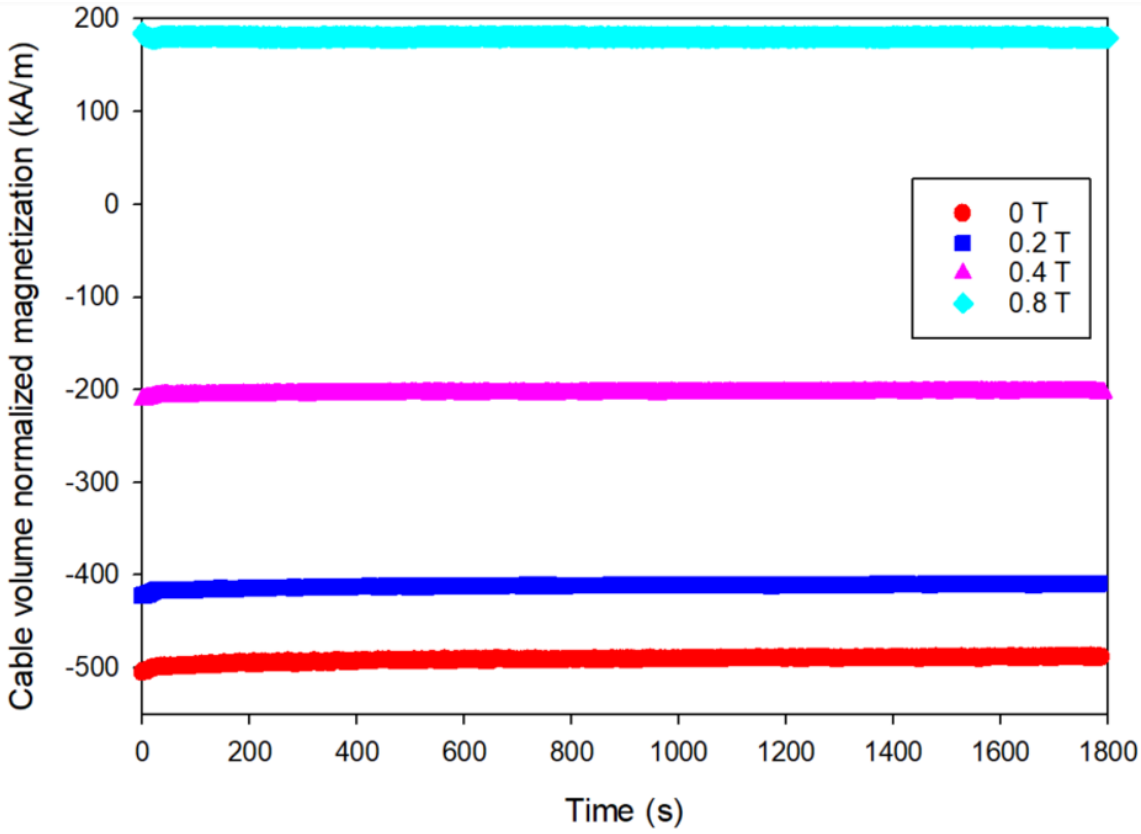

Figure 60: Flux creep in STAR cable with different hold field (0 T, 0.2 T, 0.4 T and 0.8 T)

Table 6: Initial magnetization and flux creep of STAR cable measured with different hold field.

Hold field (T)	Initial M (kA/m)	Flux creep (kA/m)
0	-505 kA/m	17.2 kA/m
0.2	-422 kA/m	12.2 kA/m
0.4	-210 kA/m	7.1 kA/m
0.8	185 kA/m	-5.8 kA/m
2	-1058 kA/m	66 kA/m

Table 6 shows the initial magnetizations and the resulting flux creep of the STAR cable. At the fully penetrated state, a hold field of -2 T, the initial magnetization was -1058 kA/m and the flux creep was 66 kA/m. At a hold field of 0 T, the initial magnetization was -505 kA/m and the flux creep was 17.2 kA/m. At a hold field of 0.2 T, the initial magnetization was -422 kA/m and the flux creep was 12.2 kA/m. At a hold field of 0.4 T, the initial magnetization was -210 kA/m and the flux

creep was 7.1 kA/m. At a hold field of 0.8 T, the initial magnetization was -185 kA/m and the flux creep was -5.8 kA/m. With these measured data, we plotted the M_0 vs. δM in Fig. 61. We concluded that for this particular STAR cable $\delta M = -14.71 + 13.94 * \exp(-0.0017 * M_0)$.

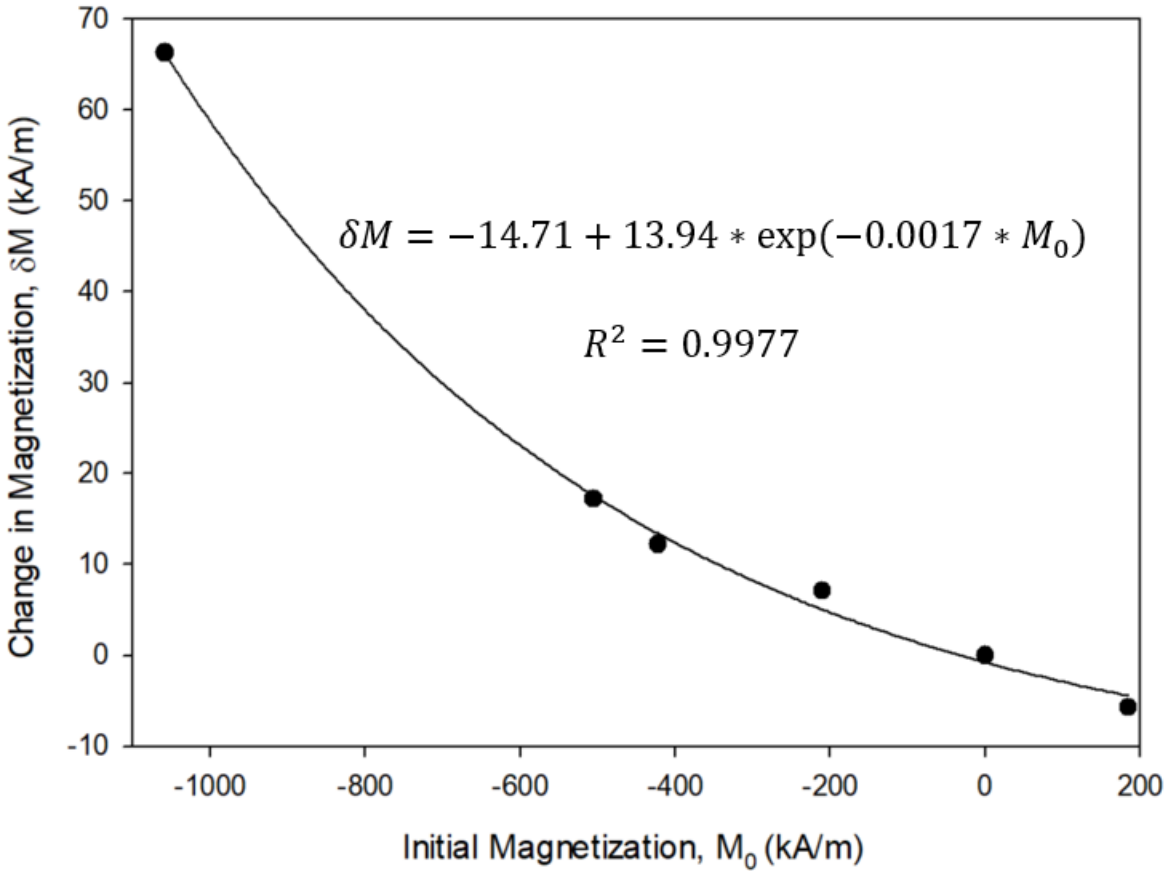

Figure 61: Flux creep as a function of initial magnetization for the STAR cable

4.2 AC loss measurement of a single Ni-replacement REBCO tape

AC loss measurements were carried out with the spinning magnet calorimeter (SMC) at the air force research laboratory (AFRL). The SMC has an 8-pole permanent magnet rotor in a Halbach configuration, Fig. 62 [137] [138]. The SMC can achieve a maximum field of 0.566 T, and at the maximum RPM of 3600, it can generate a maximum dB/dt of 543 T/s. Tests are conducted in a

liquid nitrogen environment. The sample AC loss is measured by the calorimeter based on the liquid nitrogen boiloff.

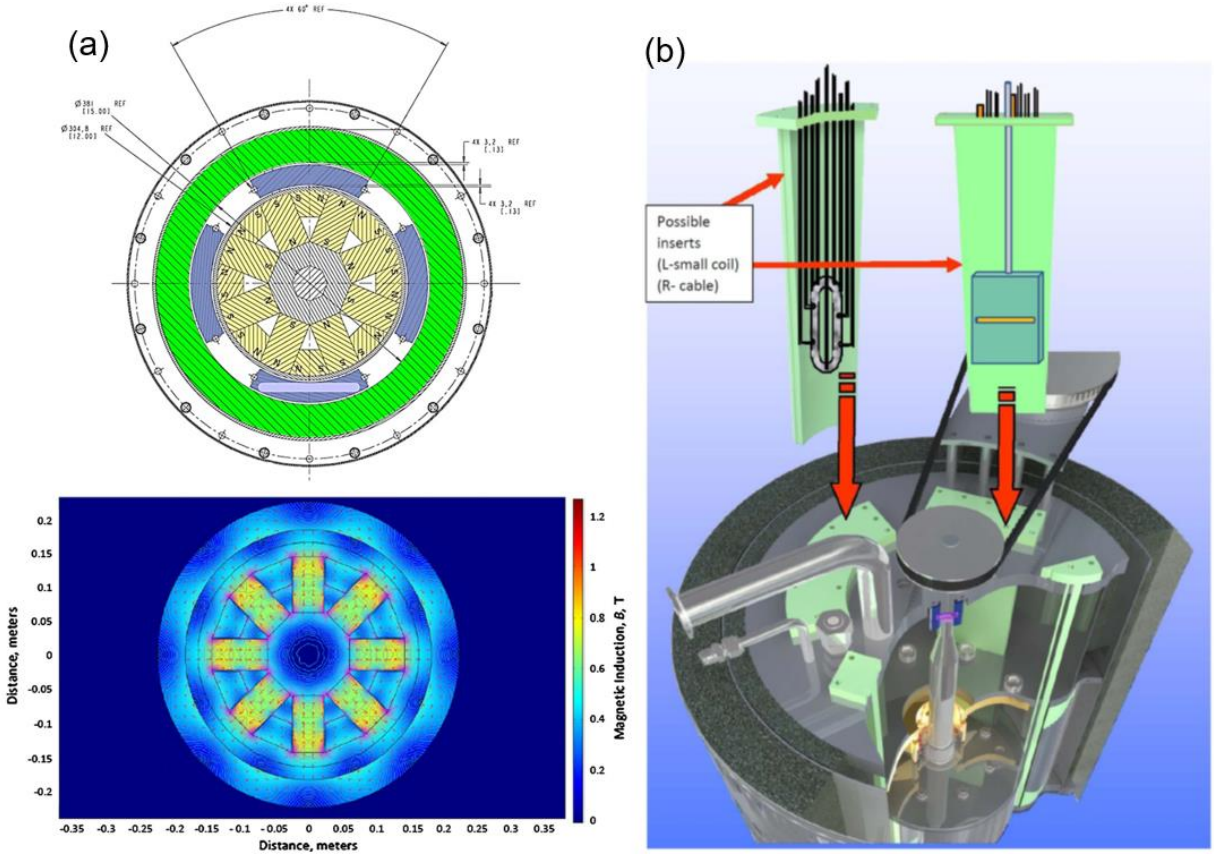

Figure 62: (a) An 8-pole permanent magnet rotor in a Halbach configuration [137], (b) 3D schematic of spinning magnet calorimeter system with cut away view, and calorimeter with sample inserts [138].

Before the samples were measured, two calibration runs were conducted to get the baseline nitrogen boiloff rate for later data analysis. The calibrations are shown in Fig. 63.

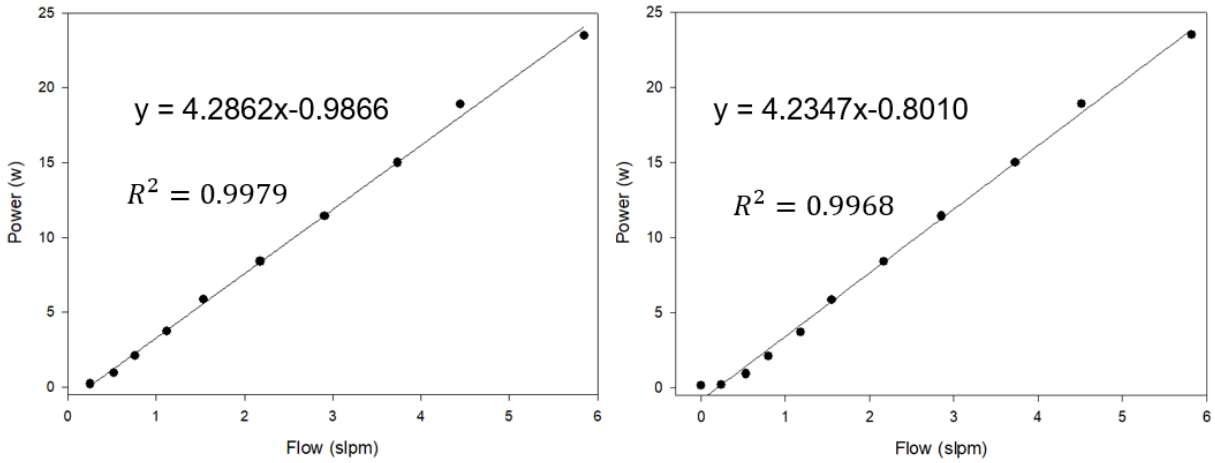

Figure 63: Calibration runs for SMC.

The first sample measured was a single tape processed by the Ni-replacement technique, section 2.4. The AC loss of this sample under frequencies varying from 10 Hz to 120 Hz are presented in Fig. 64. The fitting curve of the AC loss vs. frequency showed slightly 2nd order polynomial, indicating that the loss consisted of two parts, hysteresis loss and Eddy current loss. Therefore, the loss, P_{AC}, can be expressed as equation 27, where the first term represents the hysteresis loss, the second term represents the eddy current loss, w is width of the tape, I_c is the critical current, B_{max} is the amplitude of the sweeping field, f is the frequency of the sweeping field, and ρ is the resistivity of the metal layer [138].

$$P_{AC(hys+eddy)} = wI_cB_{max}f + \frac{\pi^2}{6\rho}(B_{max}wf)^2 \qquad Eq.27$$

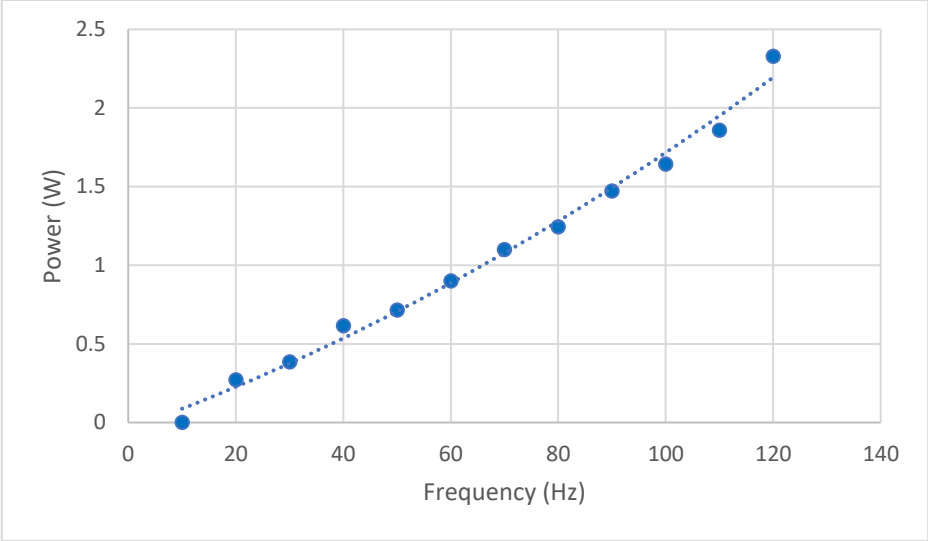

Figure 64: AC loss of Ni-replacement sample

Dividing both sides of equation 27 by $wB_{max}f$, we get equation 28 that has the critical current of the REBCO tape as intercept and the eddy current loss constant, C_{eddy}, as slope [138]. For this particular Ni-replacement sample, shown in Fig. 65, the extracted critical current is 102.5 A at 77 K, which is in the reasonable range of a REBCO CCs [68].

$$\frac{P_{AC(hys+eddy)}}{wB_{max}f} = I_c + \frac{\pi^2}{6\rho}B_{max}wf = I_c + C_{eddy}f \qquad Eq.28$$

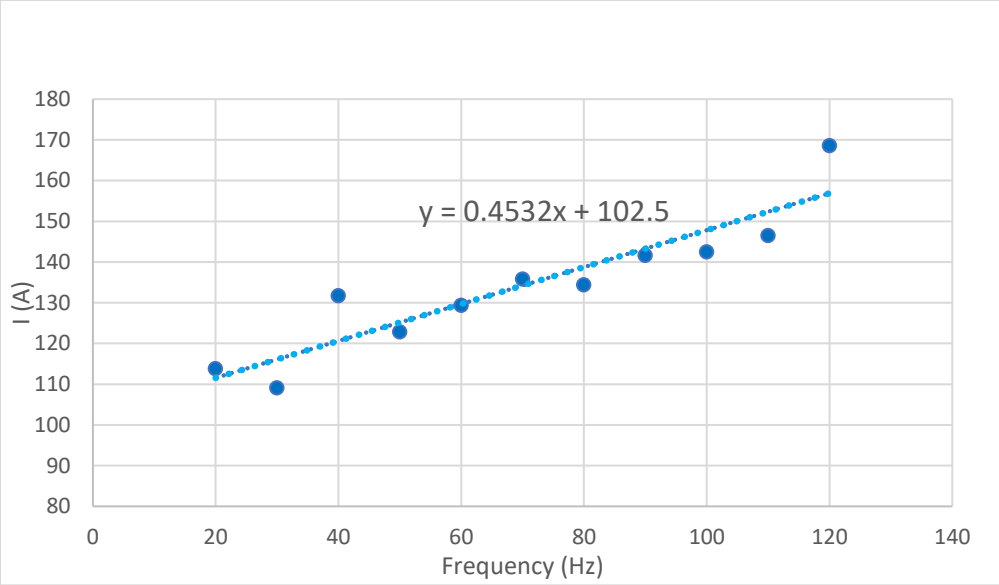

Figure 65: Critical current of the Ni-replacement sample based on AC loss measurement.

4.3 AC loss measurement of a 9-layer Ni-plated Roebel cable

Next, we measured the AC loss of a 9-layer Ni-plated Roebel cable using the same approach described in section 4.2. As listed in table 7 [139], the Roebel cable consisted of 9 tapes. The original tapes, manufactured by SuperPower Inc., were sent to Karlsruhe Institute of Technology for cutting and winding into a Roebel cable. Each individual tape in the cable had a width of 5.6 mm. Given an inter-strand gap distance of 0.4 mm, the width of the cable was 11.8 mm. The cable had a twist pitch length of 126 mm and the I_c of the cable measured at 77 K was 1168 A.

Table 7: Specifications of Roebel cable [139]

Parameter	Specification
REBCO tape manufacturer	SuperPower Inc.
Roebel cable manufacturer	Karlsruhe Institute of Technology
Number of Tapes	9
Tape Width (mm)	5.6

Cable Width (mm)	11.8
Tape thickness (mm)	0.1
Pitch Length (mm)	126
Cross-over angle (degree)	40
Inter-strand gap (mm)	0.4
I_c at 77 K (A)	1168

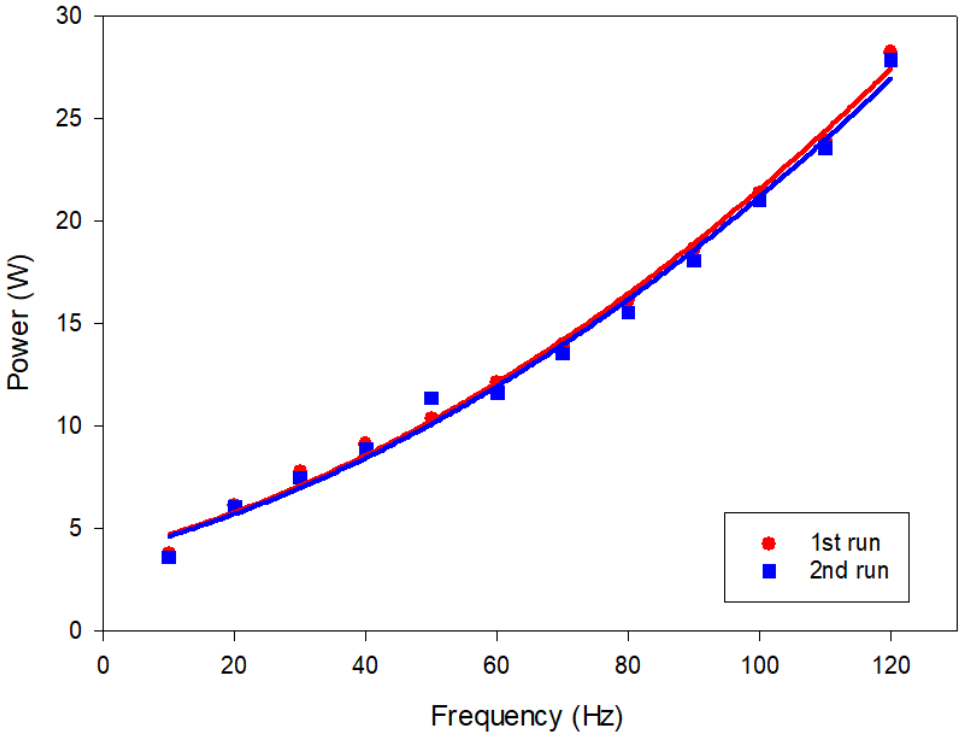

Figure 66: AC loss measurements of Ni-plated Roebel cable.

We did two measurements on this cable with a field amplitude of 0.566 T and a sweeping frequency from 10 to 120 Hz. The results are presented in Fig. 66. The two measurements, which provided highly consistent results, showed a weak quadratic frequency dependence.

Because the tapes in this Ni-plated Roebel cable were in loose contact, they possessed a high inter-strand electrical contact resistance. As a result, the coupling current loss should be negligible

and the measured loss should be comprised of two components, hysteresis loss and eddy current loss, as demonstrated in equation 27. At low frequency, hysteresis loss was dominant, while at high frequency, eddy current loss was the major loss component. Therefore, we used the low frequency data to extrapolate a linear relation between hysteretic loss and frequency. After extending this linear fit and the 2nd order polynomial to 200 Hz. We found, in Fig. 67, that at a frequency of 200 Hz, the eddy current loss component became 39% of the total loss.

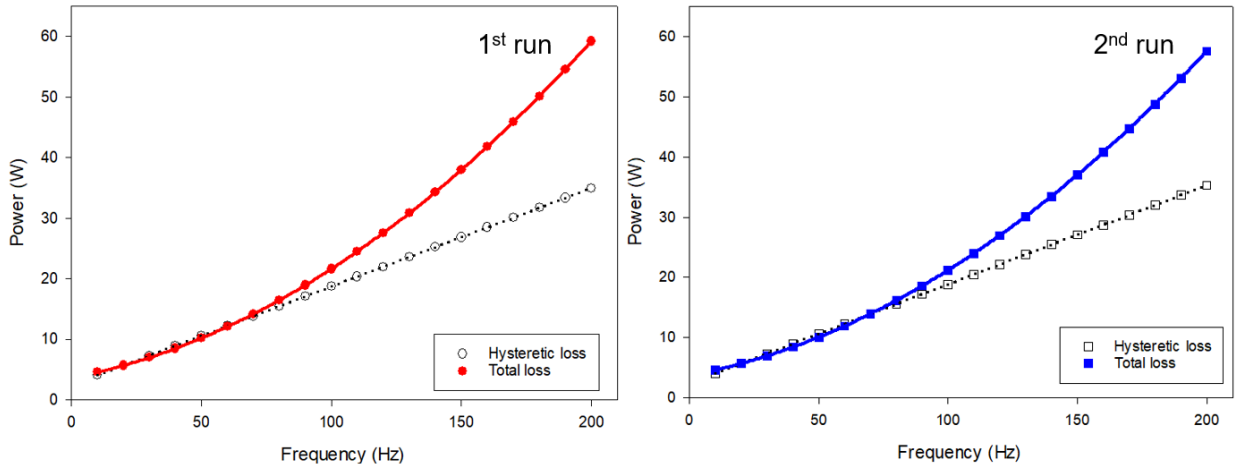

Figure 67: Total AC loss and Hysteresis loss in the Ni-plated Roebel cable.

However, when we tried to extract the I_c from AC loss measurements, as shown in Fig. 68, we found that the extrated I_c of a single tape was only 34.30 A. This is much smaller than the nominal I_c of a single tape, which is 130 A.

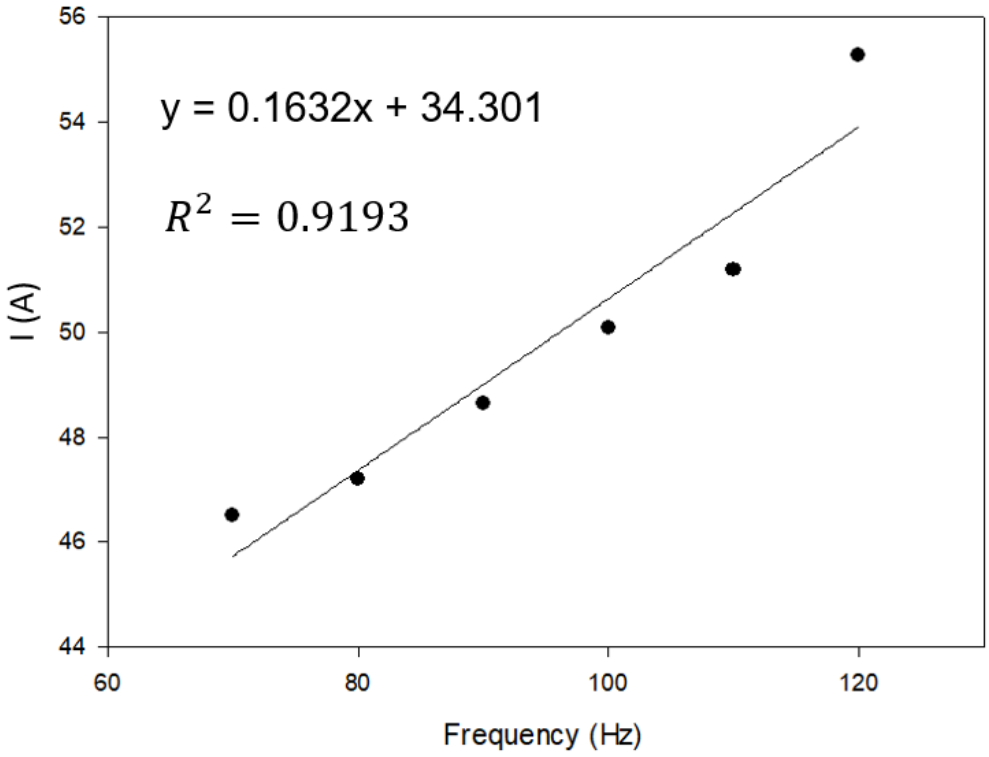

Figure 68: Critical current of the 9-tape Ni-plated Roebel cable based on AC loss measurement.

To explain this reduced *Ic*, we note that equation 27 and 28 only apply when the superconductor is fully flux penetrated. However, based on previous study, the flux penetration field of the original Roebel cable is around 1.2 T. Fig. 69 [52]. Ni-plating does not change the flux penetration field significantly, so the Ni-plated Roebel cable should have a similar flux penetration field as the original tape. The maximum field amplitude of the SMC at 0.566 T is much smaller than the sample flux penetration field, 1.2 T, so a strong demagnetization effect existed in the sample. By comparing the extracted I_c, 34.30 A, with the nominal I_c, 130 A, the demagnetization factor was about 3.79.

At a demagnetization factor of 3.79, the eddy current constant of the Ni-plated Roebel cable should be $C_{eddy} = 3.79^2 * 0.1632 = 2.34$ if the cable is fully flux penetrated. Given a room temperature electrical resistivity of Cu to be $1.7*10^{-8}\ \Omega * m$, a room temperature electrical

resistivity of Ni to be 7*10$^{-8}\,\Omega * m$, and assuming the RR ($\rho_{300\,k}/\rho_{77k}$) of both the electro-plated Cu and Ni to be approximately the same (~10), the eddy current in the Ni-placed Roebel cable should mainly flow in the Cu layer because Cu had much lower resistivity than Ni, while the eddy current in the Ni-replacement REBCO tape, discussed in section 4.2, should mainly flow in the Ni layer. Therefore, theoretically the eddy current constant of the Ni-plate Roebel cable should be 5.76 times that of the Ni-replacement sample ($^{w_{Ni-plated}}/_{\rho_{Cu}}$: $^{w_{Ni-replacement}}/_{\rho_{Ni}}$). Based on our direct measurement, the ratio of the eddy current constants is 2.34/0.45 = 5.2, which was in reasonable agreement with the theoretical value, 5.76. In addition, it can be concluded that replacement of the Cu stabilizer on the REBCO CCs with Ni can be an effective method for reducing the eddy current loss in coated conductors.

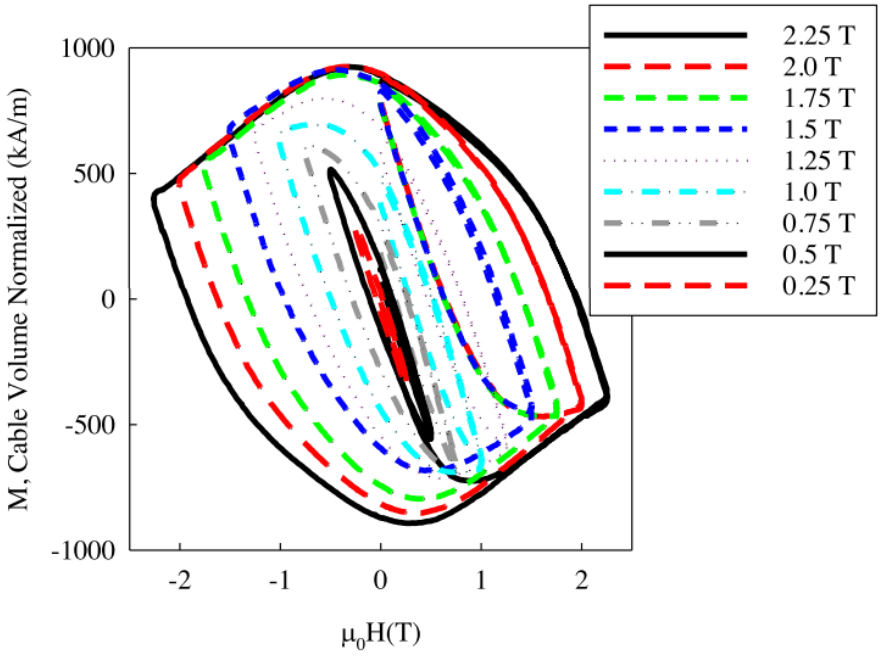

Figure 69: Magnetization of Roebel cable measured under sweeping field with different amplitude [52].

Chapter 5- AC loss simulation in REBCO conductors.

AC loss has been a limiting factor for the applications of REBCO conductors in time-varying magnetic fields. Therefore, understanding and quantifying the AC loss of REBCO conductors in a time-varying magnetic field is necessary. In this section, I will introduce several models that can be used to predict the AC loss of REBCO coated conductors.

5.1 AC loss in two-tape stack with different inter-strand properties

The first set of models were two-tape stacks. We considered two scenarios, one with pure metallic inter-strand contact property, Fig. 70 (a), and the other with insulating inter-strand contact property, Fig. 70. (b).

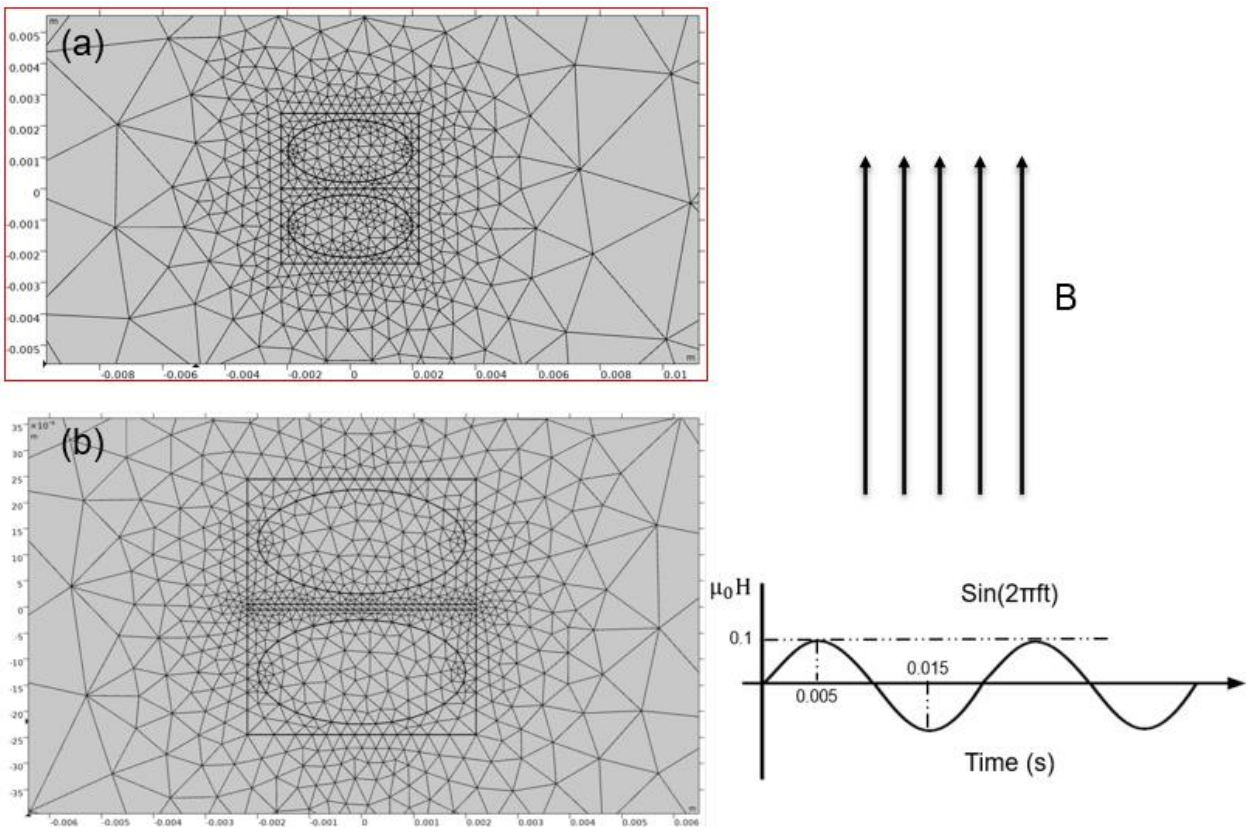

Figure 70: Two-tape stack model (a) metallic inter-strand contact, (b) insulating inter-strand contact.

Table 8:Parameters of two-tape stack model.

n value	20
YBCO width	4 mm
YBCO thickness	2 mm
Ic of tape	150 A
Diluted Jc	2.4E7 $\mathrm{A/m^2}$
Thickness of Cu	0.2 mm
Barrier thickness	0.1 mm
Barrier resistivity	5000 Ω*m
Frequency	50 Hz
$\mathrm{B_{max}}$	0.1 T

Table 8 listed the parameters used in this two-tape stack model. When the two-tape stack was placed into a time-varying magnetic field with an amplitude of 0.1 T and frequency of 50 Hz, the AC loss in the two scenarios with two different inter-strand contact property were almost identical. The total loss per cycle was 0.192 J/m, with 0.188 J/m distributed in the superconductors and 0.0038 J/m distributed in the Cu stabilizer. Comparing the two scenarios, the AC loss in the resistive barrier was negligible.

Then we investigated the demagnetization effect of overlayed tapes with this two-tape stack model. We compared the relative permeability of the two-tape stacks with and without the superconductor parts. As shown in Fig. 71, when the superconductor parts were present, at a

field amplitude of 0.1 T, the middle region of the stack was shielded away from magnetic flux, leading to a relative permeability of $u_{r,with\ sc} = 0.22$. When the superconductor parts were replaced with air, the stack was fully penetrated at 0.1 T, and the relative permeability of the structure became $u_{r,no\ sc} = 0.83$. Hence, we could conclude a demagnetization factor of 0.83/0.22 = 3.77, which was a good agreement with the result of direct measurement, 3.79, described in section 4.3.

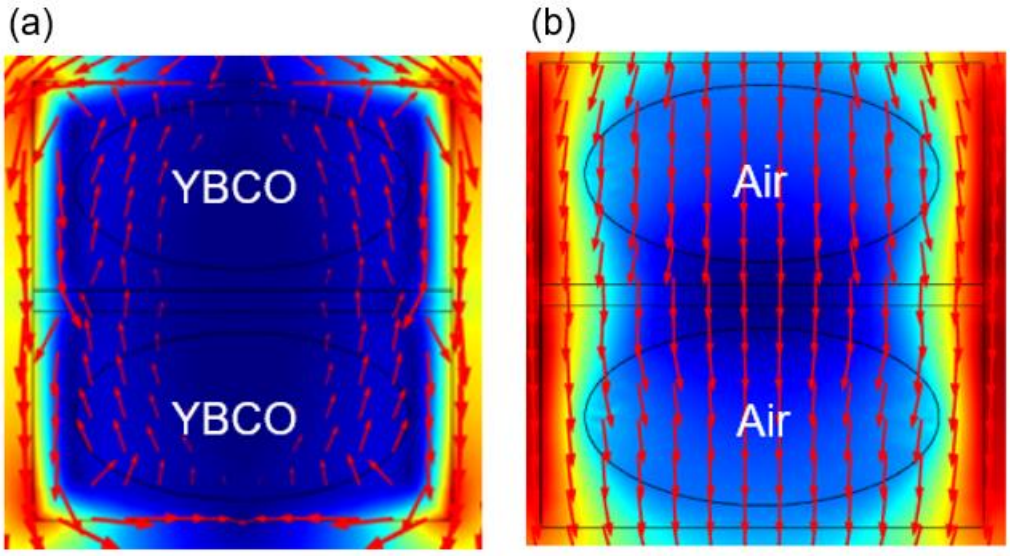

Figure 71: Magnetic flux in the two-tape stack (a) with superconductor (b) without superconductor

5.2 AC loss in seven-tape Roebel cable with good inter-strand contact

Then we investigated the AC loss in a more complex structure. A 2D seven-layer Roebel cable was made as shown in Fig. 72. In this case, we assumed the inter-strand contact to be metallic. Therefore, capturing the transposing structure of the Roebel cable was critical to achieve precise simulation of the AC loss induced due to the inter-strand coupling current. The 2D model, hence, was built to mimic the cross-section circled in Fig. 73 [140].

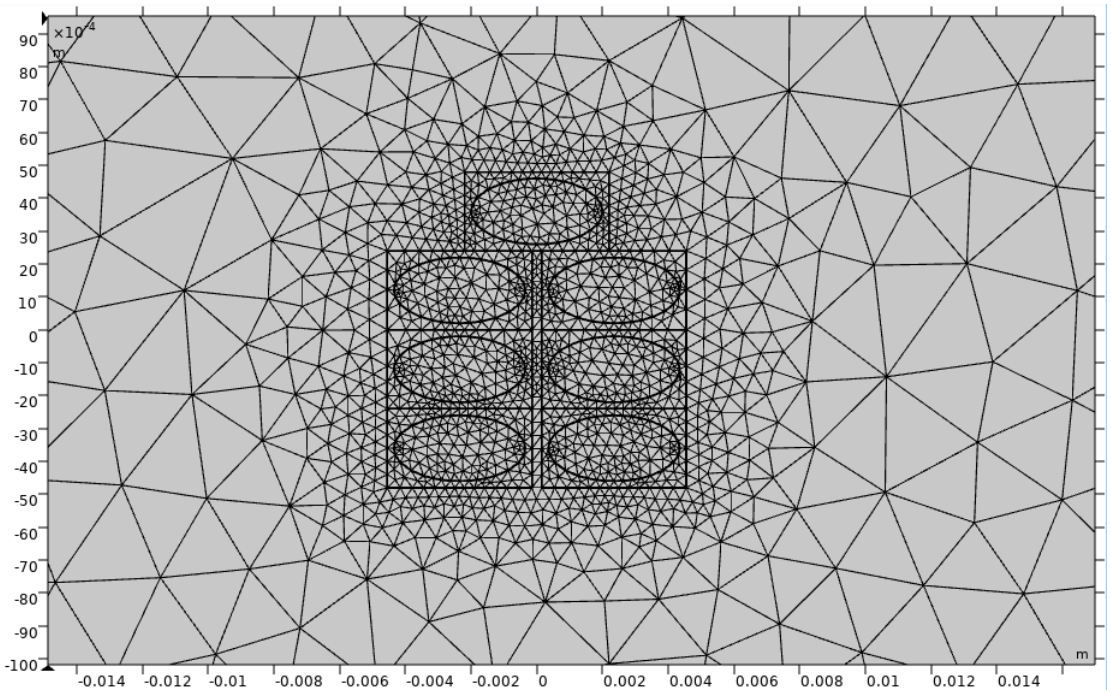

Figure 72: 2D model of seven-layer Roebel cable.

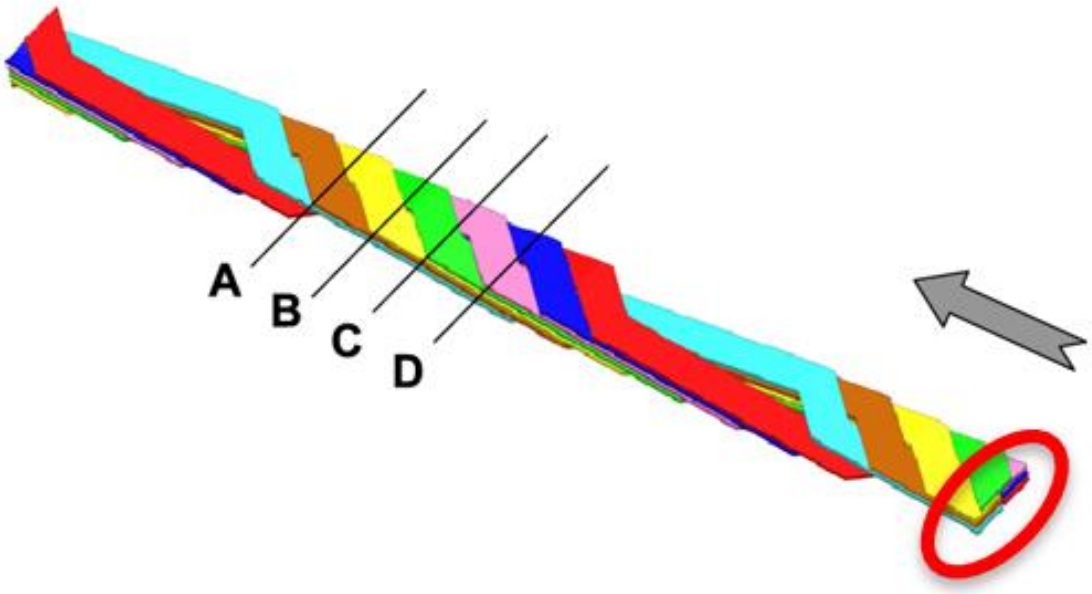

Figure 73: 3D structure of Roebel cable [140]

Table 9: Parameters of seven-layer Roebel cable model

n-value	20
YBCO width	4 mm
YBCO thickness	2 mm
Ic of single tape	150 A
Diluted Jc	2.4E7 $\mathrm{A/m^2}$
Thickness of Cu	0.2 mm
Gap distance	0.3 mm
Frequency	50 Hz
$\mathrm{B_{max}}$	0.1 T

Table 9 lists the input parameters of the seven-layer Roebel cable model. Given a field amplitude of 0.1 T and a frequency of 50 Hz, the evolution of magnetic flux and magnetic flux induced current in the seven-layer Roebel cable was calculated. The results are presented in Fig. 74 and 75.

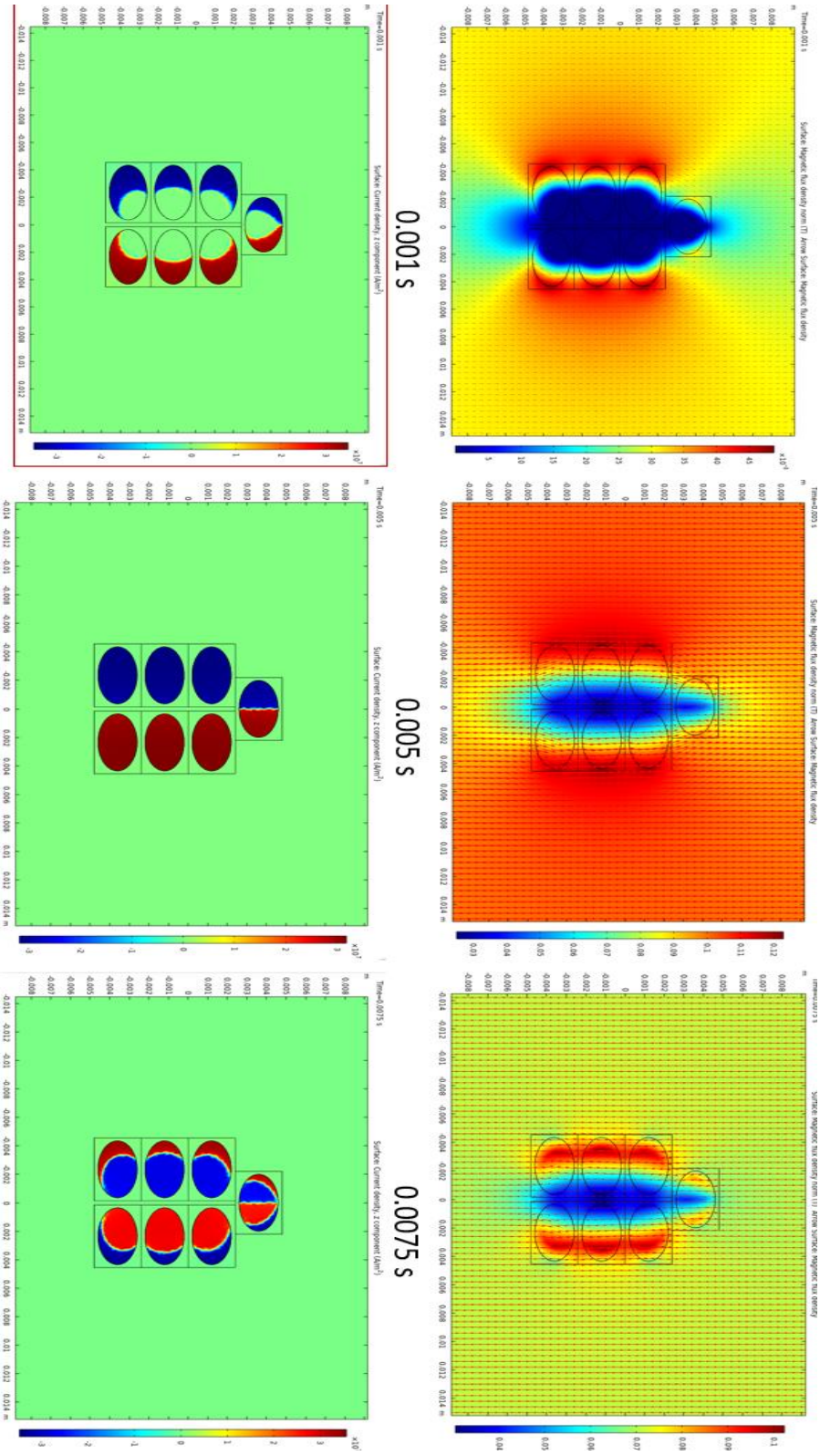

Figure 74: Evolution of magnetic flux and magnetic flux induced current in the seven-layer Roebel cable from 0 s to 0.0075 s.

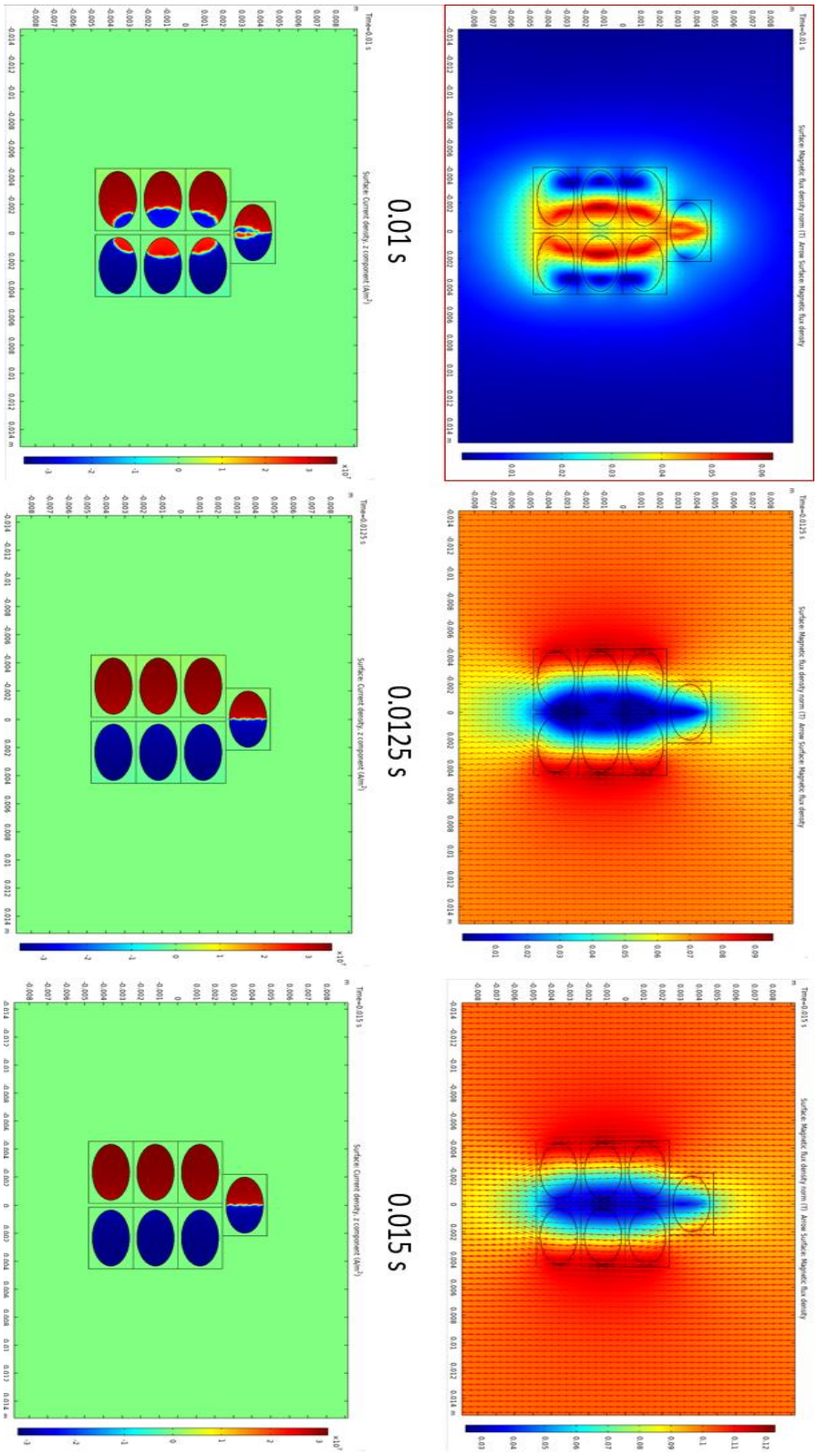

Figure 75: Evolution of magnetic flux and magnetic flux induced current in the seven-layer Roebel cable from 0.0075 s to 0.015 s.

According to the current profiles shown in Fig. 74 and 75, the induced current went into the page from one side of the cable, bridged through the top tape, and flowed out of the page from the other side of the cable. Moreover, the current distribution was dominant in the superconductor regions. The total AC loss per cycle from the simulation was 0.78 J/m, giving 0.75 J/m in the superconductor and 0.023 J/m in Cu. Therefore, the simulation signals a strong recoupling effect, which implies that the multi-strand cable behaves like a bulk superconductor.

To better understanding the simulation result, we compared the simulation to a direct AC loss measurement of a Roebel cable conducted by our group [141]. The Roebel cable get measured in ref. [141] had specifications as shown in table 10. In this real cable, the number of tapes was 15, and the twist pitch was 30 cm. Effective current transferring from one tape to another was ensured in this cable by soldering the tapes face to face by Cu strips. As shown in Fig. 76, under a field amplitude of 0.1 T and a frequency of 50 Hz, the AC loss per cycle of the cable was around 0.61 J/m. The fact that the power loss was not frequency dependent indicate that the cable was recoupled.

Table 10: Cable specification of Roebel cable [141]

Cable width, w_c(mm)	12
Cable thickness, a (mm)	1.5
Cable twist pitch, L_p (cm)	30

Cable length (cm)	30
Number of tapes in the cable, N	15
Tape width, w (mm)	5
Tape thickness (mm)	0.1
Cable I_c (77.3 K, self field) (A)	1537.5
Cu strip width (mm)	5
Cu strip length (mm)	11
Cu strip thickness (mm)	0.1
Cu strip separation on one side of the cable (cm)	2
Cu strip separation on top and bottom side of the cable (cm)	1
Number of Cu strips	38

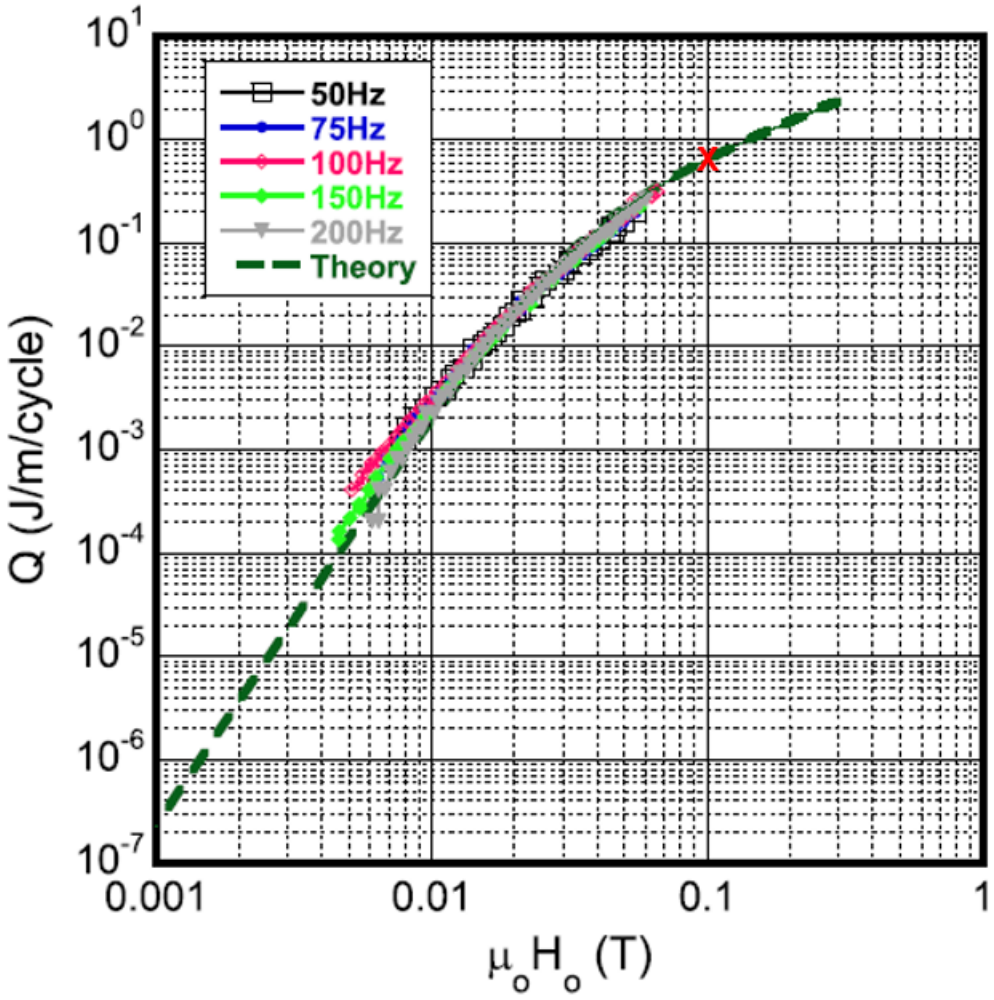

Figure 76: AC loss measurement of 15-tape Roebel cable with soldered Cu shims in between tapes [141].

Because the model we used for AC loss simulation was 2D, it was not able to demonstrate the twist pitch, which was a 3D character. To better compare the simulation with the experimental result, some adjustments were needed. The unit of the AC loss from the simulation is J/m per cycle, which entails an underlying message that the twist pitch assumed by the software in the simulation was 1 meter, which was 3.33 time of the twist pitch of the real 15-layer Roebel cable. The recoupling current loss per meter is linearly dependent on the twist pitch of the cable, the sheet critical current density of the cable (I_c/w), and the square of the of the conductor width of

the cable. Therefore, the AC loss per cycle of the15-layer Roebel cable can be calculated based on the seven-tape model as, $0.78\ \left(\frac{J}{m}\right) * \left(\frac{1}{3.33}\right) * \left(\frac{\frac{1537.5}{0.012}\left(\frac{A}{m}\right)}{150*\frac{7}{0.0091}\left(\frac{A}{m}\right)}\right) * \left(\frac{0.012\ m}{0.0091\ m}\right)^2 = 0.494\ (\frac{J}{m})$. The relative error between the calculated AC loss and the experiment result is 19 %, and this is an acceptable error for AC loss simulation.

We further verified the recoupling result by some theoretical calculations. For the superconductor to reach the recoupling state in the time varying field, the frequency of the field needs to be greater than the critical frequency, f_1. This frequency is given by equation 29, where ρ is the resistivity of the Cu stabilizer, μ_0 is the permeability of free space, μ_r is the relative permeability of the cable, and L_p is the twist pitch length [142] [143]. Given a twist pitch of 30 cm, from table 10, and a relative permeability of 0.22, from section 5.1, the critical frequency, f_1, for recoupling the Roebel cable is around 1.04 Hz. Hence, given a field frequency of 50 Hz, the Roebel cable should ensure recoupling.

$$f_1 = \frac{4\pi\rho}{\mu_0 * \mu_r * L_p^2} \qquad Eq.29$$

Chapter 6- Transvers mechanical properties of REBCO coated conductors.

From the previous chapters, we can conclude that the inter-strand contact properties play significant roles in the applications of REBCO CCs because they will determine current sharing and AC losses in a REBCO CC. One of the easiest and direct way to control the inter-strand contact properties is applying compression. Hence, it is necessary to know the mechanical behaviors of tape stacks and cables under pressure.

The last section in this dissertation is the transverse mechanical properties of REBCO CCs, and the results were published in ref. [144]. Previous studies have demonstrated magnets wound with REBCO coated conductors tape, Roebel cables, and Conductor on Round Core (CORC) cables exhibit outstanding performance [1] [70] [71] [74] [145] [146] [147] [148]. Those coils were wound under tension. Then during operation, due to the Lorentz force, a transverse stress ranging from 100 MPa to 300 MPa will be exerted on the tape/cable surface [100] [149] [150].

In non-insulation coils, this transverse pressure can be utilized as a method to reduce the inter-tape/cable contact resistance (ICR) [151]. Under a transverse pressure greater than 100 MPa, the inter-strand contact efficiency, η ($\eta = ICR * contact\ area$), will be smaller than 50 μΩ*cm^2. This can lead to good current sharing between tapes and improve coil stability [93] [117].

On the other hand, such a high stress level may lead to damage to the cables. For direct tape-to-tape contact, critical current degradation is limited to 2% under compression of 200 MPa, and less than 8% under compression of 550 MPa [152]. However, in the case of Roebel cable and CORC cable, due to the nature of the transposing tapes, their stress limits will tend to be closer to their shear stress (~19 MPa) and cleavage stress (~1 MPa) [153] [154] [155]. Therefore, the critical

currents of Roebel cable and CORC cable are much more sensitive to pressure than tape stacks. The transverse pressure tolerance of critical current in Roebel cable is around 30-40 MPa [150] [152] [156]. Appreciable degradation of critical current in CORC cable starts at a pressure level of around 1.2 MPa, and as the diameter of the former decreases, the degradation of critical current due to transverse pressure becomes more severe [157] [158].

Here we performed compression tests on 4 types of samples, shown in Fig.77, including 10-layer REBCO coated conductor tape stack, 10-layer Ni-plated REBCO coated conductor tape stack, Roebel cable, and CORC cable. The results concluded from this work can be applied to magnet design and as input parameters for magnet simulation.

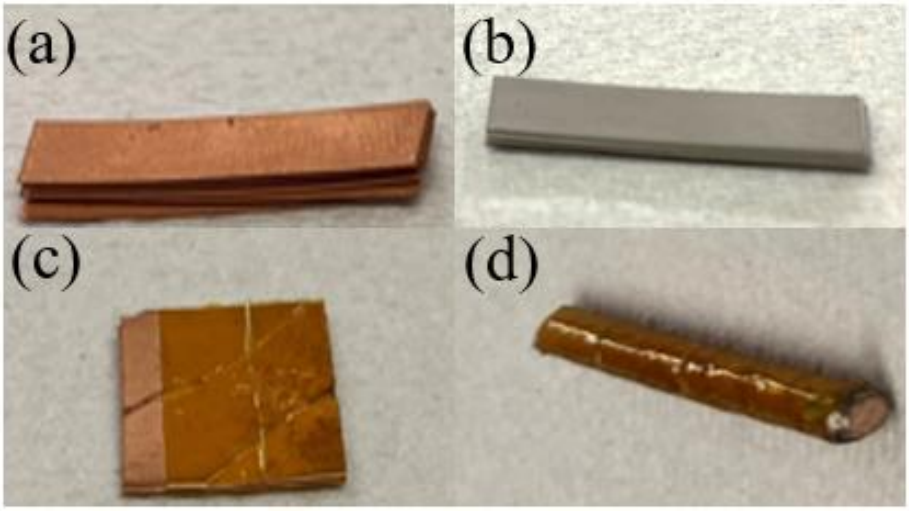

Figure 77: (a) 10-layer REBCO tape stack, (b) 10-layer Ni-plated tape stack, (c) Roebel cable, (d) CORC cable.

Sample 1 (24 mm * 4 mm * 1.3 mm) consists of 10 layers of commercially available SuperPower-SCS4050 2G HTS tapes (SP), and the specifications are given in table 11. Sample 2 (24 mm * 4.06 mm * 1.9 mm) is a ten-layer Ni-plated REBCO tape stack. Detailed Ni-plating process can be found in [97]. Sample 3 (15.8 mm * 11.8 mm * 1 mm) is a 9-layer Roebel cable

that was fabricated by Karlsruhe Institute of Technology with SuperPower tape, and the cable specifications are listed in table 12. Sample 4 (24 mm in length) is a segment of a CORC cable provided by the Lawrence Berkeley national laboratory (LBNL) with ID 160823-Berkeley 250-C [136]. The CORC sample specifications are listed in table 13. For Samples 1 and 2 we performed five sets of tests on each. For Samples 3 and 4, we performed three sets of tests on each.

Table 11: Specifications of the REBCO coated conductors, Sample 1

Component	**Thickness (μm)**
Cu stabilizer - YBCO side	20
Silver overlayer 1	2
REBCO	1
Buffer stack	0.2
Hastelloy	50
Silver overlayer 2	1.8
Cu stabilizer - substrate side	20
Tape thickness (mm)	~0.1
Stack Thickness (mm)	~ 1.3

Table 12: Specifications of Roebel cable, Sample 3

Number of tapes in the cable	9
Tape width (mm)	5.6
Cable width (mm)	11.8
Pitch length (mm)	13
Cross-over angle (degree)	40
Inter-tape gap distance (mm)	0.4

Tape thickness (mm)	~0.1
Cable Thickness (mm)	~ 1

Table 13: Specifications of CORC cable, Sample 4

Number of tapes in the cable	16
Cable diameter (mm)	3.4
Tape width (mm)	2
Tape thickness (mm)	0.045
Pitch length (mm)	6.22

We used MTS (model 43), shown in Fig. 78 (a), for all compression tests. However, because all samples have thicknesses smaller than 3.5 mm, the systematic error from the testing frame is bigger than the thicknesses of the samples. Hence, it is necessary to subtract the error from the loading frame. We used 4 pieces of polycrystalline non-heat-treated copper blocks to perform error calibration. The dimensions of each copper block are 20 mm* 12 mm* 8 mm so that the surface area under compression is similar to those of Sample 1, 2 and 4. As shown in Fig. 78 (b), the copper block was marked with two silver tapes, and a laser extensometer (model LE-01) was used to measure the displacement of the copper block. We applied pressures up to 200 MPa. Based on the value measured by the loading frame which contains the system error and the value measured by the laser extensometer which is the displacement of the sample, we were able to conclude an error correction function. Then we applied the error correction function to all the other measurements to calculate strains corresponding to stress levels. For Sample 1, 2, and 4 we applied stresses up to 200 MPa. Sample 3 was tested up to 80 MPa. To make sure the samples

were in contact with the testing frame, we used precision control to lower the pressing unit until we saw there was a small non-zero force exerted on the samples. Then we started measurements and applied a 0.003 mm/s strain rate for all samples.

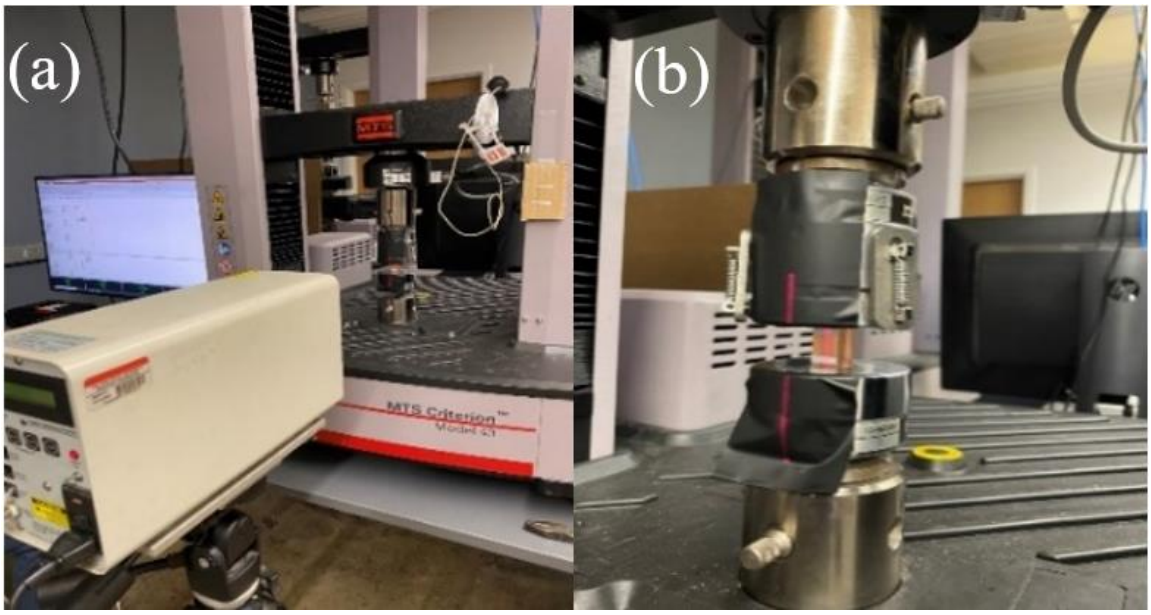

Figure 78: (a) MTS model 43 testing frame, (b) error calibration of testing frame.

Surface roughness measurements were applied to Sample 1, 2, and 3 before and after the compression test by using the optical profilometer, shown in Fig. 79 (Veeco, model Contour GT-K). The purpose of surface roughness measurement was to confirm that an appreciable amount of plastic deformation occurred during the compression test. For each sample, 8 measurements were taken to get good statistics. The roughness is presented as average roughness, S_a, which can be interpreted as the deviation of a surface height from its mean height.

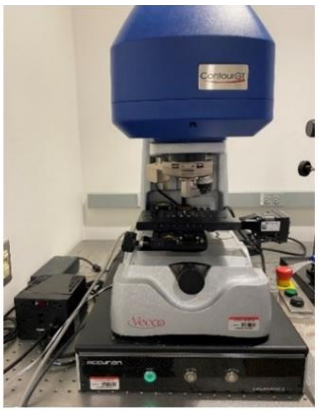

Figure 79: Veeco model Contour GT-K optical profilometer

6.1 Compression test on tape stacks

The stress-strain behavior for Sample 1, the 10-layer REBCO tape stack, is presented in Fig. 80 (a). The curve can be divided into three different regimes that are presented in the insets. Because the tapes contain curvature and their surfaces have certain roughness, as shown in Fig. 81 (a), when 10 tapes are combined to form a tape stack, the thickness of the stack is about 30% more than the thickness of adding up 10 individual tapes. Therefore, in the first regime, where the pressure level was below 20 MPa and the strain was within 0.23, the displacement was mainly due to sample flattening, reducing the curvature, and tape self-relocation. For the second regime, where the pressure increased up to 60 MPa with 0.0135 additional strain, stress-strain behavior became mostly linear, and it showed a modulus of around $3.1 \pm 7\%$ GPa. The third regime of the stress-strain curve was a combination of elastic and plastic deformation. We fitted the third regime still linearly, because we thought that elastic deformation was more dominant, and the five sets of measurements showed an average modulus of $10 \pm 11\%$ GPa for the third regime.

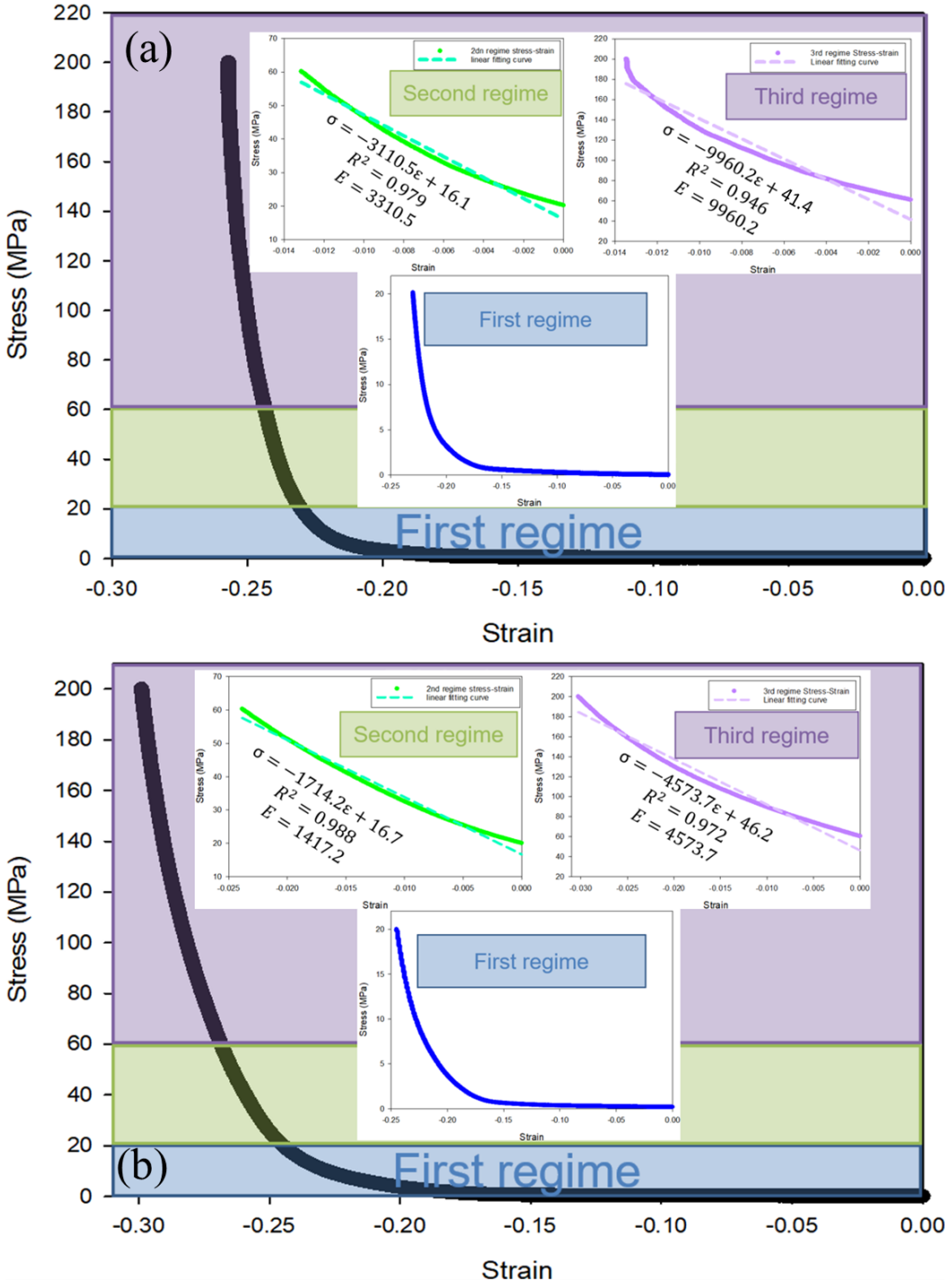

Figure 80: Stress-Strain curve of (a) Sample 1, (b) Sample 2. (Strain is determined as ΔL/L.)

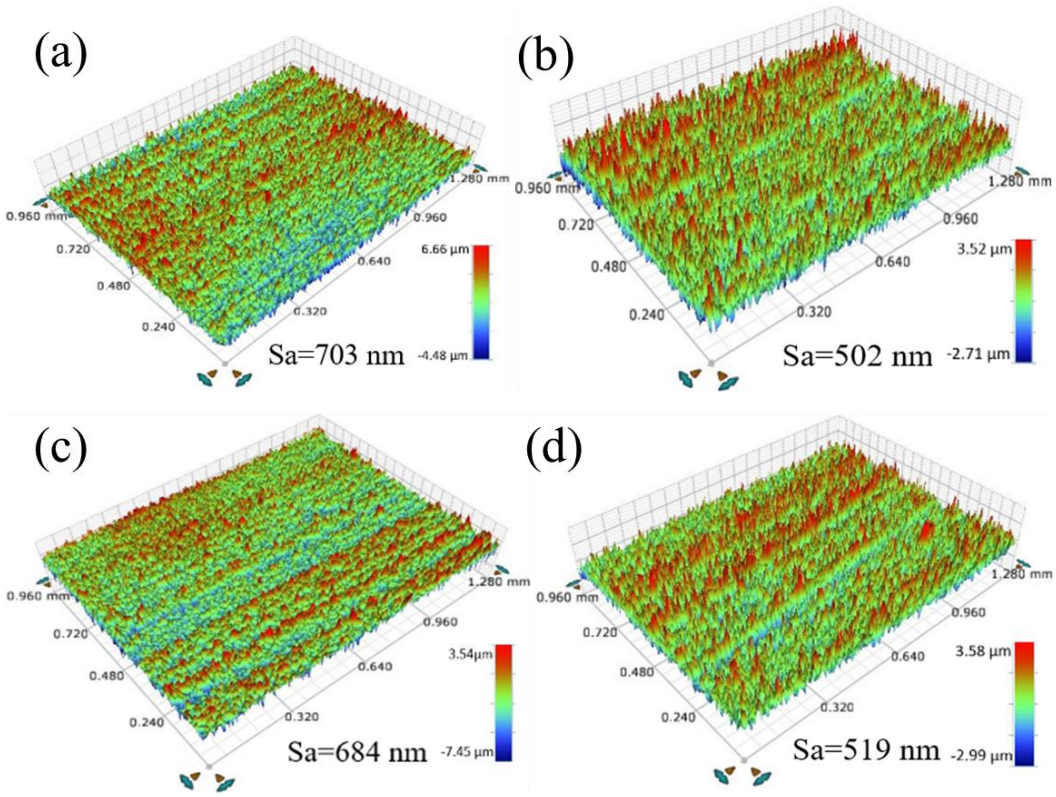

Figure 81: Surface roughness of (a) Sample 1 before pressing, (b) Sample 1 after pressing, (c) Sample 2 before pressing, (d) Sample 2 after pressing.

As shown in Fig. 80 (b), Sample 2, the 10-layer Ni-plated REBCO tape stack, exhibited similar stress-strain behavior as Sample 1. The first regime was below 20 MPa, and the sample underwent 0.25 strain. The second regime was within the compression range from 20 MPa to 60 MPa, and it showed a modulus of 1.7 $\pm$ 6% GPa. The third regime which was above 60 MPa gave a modulus of 4.6 $\pm$ 9% GPa. In comparison with Sample 1, Sample 2 had lower modulus in both the second and third regimes, because Ni-plating introduced additional less stiff material relative to Hastelloy into the structure, and it is a typical trend for REBCO coated conductor tape that tape modulus decreases with increasing plating layer thickness.

The moduli extracted based on our measurement for both Sample 1 and 2 in the second and third regimes are low compared to the moduli of polycrystalline Cu and Ni which range from 100

GPa to 200 GPa. For both Samples 1 and 2, the second and third regimes contained certain plastic deformation and related work hardening. This could be a result due to the surface roughness of the tape, which could lead to a much higher local stress than the nominal stress value. More evidently, from Fig. 81, it can be seen that the average surface roughness of Sample 1 reduced from 703 nm to 502 nm (~29 % reduction), and the surface roughness of Sample 2 reduced from 684 nm to 519 nm (~24 % reduction). In addition, the amount of strain (>0.01) governed by the concluded modulus values were much larger than the technically specified strain limit (0.0002) for elastic modulus. In this case, it would be better to compare our results with the tangent moduli of materials that are commonly adopted to the classical bilinear isotropic hardening model which is used to perform FEM analyses on REBCO coated conductor tapes [159] [160] [161]. The tangent modulus of copper is 4 GPa. For sample 1, the modulus of the second regime (3.1 GPa) was close to the tangent modulus of copper. Then, as pressure increased, work hardening accumulated and Hastelloy, the stiffer component in the tape structure, became increasingly determinant to the stack modulus. For Sample 2, the stack modulus for both regimes 2 and 3 were smaller due to increased plating thickness. The stack modulus increased from 1.7 GPa to 4.6 GPa, from a value that was lower than the tangent modulus of copper (4GPa) to a value that was similar. According to Ref. [162], the tangent modulus of electroplated Ni at 2 % strain was ~2.3 GPa [162], which was comparable to our measurement, 1.7 GPa. The intercept of the fitting line on the y-axis (pressure level) of each regime could be considered as the onset of a deformation regime given that the deformation regime was purely elastic. The fitting lines for the second regime of Samples 1 and 2 had intercepts (16.1 MPa and 16.7 MPa) that were fairly close to 20 MPa, but the third regime for both samples had intercepts (46.2 MPa and 41.4 MPa) different than the onset value, 60 MPa, for

the third regime. Hence, that indicated there was more plastic deformation in the third regime than in the second regime. In both tape stack samples, the second regime was characterized by the tangent modulus of the softest material (copper in Sample 1, and nickel in Sample 2) in the structure. As the pressure level increased to the third regime, work hardening kept accumulating and the modulus of the harder materials, Hastelloy and copper, became representative of the samples. Because the moduli concluded from our measurement were controlled by the materials, the results should be applicable to tape stacks of different layers.

The results from our measurements follow the rule-of-mixture. However, the values of the modulus of nickel, copper, and Hastelloy need to be carefully considered. The as-received tape has a copper layer of 20 µm on each side, and the thickness of the Hastelloy is 50 µm. The Ni-plated tape has a nickel layer of 15 µm on each side. To apply the rule-of-mixture, we assume that the Hastelloy does not experience any plastic deformation, but the nickel and copper layer experience both elastic and plastic deformation. Therefore, we use tangent modulus for nickel and copper, 2.3 GPa [162] and 4 GPa [159] respectively, and use elastic modulus for Hastelloy, 190 GPa [159]. Given those, the calculated modulus is 8.8 GPa for Sample 1 and 5.2 GPa for Sample 2. Both calculated values are comparable to the measured moduli of the samples in their third regime.

6.3 Compression test of Roebel cable

Fig. 82 shows the stress-strain curve of the segment of Roebel cable. The first regime contained nearly 0.25 strain. Because the Roebel cable was fabricated with SuperPower tapes, the second regime and the third regime of the Roebel cable exhibited similar results as Sample 1,

the 10-layer tape stack. The second regime of Roebel cable showed a modulus of 3.1 $\pm$ 5% GPa, and the third regime showed a modulus of 9.1 $\pm$ 11% GPa. However, one should be aware that unlike tapes or tape stacks which are resistant to pressure up to 550 MPa [152], the critical current of Roebel cable is very sensitive to compression, and even a compression of 30-40 MPa can lead to at least 20% of critical current reduction of the cable [150] [152] [156]. The reason for the high sensitivity of critical current to pressure was because of the low contact surface area between tapes in the Roebel cable [163]. One possible method to mitigate the critical current sensitivity to pressure is to apply epoxy impregnation.

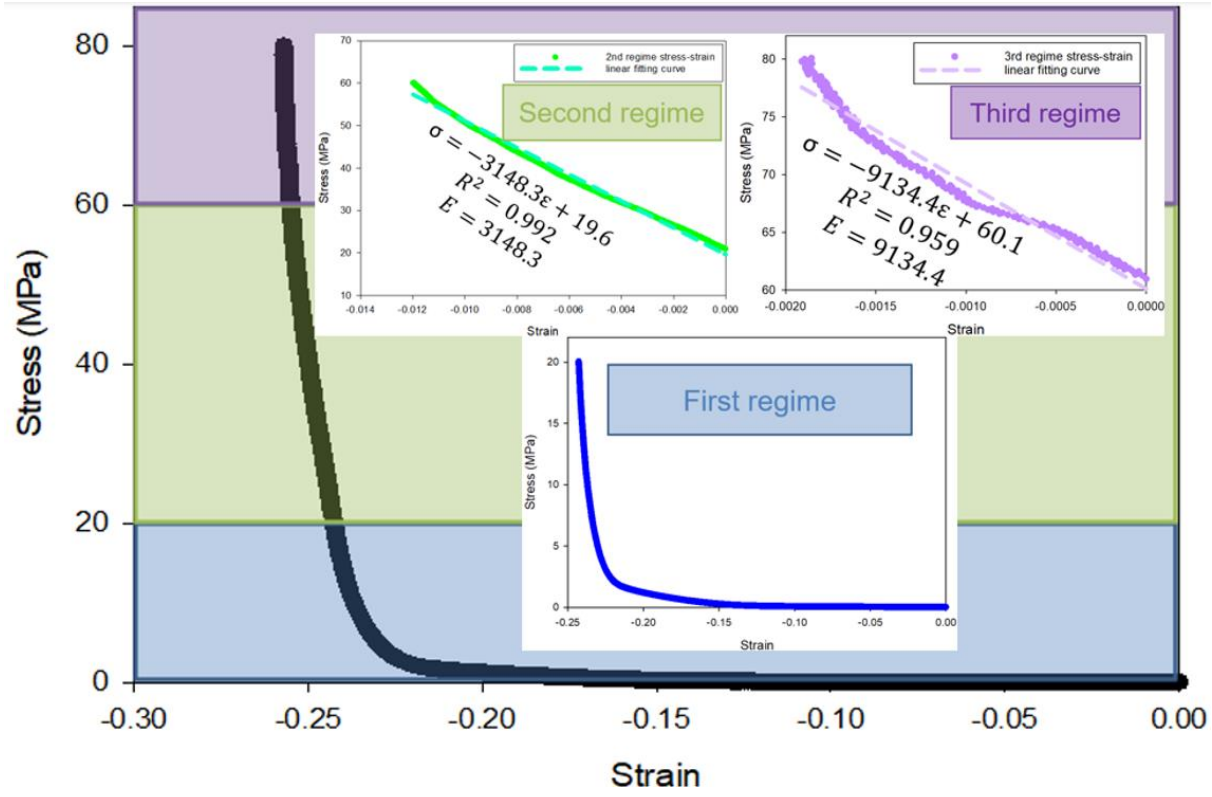

Figure 82: Stress-Strain curve of Sample 3. (Strain is determined as ΔL/L.)

Surface roughness measurement on the Roebel cable is presented in Fig. 83. The roughness measurements were performed on randomly selected areas on 8 of the 9 tapes in the cable. The

average surface roughness of Sample 3 decreased from 666 nm to 522 nm (24% reduction), which is also comparable with Sample 1.

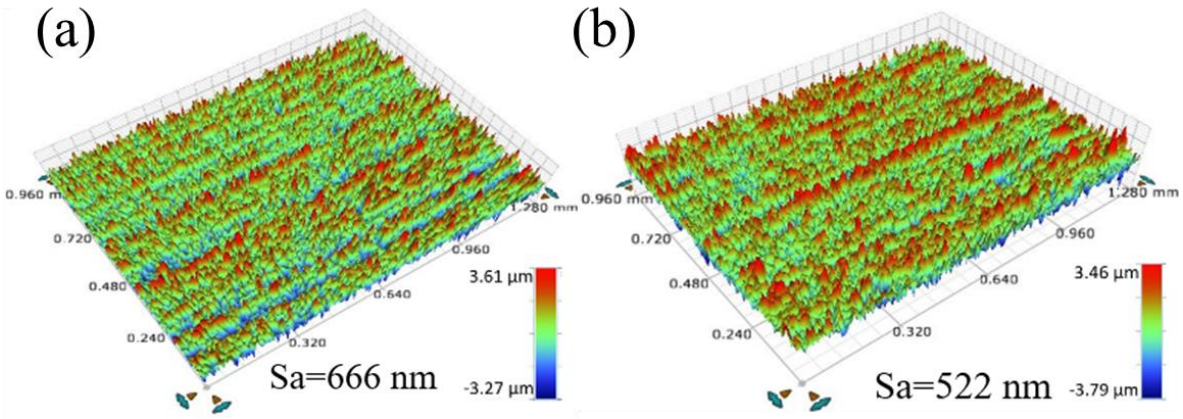

Figure 83: Surface roughness of (a) Sample 3 before pressing, (b) Sample 3 after pressing.

6.3 Compression test of Roebel cable

The three compression tests on CORC cables showed consistent results, Fig 84. The cables cracked at the pressure level of about 27 MPa. We calculated the transverse pressure applied on the CORC cables by normalizing the applied force to the product of sample length and cable diameter. If the same stress calculation is applied, based on other studies, the critical current of a CORC cable with a solid cylindrical copper former will start to decrease at stress as low as 1.2 MPa which is close to the cleavage stress limit of REBCO tape, and suffers at least 80 % reduction when the transverse pressure reached 4.7 MPa [157] [158]. From the inset of Fig. 84, the damaged cable showed cleavage fracture surface. Hence if CORC cables are to be used for high field applications, external reinforcements, such as epoxy impregnation [150] [157] and stainless steel overbending covers, are necessary [74] [164].

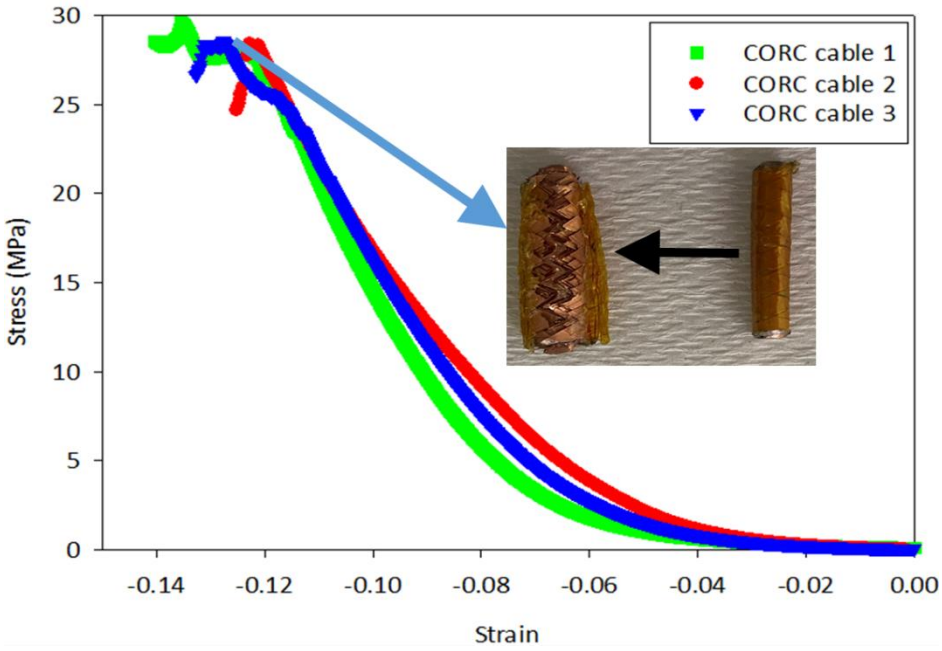

Figure 84: Stress-Strain curve of CORC cable

Chapter 7- Discussion

Major challenges to the application of REBCO CC tapes and cables to actual devices include quench protection, flux creep, and high AC loss. Controlling the inter-strand contact properties of a REBCO CC tape stack or a cable can affect quench by modifying current sharing. However, there is always a tradeoff between current sharing and AC loss, since improved current sharing will lead to an increase in the coupling loss. Therefore, the interstrand contact surface properties need to be determined on the basis of the needs of a specific application.

One very important conclusion we can draw from our study is that when considering current sharing in HTS, not only the inter-strand electrical contact property, but also the inter-strand thermal contact property and boundary cooling condition are critical factors. This is different from the case for LTS where current sharing is only controlled by the inter-strand electrical contact resistance. The reason for this is the relative speed of the events in the case of LTSC and HTSC, in the former, the event is quick (can in some cases be considered adiabatic), while for HTSC, the quench event is much slower, and heat is both shared to neighboring regions and to the bath. Indeed, while for LTSC, quench energy is most important, often for HTSC, quench power is critical. Basically, the key question to ask is how much current can flow through a cable before thermal runaway sets in, and the answer to this question is found by a power balance between the heat generation and the heat removal locally in the cable. For example, according to the simulation results from Chapter 3, given a certain inter-strand electrical contact resistance, the current limit that the central defective tape in a three-tape cable can carry is much higher when the inter-strand thermal contact property is not insulating. A variety of results for different sets of electrical and thermal contact resistances and thermal boundary conditions (BCs) are given in Chapter 3.

Another important factor to be considered is that the steady-state current sharing limit will be higher than the transient state. This is explored in Chapter 3 by changing the electrical boundary conditions (BCs) on the tapes. In the case of a pre-existing defect, current and voltage will have had time to equilibrate and the proper boundary conditions to consider are equipotentials at the ends of the conductors at each end of the cable (one for current injection, and the other for current extraction). In the case of a fault that happens in operation, the currents do not have time to equilibrate at the ends, and the proper electrical BCs are equal current injection/extraction into each strand at the ends of the cable.

This work focused more on the steady-state current sharing behavior. In this case, the defects are “pe-existing”, i.e., occurred during cabling or as part of wire manufacture. By using the three-tape cable model introduced in Chapter 3 the current sharing operation frontier for the pre-existent defect scenario can be determined as presented in Fig 85. We concluded that the maximum current this defective three-tape cable can carry is linearly proportional to the natural log of the product of the inter-strand electrical contact efficiency and the inter-strand thermal insulance, following $\frac{I_{c_{cable}}}{I_{c_{tape}}} = -0.0349 * \ln(\eta * \omega) + 3.0718$, A fit of our data leads to $y = -0.0349x + 3.0718$.

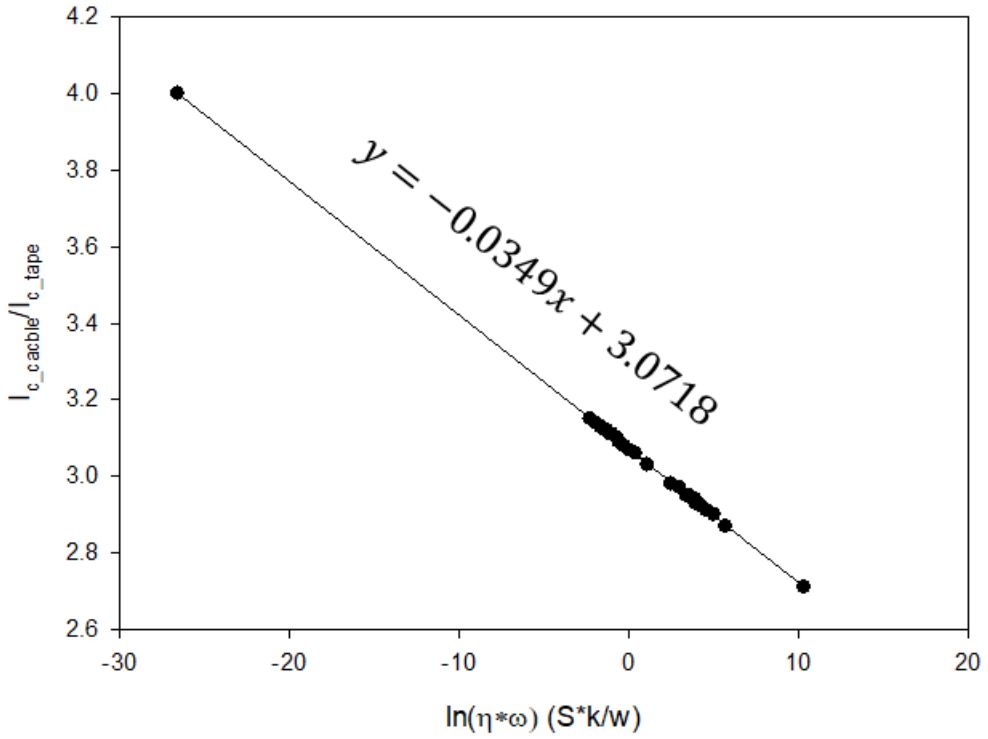

Figure 85: Current sharing operation frontier of steady state tree-tape cable model.

This compact expression gives an explicit formula for the ratio of $I_{c_{cable}}$ to $I_{c_{tape}}$ for a three strand cable (ideally in the absence of current sharing and no defects, the value would be 3), and shows it depending on the natural log of the electrical contact efficiency and the inter-strand thermal insulance. This is a very useful and predictive result, and one of the major takeaways of this work.

On a practical level, the easiest way to improve current sharing in multi-strand tape stacks and cables is to reduce the contact resistance by applying mechanical pressure. This is a practical method that can be used in no-insulation pancake coils where REBCO CCs are in a well-aligned tape-to-tape structure that enables the applied force to be uniformly distributed on the entire tape surface, leading to a maximum stress limit to be 500 MPa. However, for cables with twist

pitches and transposing structures, such as Roebel cable, CORC cable, and STAR cable, the stress limits are very low. Enhancing current sharing in those cables by simply applying pressure will not be applicable. For these cables, performing surface modification can be a better solution. In my study, I provide two surface treatment techniques, Ni-plating and PANI coating. Ni-plating reduces the inter-strand electrical contact resistance by replacing the thick native oxide layer on the Cu surface with a thinner native oxide layer on the Ni surface.

Although reducing the inter-strand electrical contact resistance can enhance the current sharing ability in the multi-strand REBCO cable, the coupling loss in the cable will also increase. To reduce the overall AC loss which consists of hysteresis loss, coupling loss, and eddy current loss, we propose to use Ni to replace the Cu stabilizer, so that the cable can have low inter-strand contact resistance to facilitate better current sharing and reduced eddy current loss. The PANI coating technique can be seen as a versatile approach to achieve a wide range of inter-strand contact properties by controlling the coating thickness, doping level, and concentration of conductive particle inclusion. Therefore, the end user of the PANI coating will have more options to make the tradeoff between current sharing and AC loss based on different applications. Moreover, PANI-coated REBCO cables or multi-strand tape stacks can be consolidated into one piece via a low-temperature heat treatment at around 50 ℃, and therefore will have better mechanical stability than cables with direct tape-to-tape contact.

Modifying inter-strand contact properties will change the AC loss in a multi-strand REBCO cable. Hence, we developed a 2D model that can simulate AC loss in a Roebel cable with given inter-strand contact properties. Compared to direct measurement, our simulation result has an error of less than 20 %. Moreover, both the simulation and experiment results show that the

hysteresis loss component in a multi-strand REBCO cable is suppressed due to the screening effect from the outer layers to the inner layers.

Finally, we studied the magnetization and flux creep in a STAR wire. We found that compared to LTSs, the maximum magnetization of the STAR wire is much higher (it is similar to CORC values). In addition, because it is wound with REBCO conductors, the cable/wire will suffer from high flux creep. One possible method to alleviate this problem is to apply pre-injection field cycles, so the initial magnetization can be reduced, leading to a reduced flux creep. In future work, it will be very useful to develop simulation models for different cables to better assist the implementation of REBCO in large-scale applications.

Chapter 8- Conclusions

As the needs for high field applications is increasingly imminent, Rare-Earth Barium Copper Oxide Coated Conductors (REBCO CCs) draws a lot of attention and becomes a hot topic of study because REBCO conductors have exceptional current carrying ability especially at high field, for example field > 22.5 T. However, quench protection and field quality are the two major challenges for the application of REBCO CCs. Because the normal zone propagation rate in the REBCO CCs is slow, 3-5 cm/s, and the ΔT between the operating temperature and the conductors' critical temperature is high, it is difficult to effectively perform quench detection in a timely manner. Considering another fact of the REBCO CCs that it is very common to introduce defects during the tape manufacturing process, cabling process, and coil winding process, localized hot spots may occur and lead to a catastrophic burn out of the coil.

Utilizing the self-protecting mechanism of current sharing in REBCO conductors can be a promising solution to the quench protection. In this case, when the supercurrent in one tape of a cable reaches a defective spot, it will bypass the defect via the neighboring tapes to avoid the generation of a non-healable localized hot spot. The no-insulation design of REBCO coils is based on this concept.

Whether effective current sharing will happen depends on the inter-strand contact properties. More specifically, because the thermal margin of REBCO conductors is high, the current sharing behavior will be dependent on the inter-strand electrical contact resistance, inter-strand thermal contact resistance, and boundary cooling conditions.

We have investigated various techniques to control the inter-strand contact properties, including cold pressing, hot pressing, Ni-plating, Ni-replacement, and PANI-coating. Through these processes, we achieved a various inter-strand electrical contact efficiency, ranging from 5400 $\mu\Omega * \mathrm{cm}^2$ to 2.7 $\mu\Omega * \mathrm{cm}^2$. Ni surface, based on our study, can provide the lowest contact resistance. In addition, Ni-plating/replacement laid a foundation for later PANI-coating treatment, which can be a promising upgraded replacement of the current epoxy-impregnation technique.

From our simulation results, we can conclude that different inter-strand contact properties can lead to different current sharing limits. Given a good inter-strand contact and liquid helium cooling condition, it is even possible for a defective cable to achieve a current sharing limit that is greater than 1. Moreover, the transient current sharing limit and the steady state current sharing limit are different from each other. In general, provided the same inter-strand contact properties and cooling conditions, the transient state current sharing limit in a REBCO cable will be smaller than that of the steady state. Hence, the lower limit should be carefully considered during magnet design.

Simply generating a high magnetic field is not sufficient for certain applications, such as particle accelerators and fusion magnets. Field quality is another important feature. Because the dimensions of a single REBCO CC tape, ranging from 2 mm to 6 mm, is much larger than that of LTS, hundreds of microns, and the J_c is high, REBCO usually exhibits strong magnetization. The magnetization from the conductor itself will generate an error field. In addition, because the individual pinning strength in REBCO is weak, flux creep is expected, which makes the error field to an even more complex time-varying state. Hence, quantification and minimization of the flux

creep in a REBCO conductor becomes an indispensable prerequisite for putting the conductor into real applications.

We measured the magnetization of a STAR cable. At fully flux penetrated state, the cable volume normalized magnetization of the cable is around 1140 kA/m, and the flux creep component is 140 kA/m (13%) for 1800 s. By applying pre-injection field cycles, the initial magnetization can be reduced and therefore the flux creep is reduced to 5.8 kA/m.

AC loss is of the major concern for the machinery applications of a superconductor. Without transport current, there will be three components of AC loss: hysteresis loss, Eddy current loss, and coupling current loss. Because coupling current loss is dependent on the current transferring from one strand to it neighbors, if we want to utilize the self-protecting mechanism of current sharing in the REBCO CCs to improve quench protection, we must live with the increased coupling loss. However, we can try to reduce the total AC loss by reducing the rest two parts. For example, for the same superconductor, hysteresis loss can be reduced by reducing the filament size. Eddy current loss can be reduced by replacing the high electrical conductivity matrix, such as Cu, of a superconductor composite with a low conductivity matrix material, for example Ni, so Ni-plating/replacement can be a desirable solution to provide better quench protection and lower eddy current loss.

As I will keep on working in this area, future work will involve applying different surface treatments to different REBCO cables, such as Roebel cable, CORC cable, and STAR cable, to improve their quench protection abilities. With these advanced cables and knowledge I acquired

through my study, I will be able to take part in projects of design and fabricating high field superconductor magnets.

References

[1] A. C. Wulff, A. B. Abrahmsen, and A. R. Insinga, "Multifilamentary coated conductors for ultra-high magnetic field applications," *Supercond. Sci. Technol.,* vol. 34, no. 5, 2021.

[2] J. A. Parrell, M. B. Field, Y. Zhang, and S. Hong, "Nb3Sn Conductor Development for Fusion and Particle Accelerator Applications," *Conf. Proc.,* vol. 711, no. 1, 2004.

[3] M. W. Rupich, S. Sathyamurthy, S. Fleshler et al, "Engineered Pinning Landscapes for Enhanced 2G Coil Wire," *IEEE Trans. Appl. Supercond.,* vol. 26, no. 3, 2016.

[4] T. Boutboul, S. Le Naour, D. Leroy, L. Oberli, and V. Previtali, "Critical Current Density in Superconducting Nb−Ti Strands in the 100 mT to 11 T Applied Field Range," *IEEE Trans. Appl. Supercond.,* vol. 16, no. 2, 2006.

[5] T. Nakashima, K. Yamazaki, S. Kobayashi et al, "Drastic Improvement in Mechanical Properties of DI-BSCCO Wire With Novel Lamination Material," *IEEE Trans. Appl. Supercond.,* vol. 25, no. 3, 2015.

[6] X. Xu, P. Xuan, J. Rochester, J. Y. Lee, and M. D. Sumption, "High critical current density in internally-oxidized Nb3Sn superconductors and its origin," *Scr. Mater.,* vol. 186, 2020.

[7] W. D. Markiewicz, D. C. Larbalestier, H. W. Weijers et al, "Design of a Superconducting 32 T Magnet With REBCO High Field Coils," *IEEE Trans. Appl.,* vol. 22, no. 3, 2012.

[8] J. Xia, H. Bai, H. Yong et al, "Stress and strain analysis of a REBCO high field coil based on the distribution of shielding current," *Supercond. Sci. Technol.,* vol. 32, no. 9, 2019.

[9] D. C. Larbalestier, J. Jiang, U. P. Trociewitz et al, "Isotropic round-wire multifilament cuprate superconductor for generation of magnetic fields above 30 T," *Nat. Mater.,* vol. 13, 2014.

[10] D. Uglietti, "A review of commercial high temperature superconducting materials for large magnets: from wires and tapes to cables and conductors," *Supercond. Sci. Technol.,* vol. 32, no. 5, 2019.

[11] Y. Li, D. Park, Y. Yan et al, "Magnetization and screening current in an 800 MHz (18.8 T) REBCO nuclear magnetic resonance insert magnet: experimental results and numerical analysis," *Supercond. Sci. Technol.,* vol. 32, no. 10, 2019.

[12] D. Park, J. Lee, Z. Li, and Y. Iwasa, "Prototype REBCO Z1 and Z2 shim coils for ultra high-field high-temperature superconducting NMR magnets," *Sci. Rep.,* vol. 10, 2020.

[13] W. Lee, D. Park, J. Bascuñán, and Y. Iwasa, "Construction and test result of an all-REBCO conduction-cooled 23.5 T magnet prototype towards a benchtop 1 GHz NMR spectroscopy," *Supercond. Sci. Technol.,* vol. 35, no. 10, 2022.

[14] D. Li, H. Wang, Y. Ren, and D. Wang, "Electromagnetic Design and Mechanical Behavior Analysis of an 850 MHz All REBCO Nuclear Magnetic Resonance Magnet," *IEEE Trans. Appl. Supercond.,* vol. 31, no. 3, 2021.

[15] K. L. Kim, S. Yoon, K. Cheon et al, "400-MHz/60-mm All-REBCO Nuclear Magnetic Resonance Magnet: Magnet Design," *IEEE Trans. Appl. Supercond.,* vol. 26, no. 4, 2015.

[16] L. Rossi, A. Badel, H. Bajas et al , "The EuCARD2 Future Magnets Program for Particle Accelerator High-Field Dipoles: Review of Results and Next Steps," *IEEE Trans. Appl. Supercond.,,* vol. 28, no. 3, 2018.

[17] G. Kirby, L. Rossi, A. Badel et al, "Status of the Demonstrator Magnets for the EuCARD-2 Future Magnets Project," *IEEE Trans. Appl. Supercond.,* vol. 26, no. 3, 2016.

[18] A. Badel, A. Ballarino, C. Barth et al, "Advances in the development of a 10-kA Class REBCO cable for the EuCARD2 demonstrator magnet," *IEEE Trans. Appl. Supercond.,* vol. 26, no. 3, 2016.

[19] J. V. Nugteren, G. Kirby, J. Murtomäki et al, "Toward REBCO 20 T+ Dipoles for Accelerators," *IEEE Trans. Appl. Supercond. ,* vol. 28, no. 4, 2018.

[20] M. Paidpilli and V. Selvamanickam, "Development of RE-Ba-Cu-O superconductors in the U.S. for ultra-high field magnets," *Supercond. Sci. Technol.,* vol. 35, no. 4, 2022.

[21] A. Sykes, A. E. Costley, C. G. Windsor et al, "Compact fusion energy based on the spherical tokamak," *Nucl. Fusion,* vol. 58, no. 1, 2018.

[22] B. N. Sorbom, J. Ball, T. R. Palmer et al, "ARC: A compact, high-field, fusion nuclear science facility and demonstration power plant with demountable magnets," *Fusion Eng. Des.,* vol. 100, 2015.

[23] P. M. McIntyre, J. Rogers, and A. Sattarov, "Blocks-in-Conduit: REBCO Cable for a 20T@20K Toroid for Compact Fusion Tokamaks," *IEEE Trans. Appl. Supercond.,* vol. 31, no. 5, 2021.

[24] M. Cyrot, "Ginzburg-Landau theory for superconductors," *Rep. Prog. Phys.,* vol. 36, no. 2, 1973.

[25] F. London and H. London, "The electromagnetic equations of the supraconductor," *Proc. R. Soc. A: Math. Phys. Eng. Sci.,* vol. 149, no. 886, 1935.

[26] M. D. Sumption, "MSE 6295 class slide," *Ohio State University,* 2021.

[27] G. Shams and M. Ranjbar, "Phase diagram of high temperature Y1Ba2Cu3O7−δ superconductor by Bean's model and experimental techniques," *Bull. Mater. Sci,* vol. 45, no. 206, 2022.

[28] Y. Yeshurun, A. Malozemoff, and A. Shaulov, "Magnetic relaxation in high-temperature superconductors," *Rev. Mod. Phys.,* vol. 68, no. 3, 1996.

[29] A. A. Abrikosov, "On the magnetic properties of superconductors of the second group," *Sov. Phys. JETP.,* vol. 5, 1957.

[30] K. Matsumoto and P. Mele, "Artificial pinning center technology to enhance vortex pinning in YBCO coated conductors," *Supercond. Sci. Technol.,* vol. 23, no. 1, 2010.

[31] M. Daeumling, J. M. Seuntjens, and D. C. Larbalestier , "Oxygen-defect flux pinning, anomalous magnetization and intra-grain granularity in YBa2Cu3O7–δ," *Nature,* vol. 346, 1990.

[32] V. A. Maroni, Y. Li, D. M. Feldmann, and Q. X. Jia, "Correlation between cation disorder and flux pinning in the YBa2Cu3O7 coated conductor," *J. Appl. Phys.,* vol. 102, no. 11, 2007.

[33] T. J. Haugan, T. A. Campbell, N. A. Pierce et al, "Microstructural and superconducting properties of (Y1−xEux)Ba2Cu3O7−δ thin films: x = 0–1," *Supercond. Sci. Technol.,* vol. 21, no. 2, 2008.

[34] L. Civale, "Vortex pinning and creep in high-temperature superconductors with columnar defects," *Supercond. Sci. Technol.,* vol. 10, no. A11, 1997.

[35] V. Pan, Y. Cherpak, V. Komashko et al, "Supercurrent transport in YBa2Cu3O7−δ epitaxial thin films in a dc magnetic field," *Phys. Rev. B,* vol. 73, 2006.

[36] D. Agassi, D. K. Christen, and S. J. Pennycook, "Flux pinning and critical currents at low-angle grain boundaries in high-temperature superconductors," *Appl. Phys. Lett.,* vol. 81, no. 15, 2002.

[37] Ch. Jooss, R. Warthmann, and H. Kronmüller, "Pinning mechanism of vortices at antiphase boundaries in YBa2Cu3O7-δ," *Phys. Rev. B,* vol. 61, no. 18, 2000.

[38] M. Murakami, M. Morita, K. Doi, and K. Miyamoto, "A New Process with the Promise of High Jc in Oxide Superconductors," *Jpn. J. Appl. Phys.,* vol. 28, 1989.

[39] X. Obradors, T. Puig, Z Li et al, "Epitaxial YBa2Cu3O7−x nanocomposite films and coated conductors from BaMO3 (M = Zr, Hf) colloidal solutions," *Supercond. Sci. Technol.,* vol. 31, no. 4, 2018.

[40] M. Sparing, E. Reich, J. Hänisch et al, "Controlling particle properties in YBa2Cu3O7−x nanocomposites by combining PLD with an inert gas condensation system," *Supercond. Sci. Technol.,* vol. 30, no. 10, 2017.

[41] T. Haugan, P. N. Barnes, R. Wheeler, F. Meisenkothen, and M. Sumption, "Addition of nanoparticle dispersions to enhance flux pinning of the YBa2Cu3O7-x superconductor," *Nature,* vol. 430, 2004.

[42] M. Malmivirta, H Rijckaert, V Paasonen et al, "Enhanced flux pinning in YBCO multilayer films with BCO nanodots and segmented BZO nanorods," *Sci. Rep.,* vol. 7, 2017.

[43] L. Pust, "Comparison between conventional flux creep in constant magnetic field and the effect of creep on the shape of magnetic hysteresis loops in high-Tc superconductors," *Supercond. Sci. Technol.,* vol. 3, no. 12, 1990.

[44] R. Puzniak, A. Szewczyk, and A. Wisniewski, "Magnetization Measurements on LHC Superconducting Strands," *IEEE Trans. Appl. Supercond.,* vol. 9, no. 2, 1999.

[45] R. Gupta, "Superconductivity," *US Particle Accelerator School on Superconducting Accelerator Magnets,* 2003.

[46] X. Xu, M.D. Sumption and X. Peng, "Internally Oxidized Nb3Sn Strands with Fine Grain Size and High Critical Current Density," *Adv. Mater.,* vol. 27, no. 8, 2015.

[47] A. Godeke, D. Turrioni, T. Boutboul et al., "Interlaboratory Comparisons of NbTi Critical Current Measurements," *IEEE Trans. Appl. Supercond.,* vol. 19, no. 3, 2009.

[48] J.L. MacManus-Driscoll and S.C. Wimbush, "Processing and application of high-temperature superconducting coated conductors," *Nat. Rev. Mater.,* vol. 6, 2021.

[49] J. Jiang, G. Bradford, S. I. Hossain et al, "High-Performance Bi-2212 Round Wires Made With Recent Powders," *IEEE Trans. Appl. Supercond. ,* vol. 29, no. 5, 2019.

[50] S. Barua, D. S. Davis, Y. Oz et al, "Critical Current Distributions of Recent Bi-2212 Round Wires," *IEEE Trans. Appl. Supercond.,* vol. 31, no. 5, 2021.

[51] J. Rochester, C. Myers , M. Sumption , T. Shen , M. Majoros, and E. W. Collings, "The Magnetization of Bi:2212 Rutherford Cables for," *IEEE Trans. Appl. Supercond.,* vol. 31, no. 5, 2021.

[52] C. Kovacs, M. Majoros, M. D. Sumption, E. W. Collings, "Magnetization Measurements of CORCTM and Roebel Type YBCO Cables for Accelerators Using a ±3-T Dipole Magnetometer," *IEEE Trans. Appl. Supercond.,* vol. 29, no. 5, 2019.

[53] C. S. Myers, M. D. Sumption and E. W. Collings, "Magnetization and Flux Penetration of YBCO CORC Cable Segments at the Injection Fields of Accelerator Magnets," *IEEE Trans. Appl. Supercond.,* vol. 29, no. 5, 2019.

[54] R. Gupta, M. Anereila, J. Cozzolino et al, "Common coil magnet program at BNL," *IEEE Trans. Appl. Supercond.,* vol. 11, no. 1, 2001.

[55] C. V¨ollinger, "Superconductor Magnetization Modeling for the Numerical Calculation of Field Errors in Accelerator Magnets," *Ph.D dissertation,* 2003.

[56] V.V. Kashikhin and A.V. Zlobin, "Correction of the persistent current effect in Nb/sub 3/Sn dipole magnets," *IEEE Trans. Appl. Supercond.,* vol. 11, no. 1, 2001.

[57] X. Wang, G. Ambrosio, G. Chlachidze et al, "Validation of Finite-Element Models of Persistent-Current Effects in Nb3Sn Accelerator Magnets," *IEEE Trans. Appl. Supercond.,* vol. 25, no. 3, 2015.

[58] T. Mulder, A. Dudarev, M. Mentink et al, "Performance Test of an 8 kA @ 10-T 4.2-K ReBCO-CORC Cable," *IEEE Trans. Appl. Supercond.,* vol. 26, no. 4, 2016.

[59] Q. Wu, Y. Wang, Z. Huang et al, "Electromagnetic and mechanical properties of CORC cable due to screening current," *Supercond. Sci. Technol.,* vol. 35, no. 7, 2022.

[60] M. D. Sumption, M. Majoros, E. W. Collings, M. A. Rindfleisch, and M. J. Tomsic, "AC Loss of Superconducting Materials- loss estimates for motors and generators for hybrid-electric aircraft: MgB2 wires, coated conductors," *CEC/ICMC 2019,* 2019.

[61] M. D. Sumption, M. Majoros, E. W. Collings, and T. Haugan, "AC Loss in Superconductor wires and tapes in a range of frequencies," *ASC 2022,* 2022.

[62] C. W. Chu, L. Z. Deng, and B. Lv, "Hole-doped cuprate high temperature superconductors," *Phys. C Supercond. Its Appl.,* vol. 514, 2015.

[63] N. H. Andersen, M. V. Zimmermann, T. Frello et al, "Superstructure formation and the structural phase diagram of YBa2Cu3O6+x," *Phys. C Supercond.,* Vols. 317-318, 1999.

[64] R. Liang, D. A. Bonn, and W. N. Hardy, "Evaluation of CuO2 plane hole doping in YBa2Cu3O6+x single crystals," *Phys. Rev. B,* vol. 73, no. 18, 2006.

[65] A. K. Saxena, "High-Temperature Superconductors," *SSMATERIALS.,* vol. 125, 2012.

[66] Y. Ando and K. Segawa, "Magnetoresistance of Untwinned YBa2Cu3Oy Single Crystals in a Wide Range of Doping: Anomalous Hole-Doping Dependence of the Coherence Length," *Phys. Rev. Lett.,* vol. 88, no. 16, 2002.

[67] K. Tomimoto, I. Terasaki, A. I. Rykov, T. Mimura, and S. Tajima, "Impurity effects on the superconducting coherence length in Zn- or Ni-doped," *Phys. Rev. B,* vol. 60, no. 1, 1999.

[68] https://www.superpower-inc.com/specification.aspx.

[69] X. Xiong, K. P. Lenseth, J. L. Reeves et al, "High Throughput Processing of Long-Length IBAD MgO and Epi-Buffer Templates at SuperPower," *IEEE Trans. Appl. Supercond.,* vol. 17, no. 2, 2007.

[70] S, Hahn, K. Kim, K. Kim et al, "45.5-tesla direct-current magnetic field generated with a high-temperature superconducting magnet," *Nature,* vol. 570, 2019.

[71] J. Fleiter, C. Lorin, and A. Ballarino, "On Roebel Cable Geometry for Accelerator Magnet," *IEEE Trans. Appl. Supercond.,* vol. 26, no. 3, 2016.

[72] G. A. Kirby, J. V. Nugteren, H. Bajas et al, "First Cold Powering Test of REBCO Roebel Wound Coil for the EuCARD2 Future Magnet Development Project," *IEEE Trans. Appl. Supercond.,* vol. 27, no. 4, 2017.

[73] D. C. van der Laan, J. D. Weiss, and D. M. McRae, "Status of CORC cables and wires for use in high-field magnets and power systems a decade after their introduction," *Supercond. Sci. Technol.,* vol. 32, 2019.

[74] D. C. van der Laan, J. D. Weiss, U. P. Trociewitz et al, "A CORC® cable insert solenoid: the first high-temerature superconducting insert magnet tested at currents exceeding 4 kA in 14 T background magnet field," *Supercond. Sci. Technol.,* vol. 33, no. 5, 2020.

[75] X. Wang, D. Abraimov, D. Arbelaez et al, "Development and performance of a 2.9 Tela dipole magnet using high temperature superconductor CORC® wires," *Supercond. Sci. Technol.,* vol. 34, no. 1, 2020.

[76] S. Kar, W. Luo, A. B. Yahia et al, "Symmetric tape round REBCO wire with Je (4.2 K, 15 T) beyond 450 A mm− 2 at 15 mm bend radius: A viable candidate for future compact accelerator magnet applications," *Supercond. Sci. Technol.,* vol. 31, no. 4, 2018.

[77] S. Kar, J. S. Sandra, W. Luo et al, "Next generation highly flexible round REBCO STAR wires with over 580 A mm-2 at 4.2 K, 20 T for future compact magnets," *Supercond. Sci. Technol.,* vol. 32, no. 10, 2019.

[78] M. Takayasu, L. Chiesa, L. Bromberg, and J. V. Minervini, "HTS twisted stacked-tape cable conductor," *Supercond. Sci. Technol.,* vol. 25, no. 1, 2011.

[79] S. Murase, T. Murakami, T. Seto et al, "Normal Zone and Quench Characteristics of Nb3Sn Wires with Jelly-Roll and In-Situ Processed CuNb Reinforcements," *IEEE Trans. Appl. Supercond.,* vol. 11, no. 1, 2001.

[80] A. D. Ouden, H. V. Weeren, W. A. J. Wessel et al, "Normal zone propagation in High-Current Density Nb3Sn Conductors for Accelerator Magnets," *IEEE Trans. Appl. Supercond.,* vol. 14, no. 2, 2004.

[81] S. Liu, L. Ren, J. Li et al, "Analysis of quench propagation characteristics of the YBCO coated conductor," *Phys. C: Supercond. Appl.,* vol. 471, no. 21-22, 2011.

[82] H. Chen, H. Liu, F. Liu, and Y. Shi, "Development of a Normal Zone Propagation Insert Set-up for YBCO Superconducting Tape," *IEEE Trans. Appl. Supercond.,* vol. 31, no. 8, 2021.

[83] A. Molodyk, S. Samoilenkov, A. Markelov et al, "Development and large volume production of extremely high current density YBa2Cu3O7 superconducting wires for fusion," *Sci. Rep.,* vol. 11, 2021.

[84] M. Polak, P. N. Barnes, P. Mozola et al, "Critical Current in YBCO Coated Conductors in the Presence of a Macroscopic Defect," *IEEE Trans. Appl. Spercond.,* vol. 19, no. 3, 2009.

[85] S. Furtner, R. Nemetschek, R. Semerad et al, "Reel-to-reel critical current measurement of coated conductors," *Supercond. Sci. Technol.,* vol. 17, 2004.

[86] G. P. Willering, "STABILITY OF SUPERCONDUCTING RUTHERFORD CABLES FOR ACCELERATOR MAGNETS," *Ph.D. thesis, University of Twente,,* 2009.

[87] C. J. Kovacs, M. D. Sumption, M. Majoros, E. W. Collings, "Modified Interconductor Contact Resistivity in Coated Conductor Stacks and Roebel Cables," *IEEE Trans. Appl. Supercond.,* vol. 30, no. 4, 2020.

[88] S. Xue, M. D. Sumption, E. W. Collings, "YBCO Coated Conductor Interlayer Electrical Contact Resistance Measured From 77 K to 4 K Under Applied Pressures up to 9.4 MPa," *IEEE Trans. Appl. Supercond.,* vol. 31, no. 5, 2021.

[89] M. Majoros, M. D. Sumption, E. W. Collings and N. J. Long, "Stability, inter-strand contact resistance, and AC Losses in YBCO Roebel cables," *IEEE Trans. Appl. Supercon.,* vol. 24, no. 3, 2014.

[90] M. Bonura, C. Barth, A. Joudrier, J. F. Troitino, A. Fête and C. Senatore,, "Systematic study of the contact resistance between REBCO tapes: pressure dependence in the case of No-Insulation, metal co-winding and metal-insulation," *IEEE Trans. Appl. Supercon.,* vol. 29, no. 5, 2019.

[91] M. D. Sumption, E.W. Collings, R.M. Scanlan, A. Nijhuis, H.H.J. ten Kate, S.W. Kim, M. Wake, and T. Shintomi, "Influence of strand surface condition on interstrand contact resistance and coupling loss in NbTi-wound Rutherford cables," *Cryogenics,* vol. 39, no. 3, 1999.

[92] K. L. Kim, Y. H. Choi, D. G. Yang, J. B. Song, and H. G. Lee, "Transient characteristics of a GdBCO racetrack pancake coil without turn-to-turn insulation," *Supercond. Sci. Technol.,* vol. 27, no. 1, 2014.

[93] J. Lu, R. Goddard, K. Han, and S. Hahn, "Contact resistance between two REBCO tapes under load and load cycles," *Supercond. Sci. Technol.,* vol. 30, no. 4, 2017.

[94] J. Lu, J. Levitan, D. McRae, and R. Walsh, "Contact resistance between two REBCO tapes: the effects of cyclic loading and surface coating," *Supercond. Sci. Technol.,* vol. 31, no. 8, 2018.

[95] Y. Wang, W. K. Chan, and J. Schwartz, "Self-protection mechanisms in no-insulation (RE)Ba2Cu3Ox high temperature superconductor pancake coils," *Supercond. Sci. Technol.,* vol. 29, no. 4, 2016.

[96] M. D. Sumption and M. Majoros, "Influence of electrical Turn-to-Turn sharing on quench protection in superconducting coils for very high power density motors for hybrid-electric aircraft," *AAIA Propulsion Energy 2019 Forum,* 2019.

[97] S. Xue, M. D. Sumption, D. Panik et al., "Electrical Contact Resistance in REBCO Stacks and Cables With Modified Surfaces," *IEEE Trans. Appl. Supercond.,* vol. 32, no. 6, 2022.

[98] M. Majoros, M. D. Sumption, S. Xue, "Current sharing in double-sided REBCO tape stacks – FEM Analysis," *LTWS 2023,* 2023.

[99] M. Guan et al., "Aparametric study on overband radial build for a REBCO 800-MHz insert of a 1.3-GHz LTS/THENMRmagnet," *IEEE Trans. Appl. Supercond.,* vol. 26, no. 4, 2016.

[100] J. Xia et al., "Stress and strain analysis of a REBCO high field coil based on the distribution of shielding current," *Supercond. Sci. Technol.,* vol. 32, no. 9, 2019.

[101] M. O. Eatough, D. S. Ginley, B. Morosin, and E. L. Venturini, "Orthorhombic-tetragonal phase transition in high-temperature superconductor YBa2Cu3O7," *Appl. Phys. Lett.,* vol. 51, 1987.

[102] J. Lu, Y. Xin, B. Jarvis, and H. Bai, "Oxygen out-diffusion in REBCO coated conductor due to heating," *Supercond. Sci. Technol.,* vol. 34, no. 7, 2021.

[103] A. Mogro-Campero, K. W. Paik, and L. G. Turner, "Degradation of thin films of YBa2Cu3O7 by annealing in air and in vacuum," *J. Supercond.,* vol. 8, 1995.

[104] S. Y. Lee, N. Mettlach, N. Nguyen, Y. M. Sun, and J. M. White, "Copper oxide reduction through vacuum annealing," *Appl. Surf. Sci.,* vol. 206, 2002.

[105] E. S. Lamber, C. N. Dykstal, J. M. Seo, J. E. Rowe, and P. H. Holloway, "Room -temperature oxidation ofNi(110) at lowand atomospherix oxygen," *Oxid Met.,* vol. 45, 1996.

[106] X. Liu, Z. Zhu, F. Ning et al., "The Research on No-Insulation ReBCO Racetrack Coil," *IEEE Trans. Appl. Supercond.,* vol. 29, no. 5, 2019.

[107] S. Hahn, D. K. Park, J. Voccio, J. Bascunan, and Y. Iwasa, "No-insulation (NI) HTS inserts for >1 GHz LTS/HTS NMR magnets," *IEEE Trans. Appl. Supercond.,* vol. 22, no. 3, 2012.

[108] W. Li, S. Peng, J. Zheng et al., "Preparation and Testing of Large Scale Epoxy Impregnated REBCO Coil for SMES," *IEEE Trans. Appl. Supercond.,* vol. 31, no. 8, 2021.

[109] I. Kesgin, Q. Hassee, Y. Ivanyushenkov, and U. Welp, "Performance of 2G-HTS REBCO Undulator Coils Impregnated Epoxies Mixed With Different Fillers," *IEEE Trans. Appl. Supercond.,* vol. 27, no. 4, 2017.

[110] H. Park, A. Kim, S. Kim et al, "Mechanical and electric characteristics of vacuum impregnated no-insulation HTS coil," *Physica C,* vol. 504, 2014.

[111] K. M. Molapo, P. M. Ndangili, R. F. Ajayi et al., "Electronics of Conjugated Polymers (I): Polyaniline," *Int. J. Electrochem. Sci.,* vol. 7, no. 12, 2012.

[112] Y. Mohd, R. Ibrahim, and M. F. Zainal, "Electrodeposition and characterization of Polyaniline films," *2012 IEEE Symposium on Humanities, Science and Engineering Research,* 2012.

[113] R. M. G. Rajapakse, A. D. L. Chandani Perera, and H. D. S. Premasiri, "Polyaniline retained glass templates as sensors for acidic/basic and/or redox gases," *J. Natn. Sci. Foundation Sri Lanka,* vol. 28, no. 4, 2000.

[114] M. Beygisangchin, S. A. Rashid, S. Shafie et al., "Preparations, Properties, and Applications of Polyaniline and Polyaniline Thin Films—A Review," *Polymer,* vol. 13, no. 12, 2021.

[115] M. Khalid, A. M. B. Honorato and H. Varela, "Polyaniline: Synthesis Methods, Doping and Conduction Mechanism," *IntechOpen,* 2018.

[116] H. Xu, J. Zhang, Y. Chen et al., "Electrochemical polymerization of polyaniline doped with Cu2+ as the electrode material for electrochemical supercapacitors," *RSC Adv.,* vol. 4, 2014.

[117] S. Xue, M. Majoros, M. D. Sumption, T. Garg, E. W. Collings, "FEM Analysis of Current Sharing in REBCO Coated Conductor Cables for Particle Accelerator Applications," *IEEE Trans. Appl. Spercond.,* vol. 33, no. 5, 2023.

[118] M. Majoros, M. D. Sumption, S. Xue, E. W. Collings, "Stability and Current haring in YBCO Cables-Impact of Broken Elements- FEM Modeling," *IEEE Trans. Appl. Spercond.,* vol. 32, no. 6, 2022.

[119] [Online]. Available: https://www.comsol.com.

[120] A. D. Berger, "Stability of Superconducting Cables with Twisted Stacked YBCO Coated Conductors," *MIT Plasma Science and Fusion Center,* 2012.

[121] E. G. Brentari, P. J. Giarratano, and R. V. Smith, "Boiling Heat Transfer for Oxygen, Nitrogen, hydrogen, and Helium," *National Bureau of Standards,* vol. 5, 1965.

[122] G. Grissonnanche, O. Cyr-Choinière, F. Laliberté et al., "Direct measurement of the upper critical field in cuprate superconductors," *Nat. Commun.,* vol. 5, 2014.

[123] J. W. Ekin, "Experimental Techniques for Low-Temperature Measurements," *Oxford University Press,* 2006.

[124] M. Takayasu, L. Chiesa, N. C. Allen, and J. V. Minervini, "Present status and recent developments of the twisted stacked-tape cable conductor," *IEEE Trans. Appl. Supercond.,* vol. 26, no. 2, 2016.

[125] G. P.Willering, D. C. van der Laan, H. W. Weijers et al., "Effect of variations in terminal contact resistances on the current distribution in high-temperature superconducting cables," *Supercond. Sci. Technol.,* vol. 28, 2015.

[126] L. Bromberg, M. Takayasu, P. Michael et al., "Current distribution and re-distribution in HTS cables made from 2nd generation tapes," *Proc. AIP Conf.,* 2012.

[127] S. Venuturumilli; F. Berg, Z. Zhang et al., "Forceful uniform current distribution among all the tapes of a coaxial cable to enhance the operational current," *IEEE Trans. Appl. Supercond.,* vol. 27, no. 4, 2017.

[128] S. Amet, L. Bottura, V. Granata et al., "Persistent and Coupling Current Effects in the LHC Superconducting Dipoles," *IEEE Trans. Applied Supercond.,* vol. 13, no. 2, 2003.

[129] A. Jain, "Dynamic effects in superconducting magnets," *US Particle Accelerator School on Superconducting Accelerator Magnets,* 2003.

[130] G. V. Velev, P. Bauer, J. DiMarco et al., "Measurements of the persistent current decay and snapback effect in tevatron dipole magnets," *IEEE Trans. Appl. Supercond.,* vol. 17, no. 2, 2007.

[131] S. Kar, J. S. Sandra, W. Luo et al., "Next-generation highly flexible round REBCO STAR wires with over 580 A mm−2 at 4.2 K, 20 T for future compact magnets," *Supercond. Sci. Technol.,* vol. 32, no. 10, 2019.

[132] E. Galstyan, J. Kadiyala, M. Paidpilli et al., "High critical current STAR® wires with REBCO tapes by advanced MOCVD," *Supercond. Sci. Technol.,* vol. 36, no. 5, 2023.

[133] W. Luo, S. Kar, X. Li et al., "Superior critical current of Symmetric Tape Round (STAR) REBCO wires in ultra-high background fields up to 31.2 T," *Supercond. Sci. Technol.,* vol. 31, no. 12, 2018.

[134] C. S. Myers , M. D. Sumption , and E. W. Collings, "Magnetization and Creep in YBCO Tape and CORC Cables for Particle Accelerators: Value and Modification Via Preinjection Cycle," *IEEE Trans. Appl. Supercond.,* vol. 29, no. 5, 2019.

[135] J. Rochester, C. Myers, T. Shen et al., "Flux Creep in a Bi-2212 Rutherford Cable for Particle Accelerator Applications," *IEEE Trans. Appl. Supercond.,* vol. 32, no. 4, 2022.

[136] X. Wang, S. Caspi, D. R. Dietderich et al., "A viable dipole magnet concept with REBCO CORC® wires and further development needs for high-field magnet applications," *Supercond. Sci. Technol.,* vol. 31, no. 4, 2018.

[137] J. P. Murphy, N. N. Gheorghiu, T. Bullard et al, "AC loss in YBCO coated conductors at high dB/dt measured using a spinning magnet calorimeter (stator testbed environment)," *Cryogenics,* vol. 86, 2017.

[138] M. D. Sumption, J. P. Murphy, T. Haugan et al., "AC losses of Roebel and CORC® cables at higher AC magnetic fields and ramp rates," *Supercond. Sci. Technol.,* vol. 35, no. 2, 2022.

[139] C. J. Kovacs, M. Majoros, M. D. Sumption, E. W. Collings, "Quench and stability of Roebel cables at 77 K and self-field: Minimum quench power, cold end cooling, and cable cooling efficiency," *Cryogenics,* vol. 95, 2018.

[140] M. Vojenčiak, F. Grilli, S. Terzieva et al , "Effect of self-field on the current distribution in Roebel-assembled coated conductor cables," *Supercond. Sci. Technol.,* vol. 24, no. 9, 2011.

[141] M. Majoros, M. D. Sumption, E. W. Collings and N. J. Long, "Inter-strand current sharing and ac loss measurements in superconducting YBCO Roebel cables," *Supercond. Sci. Technol.,* vol. 28, no. 5, 2015.

[142] M. D. Sumption, *ASC,* Vols. 3LOr2C-04 , 2022.

[143] V. B. Zenkevitch, A. S. Romanyuk, V. V. Zheltov, "Losses in composite superconductors at a high level of magnetic field excitation: Part 2," *Cryogenics,* vol. 21, no. 1, 1981.

[144] S. Xue, J. Kwon, Y. Guo et al., "Compressive Stress-Strain Behavior of REBCO Coated Conductors and Cables," *IEEE Trans. Appl. Supercond.,* vol. 33, no. 5, 2023.

[145] D. C. van der Laan, P. D. Noyes, G. E. Miller et al., "Characterization of a high-temperature superconducting conductor on round core cables in magnetic fields up to 20 T," *Supercond. Sci. Technol.,* vol. 26, no. 4, 2013.

[146] R. Gupta, M. Anerella, A. Ghosh et al., "Hybrid High-Field Cosine-Theta Accelerator Magnet R&D With Second-Generation HTS," *IEEE Trans. Appl. Supercond.,* vol. 25, no. 3, 2015.

[147] H. W. Weijers, W. D. Markiewicz, A. V. Gavrilin et al., "Progress in the Development and Construction of a 32-T Superconducting Magnet," *IEEE Trans. Appl. Supercond.,* vol. 26, no. 4, 2016.

[148] J. Ruuskanen, A. Stenvall, V. Lahtinen, and E. Pardo, "Electromagnetic nonlinearities in Roebel-cable-based accelerator magnet prototype: Variational approach," *Supercond. Sci. Technol.,* vol. 30, no. 2, 2020.

[149] X. Zhang, H. Liu, Y. Shi et al, "Development of a 5 T Class Insert Coil Using YBCO Coated Conductors," *IEEE Trans. Appl. Supercond.,* vol. 29, no. 5, 2019.

[150] P. Gao, W. A. J. Wessel, M. Dhallé et al., "Effect of resin impregnation on the transverse pressure dependence of the critical current in ReBCO Roebel cables," *Supercond. Sci. Technol.,* vol. 32, no. 5, 2019.

[151] K. L. Kim, S. Hahn, Y. Kim et al, "Effect of Winding Tension on Electrical Behaviors of a No-Insulation ReBCO Pancake Coil," *IEEE Trans. Appl. Supercond.,* vol. 24, no. 3, 2014.

[152] D. Uglietti, R. Wesche, and P. Bruzzone, "Effect of transverse load on the critical current of a coated conductor Roebel cable," *Supercond. Sci.Technol.,* vol. 26, no. 7, 2013.

[153] Y. Yanagisawa, H. Nakagome, T. Takematsu et al., "Remarkable weakness against cleavage stress for YBCO-coated conductors and its effect on the YBCO coil performance," *Physica C,* vol. 471, no. 15-16, 2011.

[154] H. Maeda and Y. Yanagisawa, "Recent developments in high-temperature superconducting magnet technology," *IEEE Trans. Appl. Supercond.,* vol. 24, no. 3, 2014.

[155] S. Yin, M. Duranti, C. A. Swenson et al., "Degradation of REBCO coated conductors due to a combination of epoxy impregnation, thermal cycles, and quench: Characteristics and a method of alleviation," *J. Appl. Phys.,* vol. 128, no. 17, 2020.

[156] S. Otten, M. Dhallé, P. Gao et al., "Enhancement of the transverse stress tolerance of REBCO Roebel cables by epoxy impregnation," *Supercond. Sci. Technol.,* vol. 28, no. 6, 2015.

[157] Y. Shi, S. Dai, T. Ma et al., "Analysis on the transverse compression performance of the CORC cable," *Supercond. Sci. Technol.,* vol. 35, no. 12, 2022.

[158] D. C. van der Laan, D. M. McRae, and J. D. Weiss, "Effect of the transverse compressive monotonic and cyclic loading on the performance of superconducting CORC cables and wires," *Supercond. Sci. Technol.,* vol. 32, no. 1, 2018.

[159] N. C. Allen, L. Chiesa, and M. Takayasu, "Structural modeling of HTS tapes and cables," *Cryogenics,* vol. 80, no. 3, 2016.

[160] F. Pierro, Z. Zhao, C. M. Owen, "Finite-Element Analysis of the Strain Distribution Due to Bending in a REBCO Coated Conductor for Canted Cosine Theta Dipole Magnet Applications," *IEEE Trans. Appl. Supercond.,* vol. 29, no. 5, 2019.

[161] Z. Zhao, P. Moore, and L. Chiesa, "Structural Finite Element Analysis of REBCO Tape Delamination with Solid-Shell Element under Various Loads," *IOP Conf. Ser.: Mater. Sci. Eng.,* vol. 1241, no. 1, 2022.

[162] T. Nagoshi, T. M. Chang, S. Tatsuo, and M. Sone, "Mechanical properties of nickel fabricated by electroplating with supercritical CO2 emulsion evaluated by micro-compression test using non-tapered micro-sized pillar," *Microelectron. Eng.,* vol. 110, 2013.

[163] J. Fleiter, A. Ballarino, L. Bottura et al., "Characterization of Roebel cables for potential use in high-field magnets," *IEEE Trans. Appl. Supercond.,* vol. 25, no. 3, 2015.

[164] J. Stern, J. Swanson, T. Bogdanof et al., "Developing a Vacuum Pressure Impregnation Procedure for CORC Wires," *IEEE Trans. Appl. Supercond.,* vol. 323, no. 6, 2022.

[165] R. Gupta, "Superconductivity," *US Particle Accelerator School on Superconducting Accelerator Magnets,* 2003.